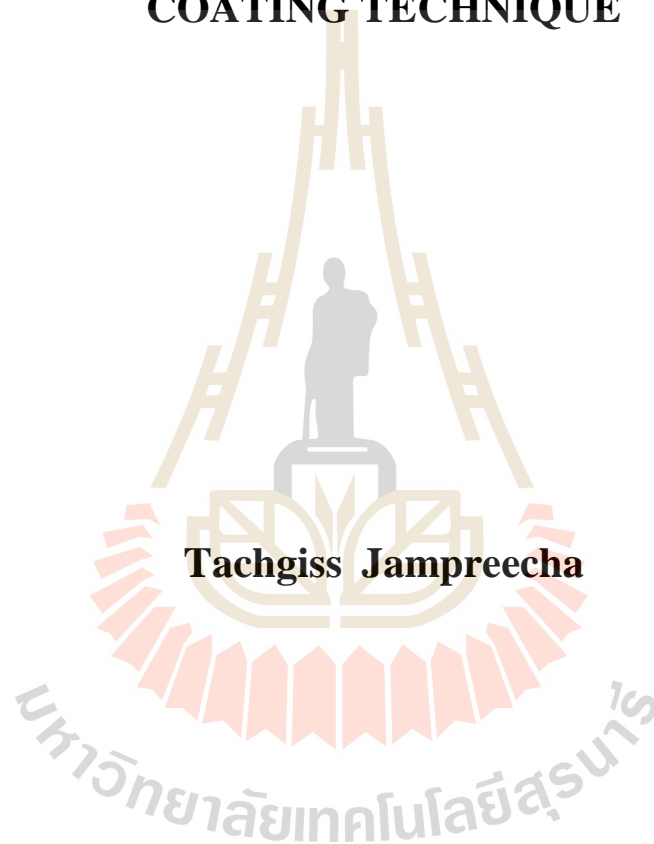


**STRUCTURAL, ELECTRICAL AND MAGNETIC
PROPERTIES OF Cu-DOPED BISMUTH FERRITE
THIN FILMS PREPARED BY SPIN
COATING TECHNIQUE**



**A Thesis Submitted in Partial Fulfillment of the Requirements for the
Degree of Master of Science in Applied Physics
Suranaree University of Technology
Academic Year 2018**

สมบัติเชิงโครงสร้าง ไฟฟ้าและแม่เหล็กของฟิล์มบางบิสแมทเฟอร์ไรท์
เจือด้วยทองแดงเตรียมด้วยเทคนิคการสปิ้นโคตติง

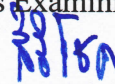


วิทยานิพนธ์นี้เป็นส่วนหนึ่งของการศึกษาตามหลักสูตรปริญญาวิทยาศาสตรมหาบัณฑิต
สาขาวิชาฟิสิกส์ประยุกต์
มหาวิทยาลัยเทคโนโลยีสุรนารี
ปีการศึกษา 2561

**STRUCTURAL, ELECTRICAL AND MAGNETIC
PROPERTIES OF Cu-DOPED BISMUTH FERRITE
THIN FILMS PREPARED BY SPIN COATING TECHNIQUE**

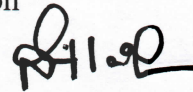
Suranaree University of Technology has approved this thesis submitted in partial fulfillment of the requirements for a Master's Degree.

Thesis Examining Committee



(Assoc. Prof. Dr. Sirichok Jungthawan)

Chairperson



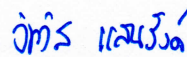
(Prof. Dr. Santi Maensiri)

Member (Thesis Advisor)



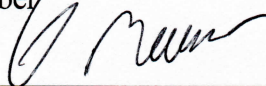
(Assoc. Prof. Dr. Worawat Meevasana)

Member



(Dr. Wittawat Saenrang)

Member



(Assoc. Prof. Dr. Worawat Meevasana)



(Prof. Dr. Santi Maensiri)

Vice Rector for Academic Affairs
and Internationalization

Dean of Institute of Science

ทักษกฤษ แจ่มปรีชา : สมบัติเชิงโครงสร้าง ไฟฟ้าและแม่เหล็กของฟิล์มบางบิสมัทเฟอร์ไรท์
เจือด้วยทองแดงเตรียมด้วยเทคนิคการสปินโคตติง (STRUCTURAL, ELECTRICAL AND
MAGNETIC PROPERTIES OF Cu-DOPED BISMUTH FERRITE THIN FILMS
PREPARED BY SPIN COATING TECHNIQUE). อาจารย์ที่ปรึกษา :
ศาสตราจารย์ ดร.สันติ แม้นศิริ, 126 หน้า.

ฟิล์มบาง/วัสดุเฟอร์ไรท์อ็อกไซด์/แม่เหล็กแอนติเฟอร์โร

ในงานวิจัยเล่มนี้ได้ทำการประดิษฐ์และศึกษาคุณสมบัติเชิงโครงสร้าง ไฟฟ้าและแม่เหล็ก
ของฟิล์มบางบิสมัทเฟอร์ไรท์ (BiFeO_3) ซึ่งถูกเจือด้วยธาตุทองแดง (Cu) เพื่อแทนที่ธาตุเหล็ก
(Fe) โดยโครงสร้างฟิล์มบางบิสมัทเฟอร์ไรท์ที่ถูกเจือด้วยธาตุทองแดงนั้นจะอยู่ในรูปสารประกอบ
 $\text{BiFe}_{1-x}\text{Cu}_x\text{O}_3$ ความเข้มข้นของการเจือที่ $x = 0.1, 0.2, 0.3, 0.5, 1.0, 2.0$ และ 3.0 (1% 2%
3% 5% 10% 20% และ 30% โมล) ของธาตุโลหะในโครงสร้างฟิล์มบาง ตัวอย่างฟิล์มที่ถูกเตรียม
ขึ้นได้ถูกนำไปตรวจสอบสมบัติเชิงโครงสร้างผลึก สัณฐานวิทยาของพื้นผิวฟิล์มและความหนา
สถานะทางเคมีและพันธะทางเคมี โดยเทคนิคการตรวจสอบการเลี้ยวเบนของรังสีเอ็กซ์ (XRD)
กล้องจุลทรรศน์แบบส่องกราด (SEM) การดูดกลืนรังสีเอ็กซ์ (XAS) และ การปลดปล่อย
อนุภาคโฟโตอิเล็กตรอนจากการฉายรังสีเอ็กซ์ (XPS) ส่วนสมบัติทางไฟฟ้าถูกศึกษาโดยเครื่อง
Agilent4294A โดยการนำค่าความจุไฟฟ้า (C_p) และค่าการสูญเสียทางไฟฟ้า ($\tan \delta$) ที่วัดได้มา
คำนวณและวิเคราะห์ค่าคงที่ไดอิเล็กตริกค่าความต้านเชิงซ้อน รวมทั้งผลของอุณหภูมิที่ส่งผลต่อ
คุณสมบัติทางไฟฟ้าของฟิล์มบาง สมบัติทางแม่เหล็กถูกศึกษาโดยเครื่องวัดโมเมนต์แม่เหล็กแบบ
สั้นตัวอย่างในสนามแม่เหล็ก (VSM)

ฟิล์มบางบิสมัทเฟอร์ไรท์ที่เจือด้วยทองแดง ($\text{BiFe}_{1-x}\text{Cu}_x\text{O}_3$) ที่ถูกเตรียมขึ้นมีพื้นผิวฟิล์ม
เป็นเนื้อเดียวกันและมีความหนาประมาณ 200-300 nm แต่มีบางส่วนของผิวฟิล์มที่เป็นก้อนฟิล์ม
ขนาดนาโนอยู่บนพื้นผิวฟิล์ม ความบริสุทธิ์เชิงโครงสร้างของฟิล์มมีความบริสุทธิ์ตามผลการแทรก
สอดรังสีเอ็กซ์ของบิสมัทเฟอร์ไรท์ (BiFeO_3) เฉพาะฟิล์มที่ยังไม่มีการเจือธาตุทองแดงเท่านั้น ส่วน
ฟิล์มที่มีการเจือธาตุทองแดงจะมีความไม่บริสุทธิ์เชิงโครงสร้างของไบสมัทเตตระไฮดรอกไซด์
($\text{Bi}_2\text{Fe}_4\text{O}_9$) ปนอยู่ด้วย การดูดกลืนรังสีเอ็กซ์ของฟิล์มบางได้แสดงสถานะเลขออกซิเดชัน
พบว่าเลขออกซิเดชันของธาตุ Bi Fe และ Cu มีเลขออกซิเดชันเป็น Bi^{3+} Fe^{3+} และ $\text{Cu}^{2+,3+}$ การ
ปลดปล่อยอนุภาคโฟโตอิเล็กตรอนจากการฉายรังสีเอ็กซ์ของฟิล์มบางได้ยืนยันสถานะเลข
ออกซิเดชันของ Bi^{3+} และ Fe^{3+} และการมีอยู่ของช่องว่างออกซิเจน O_v ที่พลังงานยึดเหนี่ยว 531.5

eV การศึกษาคุณสมบัติทางไฟฟ้าของฟิล์มบางพบว่ามีความสมบัติการนำไฟฟ้าของฟิล์มบางมีค่าออกซิเดชันของ Bi^{3+} และ Fe^{3+} และการมีอยู่ของช่องว่างออกซิเจน O_v ที่พลังงานยึดเหนี่ยว 531.5 eV การศึกษาคุณสมบัติทางไฟฟ้าของฟิล์มบางพบว่ามีความสมบัติการนำไฟฟ้าของฟิล์มบางมีค่าลดลงเมื่อมีการเจือธาตุทองแดงมากขึ้น พิจารณาจากความนำไฟฟ้าที่มากขึ้นจากค่าความนำไฟฟ้าขอบเกรน (σ_{gb}) $1.9-0.13 \times 10^{-4} \text{ S.cm}$ แต่กระนั้นการนำไฟฟ้ากลับมากขึ้นเมื่อมีการเจือธาตุทองแดงที่สูงกว่า $x = 0.03$ อาจเป็นผลเนื่องจากการลดลงของผลึกคริสตอลไลน์และความไม่บริสุทธิ์ทางโครงสร้างผลึกของฟิล์มบางบิสมาทเฟอร์ไรต์ ส่วนคุณสมบัติทางแม่เหล็กของฟิล์มบางบิสมาทเฟอร์ไรต์เจือด้วยทองแดงนั้นพบว่ามีการเจือธาตุทองแดงนั้นมีผลต่อการเพิ่มขึ้นของโมเมนต์แม่เหล็กอันเนื่องมาจากขนาดของเกรนที่ลดลงและคุณสมบัติทางโดเมนแม่เหล็กคัมเบิลเอ็กซ์เซ่งที่มีการเจือปนของคอปเปอร์ออกไซด์ (CuO , Cu_2O) รวมไปถึงช่องว่างออกซิเจนของฟิล์มบางที่ซึ่งซึ่งทำให้เกิดชั้นเวเลนซ์อิเล็กตรอนอิสระ จากกราฟฮิสเทอรีซิสลูปพบว่า ค่าแมกนีไตเซชันอิ่มตัว (M_s) ค่าเรมานเนสซ์ (M_r) และ ค่า Coercivity (H_c) มีค่าเพิ่มขึ้นเมื่อมีการเจือธาตุทองแดงเพิ่มขึ้น นอกจากนี้เมื่อทำการพิจารณา ค่า Susceptibility (χ) ที่สนามแม่เหล็ก (H) 2 kOe โดยเปลี่ยนแปลงอุณหภูมิ 50-400 K พบว่า แนวโน้มของค่า Susceptibility (χ) บ่งบอกถึงคุณสมบัติแม่เหล็กแอนติเฟอร์โรของฟิล์มบาง ตามกฎของ คูรี-ไวร์ส ซึ่งมีอุณหภูมิเนล (T_N) อยู่ในช่วง 55-70 K ค่าอุณหภูมิเนล (T_N) เพิ่มขึ้นเมื่อมีการเจือธาตุทองแดงเพิ่มขึ้นซึ่ง อาจเป็นผลเนื่องมาจากสารแอนติเฟอร์โรผสมของไฮรอนออกไซด์ (F_2O_3) และคอปเปอร์ออกไซด์ (C_2O_3)

สาขาวิชาฟิสิกส์
ปีการศึกษา 2561

ลายมือชื่อนักศึกษา _____
ลายมือชื่ออาจารย์ที่ปรึกษา _____
ลายมือชื่ออาจารย์ที่ปรึกษาร่วม _____

TACHGISS JAMPREECHA : STRUCTURAL, ELECTRICAL AND
MAGNETIC PROPERTIES OF Cu-DOPED BISMUTH FERRITE
THIN FILMS PREPARED BY SPIN COATING TECHNIQUE.
THESIS ADVISOR : PROF. SANTI MAENSIRI, D.Phil. 126 PP.

THIN FILMS/FERROIC/ANTIFERROMAGNETISM

In this research, Cu-doped bismuth ferrite thin films were fabricated and studied structural, electrical, and magnetic properties. The Cu elements were doped to bismuth ferrite structure (BiFeO_3) for substitution Fe elements as concentration $x = 0.01, 0.02, 0.03, 0.05, 0.1, 0.2$ and 0.3 (1, 2, 3, 5, 10, 20 and 30 mol %). The $\text{BiFe}_{1-x}\text{Cu}_x\text{O}_3$ thin films samples were investigated crystallite phases structure and crystallite sizes by x-ray diffraction (XRD). Surface morphology and thickness were revealed by scanning electron microscope (SEM). Oxidation states of films elements (Bi, Fe and Cu) were investigated by x-ray absorption spectroscopy (XAS). The elements (Bi, Fe and Cu) oxidation states and existence of oxygen vacancy were confirmed by x-ray photoelectron spectroscopy (XPS). The electrical properties were investigated by Agilent4294A precision impedance analyzer by measurement capacitance (C_p) and loss tangent ($\tan \delta$). The magnetic properties were investigated by vibration sample magnetometer (VSM). The crystallite phase structure of the thin films was pure phase of bismuth ferrite (BiFeO_3) only on undoped bismuth ferrite thin films. For Cu-doped thin films samples were compounded with some impurity phase of dibismuth tetrairon oxide ($\text{Bi}_2\text{Fe}_4\text{O}_9$). The films surfaces morphology showed some inhomogeneous of mountain films. The films thicknesses which were measured by SEM cross section technique, are about 200-300 nm. The oxidation states

of Bi^{3+} , Fe^{3+} and Cu^{2+} , $^{3+}$ elements were investigated by x-ray absorption spectroscopy technique. The photoelectrons emission spectra which had been revealed valence electron binding energy of Bi and Fe elements, were confirmed oxidation states of Bi^{3+} , Fe^{3+} and existence of oxygen vacancy.

The electrical properties of the thin films were revealed by dielectric permittivity constant and complex impedance spectroscopy. The grain boundary conductance (σ_{gb}) decreased with increasing Cu content elements for $1.9-0.13 \times 10^{-4} \text{ S.cm}$ as $x = 0.01-0.3$. Increasing of grain boundary related to crystallite size effect. So, grain boundary resistance (R_{gb}) was increased trend when doped Cu elements as $x = 0.00-0.03$, according to decreasing of grain boundary conductance. The magnetic properties of the thin films were found that saturation magnetization (M_s), remanent magnetization (M_r) and coercive force (H_c) increased with increasing of Cu-doped concentration. Susceptibility (χ) versus variant temperature (50-400 K) graph of the thin films showed antiferromagnetic behavior, according to Curie- Weiss law. Néel temperature (T_N) of the $\text{BiFe}_{1-x}\text{Cu}_x\text{O}_3$ thin films were about 55 and 70 K, as Cu-doped $x = 0.05$ and 0.2. The Néel temperature forward shifted with increasing Cu doping concentration may be because increasing weak ferromagnetic magnetic of copper oxide's electrons orbitals interaction (CuO , Cu_2O_3).

School of Physics

Academic Year 2018

Student's Signature

Advisor's Signature

Co-advisor's Signature

ACKNOWLEDGEMENTS

I would like to thank everyone who supported, advised and involved with my research thesis, through gave me a chance and an experience of studying and researching about materials science research field. I would like to thank my both thesis adviser Prof. Dr. Santi Maensiri and Assoc. Prof. Dr. Worawat Meevasana who taught and trained my materials researching skills, and gave many chance to polish my presentation skills in national conferences and international conferences. I would like to thank my brother and sister in Advanced Materials Physics laboratory research group who helped every methods and every suggestion about my research, through proofreading and submission of my research. I would like to thank my friends both of SUT and KCU graduate students who gave conveniences about equipment services, and any suggestions about my research. Finally, I would like to thank my parents and my brother who have always supported everything, and have been giving encouragement to me every day.

Tachgiss Jampreecha

CONTENTS

	Page
ABSTRACT IN THAI.....	I
ABSTRACT IN ENGLISH	III
ACKNOWLEDGEMENTS.....	V
CONTENTS.....	VI
LIST OF FIGURES	X
LIST OF TABLES.....	XVI
CHAPTER	
I INTRODUCTION.....	1
1.1 Background and Motivation.....	1
1.2 Objectives of the research	3
1.3 Scope and limitation.....	3
1.4 Location of the research	4
1.5 Anticipated outcome	4
1.6 Outline of thesis	5
II LITERATURE REVIEW	6
2.1 Bismuth ferrite.....	6
2.1.1 Bismuth ferrite nanoparticles.....	7
2.1.2 Bismuth ferrite thin films.....	14
2.1.3 Experimental results overview of BiFeO ₃	17

CONTENTS (Continued)

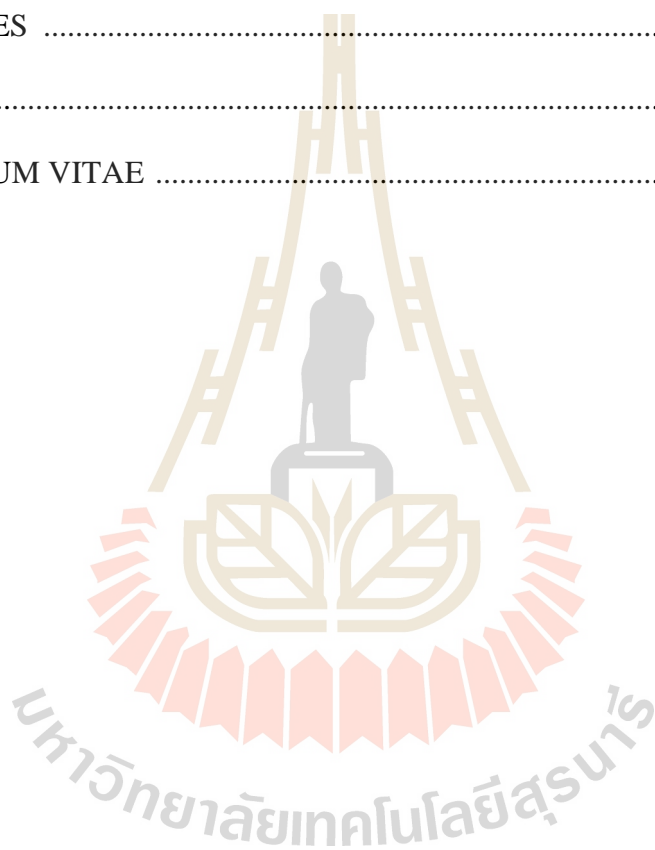
	Page
2.2 Polarization and electrical properties of materials.....	21
2.2.1 Dielectric polarization	21
2.2.2 Interaction of dielectric and polarization among electric field.....	24
2.2.3 Dielectric permittivity constant and alternating electric fields.....	25
2.2.4 Dielectric permittivity constant and complex impedance spectroscopy	27
2.3 Magnetism and magnetic properties of materials	29
2.3.1 Magnetism materials.....	29
2.3.2 Magnetic field.....	29
2.3.3 Magnetic inductor	33
2.3.4 Magnetic moment	33
2.3.5 Magnetic parameters and hysteresis loop	36
2.3.6 Classes of magnetism materials and theory of magnetic materials	39
2.3.7 Magnetism of 3d transition metal oxide	50
2.3.8 Units for magnetic properties	52
III EXPERIMENTAL PROCEDURE.....	54
3.1 Fabrication of Cu doped BiFeO ₃ thin films.....	54

CONTENTS (Continued)

	Page
3.1.1 Precursor preparation	54
3.1.2 Substrate preparation	56
3.1.3 Spin coating and annealing of Cu doped BiFeO ₃ thin films	58
3.2 Materials characterization	59
3.2.1 X-ray diffraction	59
3.2.2 Scanning electron microscopy	61
3.2.3 X-ray absorption spectroscopy	62
3.2.4 X-ray photoelectron spectroscopy.....	63
3.3 Electric and magnetic properties	64
3.3.1 Electric properties	64
3.3.2 Magnetic properties.....	65
IV RESULTS AND DISCUSSION.....	67
4.1 X-ray diffraction.....	67
4.2 Scanning electron microscopy	81
4.3 X-ray adsorption spectroscopy.....	85
4.4 X-ray photoelectron spectroscopy.....	88
4.5 Magnetic properties.....	97
4.6 Electrical properties.....	104
V CONCLUSIONS AND SUGGESTIONS.....	110
5.1 Structure and characterization.....	110

CONTENTS (Continued)

	Page
5.2 Magnetic properties.....	111
5.3 Electrical properties.....	112
5.4 Suggestion.....	113
REFERENCES	115
APPENDIX	125
CURRICULUM VITAE	126



LIST OF FIGURES

Figure	Page
2.1	The bismuth ferrite space group (a) rhombohedral R3c, (b) cubic Pm-3m..... 7
2.2	The sol-gel method for preparation initial precursor 8
2.3	X-ray diffraction patterns of $\text{BiFe}_{1-x}\text{Cu}_x\text{O}_3$ nanoparticles 9
2.4	Sem images of $\text{BiFe}_{1-x}\text{Cu}_x\text{O}_3$ nanoparticles 10
2.5	Frequency dependence of dielectric constant ϵ at room temperature 11
2.6	Frequency dependence of loss tangent $\tan\delta$ at room temperature 11
2.7	Impedance spectra as a function of applied dc bias for $\text{Bi}_{1-x}\text{La}_x\text{FeO}_3$ 12
2.8	The ideal circuit of dielectric materials 13
2.9	Room temperature M-H curves for $\text{BiFe}_{1-x}\text{Cu}_x\text{O}_3$ nanoparticles 14
2.10	X-ray pattern of the pure BFO and BFMC_2O thin films deposited on FTO.... 15
2.11	FE-SEM images of the surface and the cross-section micrographs of BiFeO_3 (a and b) and BFMC_2O_3 (c and d) thin films. 16
2.12	Frequency dependence of polarization of dielectric materials 23
2.13	The polarization mechanism of each types polarization of dielectric materials 23
2.14	Shows ideal complex impedance spectroscopy which consist of grain part and grain boundary part..... 28
2.15	Magnetic field of permanence magnetism materials..... 30
2.16	Shows electromagnetic filed and Right Hand rule for indication direction 30
2.17	Shows orbital magnetic moment within single atom model..... 36

LIST OF FIGURES (Continued)

Figure	Page
2.18 Shows spin magnetic moment within of single electron.....	36
2.19 Shows normal magnetic hysteresis loop graph of $M-H$	39
2.20 Shows $2P^2$ electron orbital shell of a C^6 atom.....	43
2.21 Shows magnetic moment responding of diamagnetic and paramagnetic materials with external magnetic field	45
2.22 Shows magnetic moment responding of ferromagnetism and antiferromagnetism materials with external magnetic field	46
2.23 Shows effect of vertical external magnetic field to magnetization of antiferromagnetism at below neel temperature	48
2.24 Shows ideal temperature dependence of magnetic susceptibility of paramagnetic, ferromagnetic and antiferromagnetic	50
2.25 Shows super exchange interaction of $3d^5$ electron orbital of a pair transition metal oxide	51
2.26 Shows double exchange interaction of A $3d^3$ and A $3d^4$ electron orbital of a pair transition metal oxide.....	52
3.1 Shows illustration of precursor preparation of condensation solprocess.....	56
3.2 Shows illustration of substrates preparation of Pt/Si n type substrate.....	57
3.3 Shows DC plasma sputtering machine	57
3.4 Shows spin coating methods for fabricated pre-annealing samples	58
3.5 Shows spin coating machine	58
3.6 Shows time scheme of annealing Cu-doped $BiFeO_3$ thin films	59
3.7 Shows x-ray incident and reflected, according to Bragg's law.....	60

LIST OF FIGURES (Continued)

Figure	Page
3.8 Shows X-ray diffraction machine	61
3.9 Shows scanning electron microscopy	62
3.10 Shows measurement technique scheme of x-ray absorption reflection mode	63
3.11 Shows measurement technique scheme of x-ray photoelectron spectroscopy	64
3.12 Shows Agilent 4294A precision impedance analyser	65
3.13 Shows vibrating sample magnetometer.....	66
4.1 Shows grazing incident x-ray diffraction pattern BiFeO ₃ of nitrate route.....	68
4.2 Shows x-ray diffraction pattern of substrate, Si, Pt, PtO, PtO ₂ , Bi ₂ Fe ₄ O ₉	69
4.3 Shows grazing incident x-ray diffraction pattern of BiFeO ₃ dependence of acetone solvent quantity	70
4.4 Shows grazing incident x-ray diffraction pattern of BiFeO ₃ thin films which were prepared by acetic acid and citric acid.....	71
4.5 Shows grazing incident x-ray diffraction pattern BiFeO ₃ dependent on acetic acid quantity	72
4.6 Shows grazing incident x-ray diffraction pattern BiFeO ₃ thin films dependence of annealing temperature 600, 700 and 800 °C which annealed for 6 hours	73
4.7 Shows polyethylene terephthalate XRD holder from 3D printed holder.....	74
4.8 Shows grazing incident x-ray diffraction pattern background of 3D printed XRD holder.....	75

LIST OF FIGURES (Continued)

Figure	Page
4.9 Shows grazing incident x-ray diffraction pattern background of Glass slide XRD holder	75
4.10 Shows grazing incident x-ray diffraction pattern BiFeO ₃ on Glass slide XRD holder and 3D printed holder	76
4.11 Shows x-ray diffraction pattern BiFeO ₃ thin films by grazing incident beam and normal beam	77
4.12 Shows normal incident beam x-ray diffraction pattern of BiFe _{1-x} Cu _x O ₃ thin films	78
4.13 Shows peak shift of BiFe _{1-x} Cu _x O ₃ thin films at $2\theta \approx 56.505$	79
4.14 Shows crystallite sizes dependence of Cu content %.....	80
4.15 Shows SEM and SEM cross section images of BiFe _{1-x} Cu _x O ₃ thin films as x = 0.0.....	83
4.16 Shows SEM and SEM cross section images of BiFe _{1-x} Cu _x O ₃ thin films as x = 0.1.....	84
4.17 Shows x-ray absorption spectra of Fe K-edge of BiFe _{1-x} Cu _x O ₃ thin films	86
4.18 Shows x-ray absorption spectra of Cu K-edge of BiFe _{1-x} Cu _x O ₃ thin films	87
4.19 Shows x-ray absorption spectra of Bi M5-edge of BiFe _{1-x} Cu _x O ₃ thin films.....	88
4.20 Shows x-ray photoelectron spectra valence electron Bi 4f _{5/2} and Bi 4f _{7/2} of BiFe _{1-x} Cu _x O ₃ thin films as x = 0.0-0.03.....	89
4.21 Shows x-ray photoelectron spectra valence electron Bi 4f _{5/2} and Bi 4f _{7/2} of BiFe _{1-x} Cu _x O ₃ thin films as x = 0.05-0.3	90

LIST OF FIGURES (Continued)

Figure	Page
4.22 Shows x-ray photoelectron spectra valence electron $\text{Fe}^{3+} 2p_{3/2}$ and $\text{Fe}^{3+} 2p_{3/2}$ of $\text{BiFe}_{1-x}\text{Cu}_x\text{O}_3$ thin films as $x = 0.0-0.03$	91
4.23 Shows x-ray photoelectron spectra valence electron $\text{Fe}^{3+} 2p_{1/2}$ and $\text{Fe}^{3+} 2p_{3/2}$ of $\text{BiFe}_{1-x}\text{Cu}_x\text{O}_3$ thin films as $x = 0.05-0.3$	92
4.24 Shows x-ray photoelectron spectra valence electron $\text{Cu}^{3+} 2p_{1/2}$ and $\text{Cu}^{3+} 2p_{3/2}$ of $\text{BiFe}_{1-x}\text{Cu}_x\text{O}_3$ thin films as $x = 0.0-0.03$	92
4.25 Shows x-ray photoelectron spectra valence electron $\text{Cu}^{3+} 2p_{1/2}$ and $\text{Cu}^{3+} 2p_{3/2}$ of $\text{BiFe}_{1-x}\text{Cu}_x\text{O}_3$ thin films as $x = 0.05-0.3$	93
4.26 Shows x-ray photoelectron spectra valence electron O 1s and O_v of $\text{BiFe}_{1-x}\text{Cu}_x\text{O}_3$ thin films as $0.0-0.03$	94
4.27 Shows x-ray photoelectron spectra valence electron O 1s and O_v of $\text{BiFe}_{1-x}\text{Cu}_x\text{O}_3$ thin films as $0.05-0.3$	94
4.28 Shows hysteresis loop of $\text{BiFe}_{1-x}\text{Cu}_x\text{O}_3$ thin films as $x = 0.00-0.3$	98
4.29 Shows hysteresis loop grid scales of $\text{BiFe}_{1-x}\text{Cu}_x\text{O}_3$ thin films as $x = 0.00-0.03$	99
4.30 Shows hysteresis loop grid scales of $\text{BiFe}_{1-x}\text{Cu}_x\text{O}_3$ thin films as $x = 0.05-0.3$	100
4.31 Shows temperature dependence of susceptibility $\text{BiFe}_{1-x}\text{Cu}_x\text{O}_3$ thin films as $x = 0.0, 0.02, 0.05$ and 0.2 at 2.5 kOe	101
4.32 Shows temperature dependence of susceptibility of $\text{BiFe}_{1-x}\text{Cu}_x\text{O}_3$ thin films as $x = 0.02, 0.05$ and 0.2 at 2.5 kOe	102

LIST OF FIGURES (Continued)

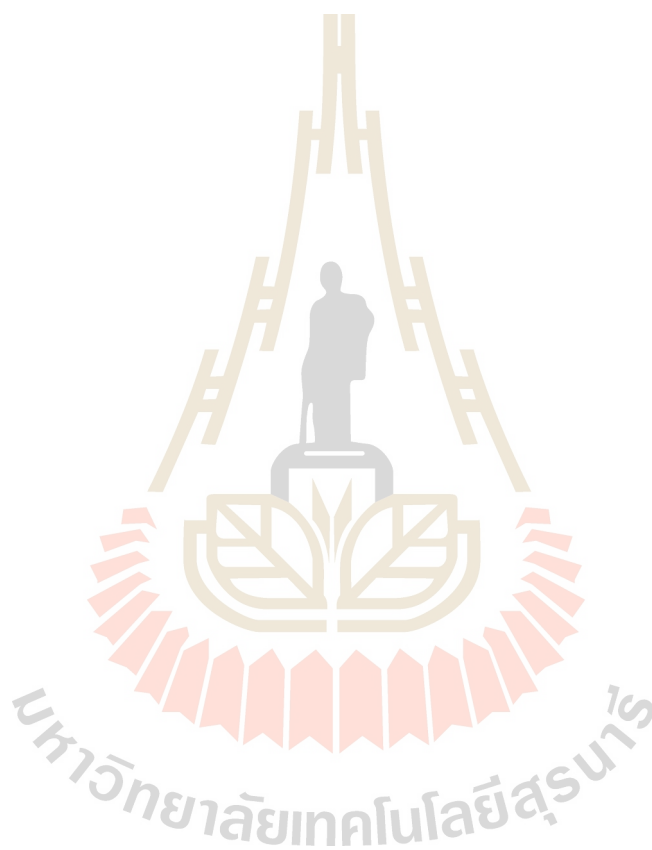
Figure		Page
4.33	Shows frequency dependence of real part dielectric permittivity of $\text{BiFe}_{1-x}\text{Cu}_x\text{O}_3$ thin films	104
4.34	Shows frequency dependence of imaginary part dielectric permittivity of $\text{BiFe}_{1-x}\text{Cu}_x\text{O}_3$ thin films	105
4.35	Shows frequency dependence of loss tangent of $\text{BiFe}_{1-x}\text{Cu}_x\text{O}_3$ thin films	105
4.36	Shows original complex impedance spectroscopy of $\text{BiFe}_{1-x}\text{Cu}_x\text{O}_3$ thin films	107
4.37	Shows fitted complex impedance spectroscopy of $\text{BiFe}_{1-x}\text{Cu}_x\text{O}_3$ thin films	108

LIST OF TABLES

Table		Page
2.1	Shows synthesis method, dielectric constant, loss tangent and magnetic parameters of rare earth doped BiFeO ₃ thin films.....	17
2.2	Shows saturation magnetization, remanent magnetization and coercive force of rare earth doped BiFeO ₃ thin films.	19
2.3	Classes of magnetism materials and indicator parameters	40
2.4	Magnetic parameters and units	52
3.1	List of materials and solvent which were used to fabricated Cu doped BiFeO ₃ thin films.....	55
4.1	Shows binding energy positions counts number, full width at half maximum and Gauss fixed quantity Bi ³⁺ 4f _{5/2} and Bi ³⁺ 4f _{7/2} of BiFe _{1-x} Cu _x O ₃ thin films as x = 0.0-0.3.....	95
4.2	Shows binding energy positions counts number, full width at half maximum and Gauss fixed quantity Fe ³⁺ 2p _{1/2} and Fe ³⁺ 2p _{3/2} of BiFe _{1-x} Cu _x O ₃ thin films as x = 0.0-0.3.....	96
4.3	Shows binding energy positions counts number, full width at half maximum and Gauss fixed quantity O s ₁ and O _v of BiFe _{1-x} Cu _x O ₃ thin films as x = 0.0-0.3.	97
4.4	Shows list of saturation magnetization, remanent magnetization and coercivity force of BiFe _{1-x} Cu _x O ₃ thin films.....	103

LIST OF TABLES (Continued)

Table		Page
4.5	Shows list of grain and grain boundary of resistance, capacitance and conductance of $\text{BiFe}_{1-x}\text{Cu}_x\text{O}_3$ thin films as $x = 0.0-0.3$	109



CHAPTER I

INTRODUCTION

1.1 Background and Motivation

Nowadays, transition metals oxide semiconductor (MOS) have been widely used for electronic devices such as gases sensor, solar catalyst, microelectronic devices because of its excellent properties (Khajonrit *et al.*, 2017). Some MOS materials have interesting properties as follows: ferromagnetic, ferroelectric and ferroelastics. The MOS materials which consisted of ferromagnetic, ferroelectric and ferroelastics properties (Qian *et al.*, 2017) are called multiferroic materials. Bismuth ferrite BiFeO_3 is one of multiferroic materials which have been interested by materials scientist association. Multiferroic materials BiFeO_3 is a perovskite structure (Xue *et al.*, 2004) which the structure of perovskite was formed as ABO_3 . This wonderful structure of BiFeO_3 have optical properties of blue range visible sun light (Zhai *et al.*, 2015), through magnetic and electrical properties. Normally, BiFeO_3 perovskite structure was found as rhombohedral distorted ($R3c$) structure which both Bi and Fe cation are center position of perovskite structure (Yotburut *et al.*, 2017). The BiFeO_3 materials were widely studied in forms of nanoparticle structure, micro-fiber structure, thin films, rare earth doping distorted structure (Sharif *et al.*, 2018). Those study were done to improve and enhance magnetic, optical, dielectric, electrical properties of BiFeO_3 because those properties are too weak at room temperature. So, natural BiFeO_3 did not sufficient adapt

to electronic and magnetic application devices. The curie temperature and Néel temperature of BiFeO₃ nanoparticles stayed at 1,103 K and 643 K, respectively (Dong *et al.*, 2014; Singh *et al.*, 2006; Wang, 2003). Improvement multiferroic properties of BiFeO₃ by using thin films form have been known well. This structure form can be prepared by variant methods such as high radio frequency RF sputtering deposition, pulse laser deposition, spin coating method, dip coating method. The difference preparation methods are conducive to differ quality, thickness and morphology yield of the films. The differences of those yield are conducive to differ magnetization and electrical polarization, light absorption (Kumar *et al.*, 2010). Thin films form is an optional way for saving materials precursor source because films preparation requested a little initial precursor. Magnetization and electrical polarization of thin films can be inducted with external magnetic field and applying electric current frequency. So, these inductions can be applied to magnetic and electrical controller devices. The magnetic and electrical properties of BiFeO₃ nanoparticles which were reported by literature reviews, had magnetization about $M_s \approx 0.07$ emu/g and remanent polarization about $P_r \approx 0.232$ $\mu\text{C}/\text{cm}^2$ at room temperature (Shah *et al.*, 2015).

In this research, Cu-doped bismuth ferrite thin films were fabricated for studying morphology structure, crystallite structure and magnetic/electrical properties. In the first, the BiFe_{1-x}Cu_xO₃ thin films were doped Cu elements to distort structure BiFe_{1-x}Cu_xO₃, at Cu-doped concentration $x = 0.0, 0.01, 0.02, 0.03, 0.05, 0.1, 0.2,$ and 0.3 . The variants concentration of Cu doping was done for studying optimal doping concentration versus each properties of BiFe_{1-x}Cu_xO₃ thin films. Initial precursors were prepared by using sol-gel method because it's a simple process and low cost. The thin films were characterized by x-ray diffraction (XRD) for indicating crystal pattern of

BiFeO₃ structure. X-ray absorption spectroscopy (XAS) was used to reveal oxidation state of Bi, Fe and Cu elements in the thin films structure. X-ray photoelectron spectroscopy (XPS) was used to confirm oxidation states of Bi, Fe elements and existence oxygen vacancy. Homogeneous of thin films surface and film thickness were revealed by scanning electron microscope (SEM). Vibrating sample magnetometer (VSM) was used to investigate magnetic properties of the thin films. Agilent4294 precision impedance analyzer was used to reveal complex impedance and conductivity of thin films.

1.2 Objectives of the research

1.2.1 To fabricate bismuth ferrite thin films by using sol-gel method and spin coating technique.

1.2.2 To characterize bismuth ferrite thin films by using advanced x-ray measurement techniques (XRD, XAS and XPS) and analysis techniques.

1.2.3 To study structure of bismuth ferrite thin films.

1.2.4 To study magnetic properties of bismuth ferrite thin films.

1.2.5 To study electrical properties of bismuth ferrite thin films

1.2.6 To study the effect of Cu-doped bismuth ferrite thin films on structure, magnetic and electrical properties.

1.3 Scope and limitation

1.3.1 The research is about fabrication BiFe_{1-x}Cu_xO₃ thin films, at Cu doping concentration $x = 0.0, 0.01, 0.02, 0.03, 0.05, 0.1, 0.2$ and 0.3 by using sol-gel method and spin coat technique.

1.3.2 The morphology, particles size effect of Cu-doped bismuth ferrite thin films was studied and compared with standard and literatures review.

1.3.3 The structural, magnetic and electrical properties of Cu-doped bismuth ferrite thin films were studied and compared.

1.4 Location of the research

1.4.1 Advanced Materials Physics Laboratory (AMP), School of Physics, Institute of Science, Suranaree University of Technology, Nakhon Ratchasima, Thailand.

1.4.2 Department of Physics, Faculty of Science, Khon Kaen University, Khon Kaen, Thailand.

1.5 Anticipated outcome

1.5.1 To achieve fabrication Cu-doped bismuth ferrite thin films prepared by spin coating technique.

1.5.2 To understand characterization Cu-doped bismuth ferrite thin films.

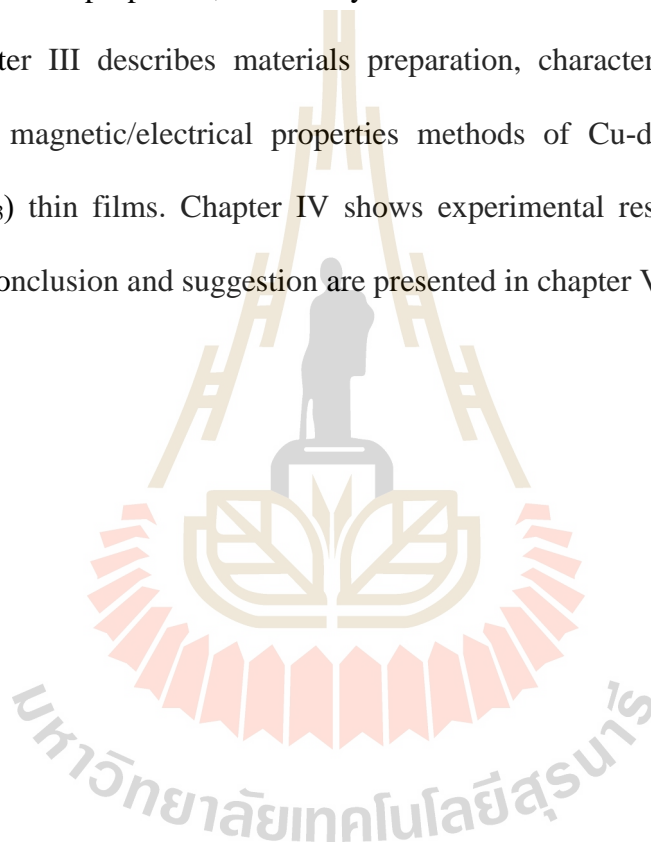
1.5.3 To comprehend magnetic and electrical properties of Cu-doped bismuth ferrite thin films.

1.5.4 Skillful of analysis magnetic/electrical properties of Cu-doped bismuth ferrite thin films.

1.5.5 Publishing this thesis research.

1.6 Outline of thesis

This research consists of five chapters. The initial chapter has introduced about motivation and reasons for concerning in this topic research. Chapter II consists of literature review reports of the materials information, synthesis method, characterization method, investigation of magnetic/electrical properties, theory of magnetic/electrical properties, and analysis methods which involved with bismuth ferrite. Chapter III describes materials preparation, characterization methods and investigation magnetic/electrical properties methods of Cu-doped bismuth ferrite ($\text{BiFe}_{1-x}\text{Cu}_x\text{O}_3$) thin films. Chapter IV shows experimental results and discussions. Finally, the conclusion and suggestion are presented in chapter V.



CHAPTER II

LITERATURE REVIEW

2.1 Bismuth ferrite

Bismuth ferrite is materials which was well known by materials scientist. The materials were studied by many research methods such as nanoparticles, thin films, ceramic, solar cell catalyst, super capacitor. The perovskite structure ABO_3 within bismuth ferrite $BiFeO_3$ led to express multiferroic properties for magnetism, electricity and elasticity (Zhai *et al.*, 2015). Nevertheless, the magnetic and electrical properties are poor in bismuth ferrite nanoparticles. Therefore, it is challenge points for scientist to develop, improve, enhance, modified bismuth ferrite materials to better its original properties.

The structures of bismuth ferrite were classified into 3 space groups as rhombohedral $R3c$, cubic $Pm-3m$ and orthorhombic $Pbnm$ which are shown in figure 2.1. Each structure has different quantity of multiferroic properties. The most popular structure of bismuth ferrite which researcher interested was rhombohedral $R3c$ structure. The lattice parameters of rhombohedral $R3c$ are $a = 5.72 \text{ \AA}$, $\alpha = 59.02^\circ$, $b = 5.72 \text{ \AA}$, $\beta = 59.02^\circ$, $c = 5.72 \text{ \AA}$, and $\gamma = 59.02^\circ$. The rhombohedral $R3c$ structure can occur at synthesis temperature $600 - 820 \text{ K}$, orthorhombic $Pbnm$ $820-925 \text{ K}$ and cubic $Pm-3m$ above 925 K (Haumont *et al.*, 2005; Zhou *et al.*, 2012; Arnold *et al.*, 2009; Kadomtseva *et al.*, 2006; Siemons *et al.*, 2011).

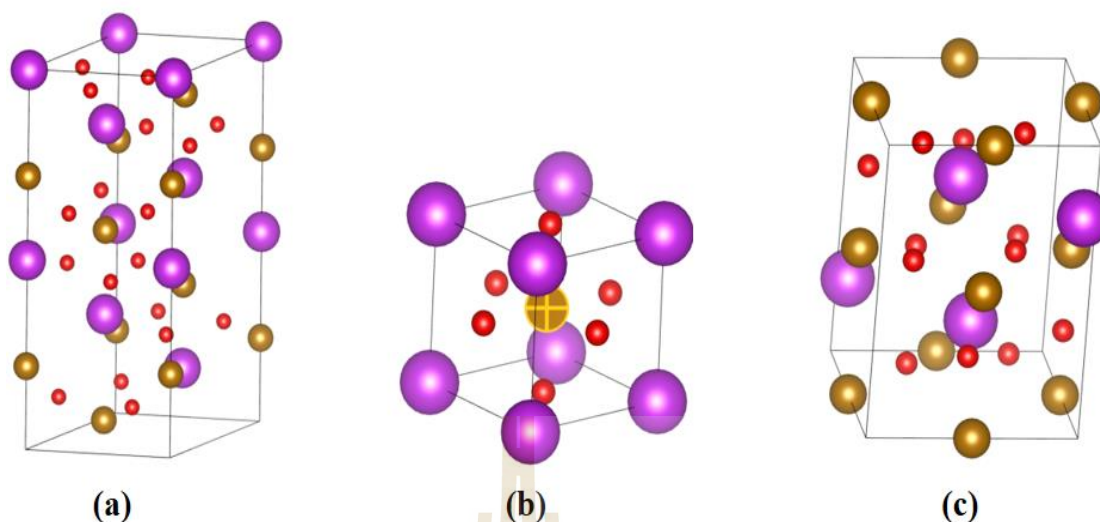


Figure 2.1 The bismuth ferrite space group (a) rhombohedral R3c, (b) cubic Pm-3m and (c) orthorhombic Pbnm (materialsproject.org).

2.1.1 Bismuth ferrite nanoparticles

Initially, the bismuth ferrite was popular researched in nanoparticles field. The nanoparticles are small size materials form which expressed better any properties than bulk materials such as magnetic properties, charge capacity, high specific area per volume (Yotburut *et al.*, 2017). The researcher has concerned to modify structure of BiFeO₃ nanoparticles such as substitution rare earth elements, changing precursor elements sources, using variant preparation methods. The nanoparticle can prepare with variant materials science methods such as sol-gel method, hydrothermal method, solid state combustion method. Sol-gel method is a simple method for prepare bismuth ferrite nanoparticles (Zhou *et al.*, 2012). The sol-gel method is a technique which were used to distribute initial elements by dissolving the elements in prepared solutions with stirrer machine. The optimal thermal temperature was applied between dissolving for homogeneous solution, this step is called condensation sol. Then, the precursors were

increased temperature to optimal temperature for forming gel, this step is called gelation (Qi *et al.*, 2006). Finally, the gel had been dried or super critical dried dependence of each materials condition. The sol-gel forming is shown in figure 2.2.

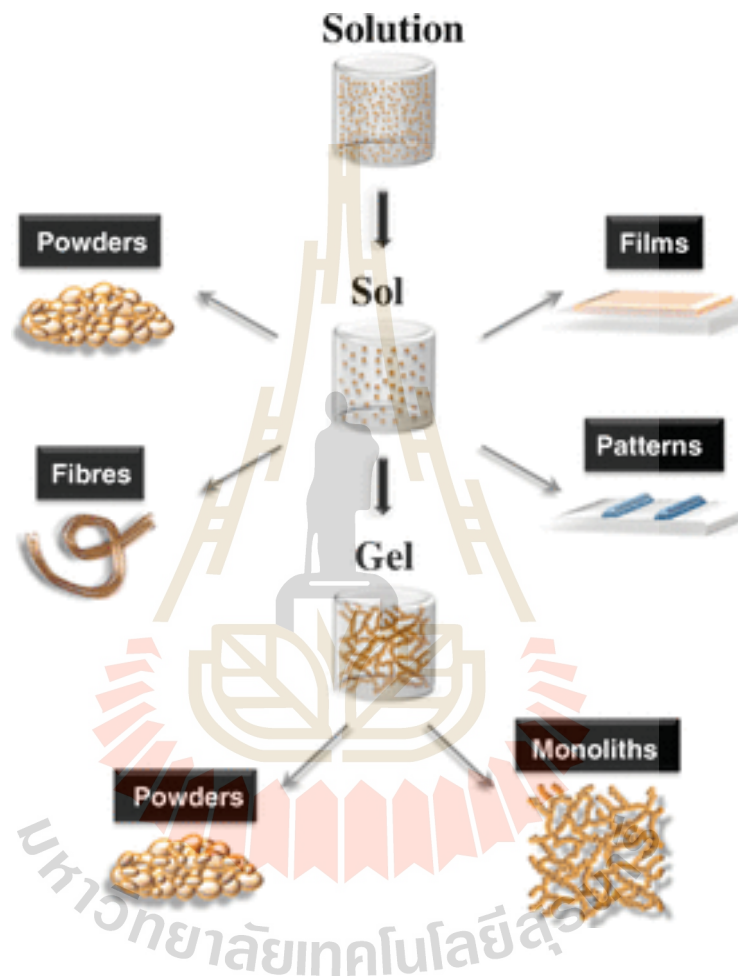


Figure 2.2 The sol-gel method for preparation initial precursor (Shirsath *et al.*, 2017).

For instances bismuth ferrite nanoparticles, the crystallite structure phase of bismuth ferrite nanoparticles show almost purity phase of rhombohedral R3c bismuth ferrite BiFeO_3 and some impurity phase dibismuth tetrairon (III) oxide $\text{Bi}_2\text{Fe}_4\text{O}_9$ for Cu-doped bismuth ferrite $\text{BiFe}_{1-x}\text{Cu}_x\text{O}_3$ that following figure 2.3. The crystallite sizes were about 66-88 nm. The bismuth ferrite nanoparticles were investigated particles size by

scanning electron microscope. The SEM images revealed particles size about 100-200 nm that following figure 2.4 (Khajonrit *et al.*, 2016)

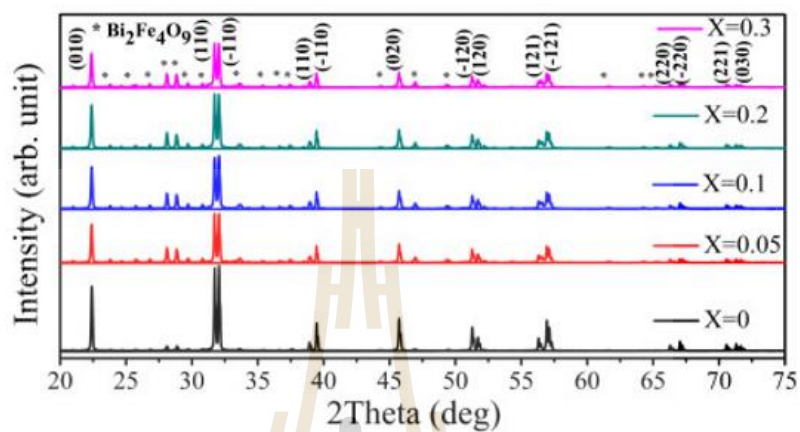


Figure 2.3 X-ray diffraction patterns of BiFe_{1-x}Cu_xO₃ (x = 0.0, 0.05, 0.1, 0.2 and 0.3) Nanoparticles (Khajonrit *et al.*, 2016).

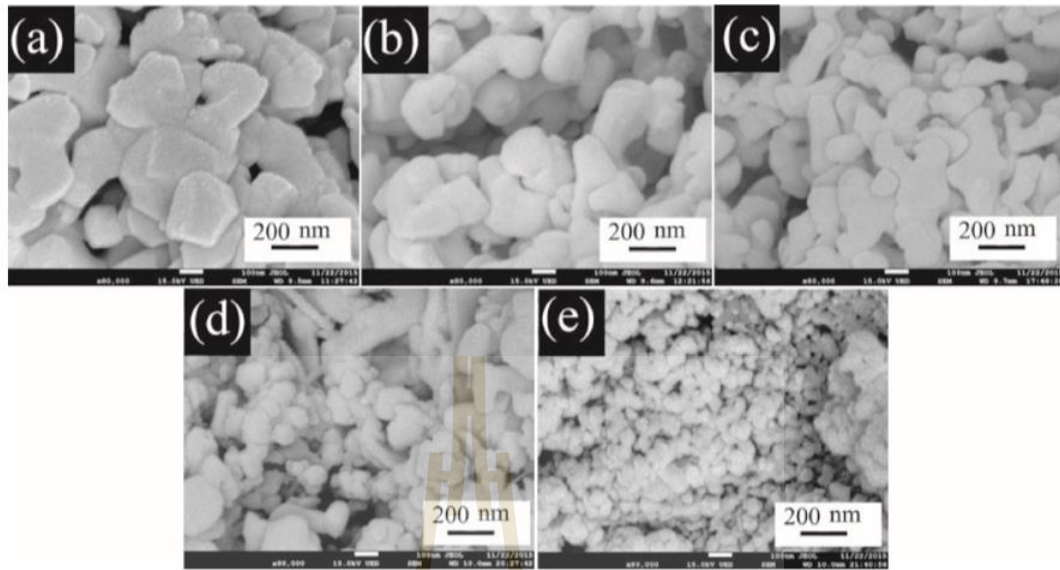


Figure 2.4 SEM images of $\text{BiFe}_{1-x}\text{Cu}_x\text{O}_3$ nanoparticles: (a) $x = 0$, (b) $x = 0.05$, (c) $x = 0.1$, (d) $x = 0.2$ and (e) $x = 0.3$ (Khajonrit *et al.*, 2016).

The electrical properties of Sm-doped bismuth ferrite $\text{Bi}_{1-x}\text{Sm}_x\text{FeO}_3$ nanoparticles revealed non-linear electrical enhancement. The non-linear was observed by increasing and decreasing of dielectric constant ϵ and loss tangent $\tan\delta$. The dielectric constant ϵ increased with increasing Sm concentration $x = 0.05-0.1$, but decreased when doped Sm concentration over than $x = 0.2$. The non-linear trend of dielectric constant ϵ was same the trend of loss tangent $\tan\delta$ dependence of Cu concentration that following figure 2.5 and 2.6 (Yotburut *et al.*, 2017). On the other hand, La-doped bismuth ferrite nanoparticles of $\text{Bi}_{1-x}\text{La}_x\text{FeO}_3$ revealed linear decreasing electrical enhancement.

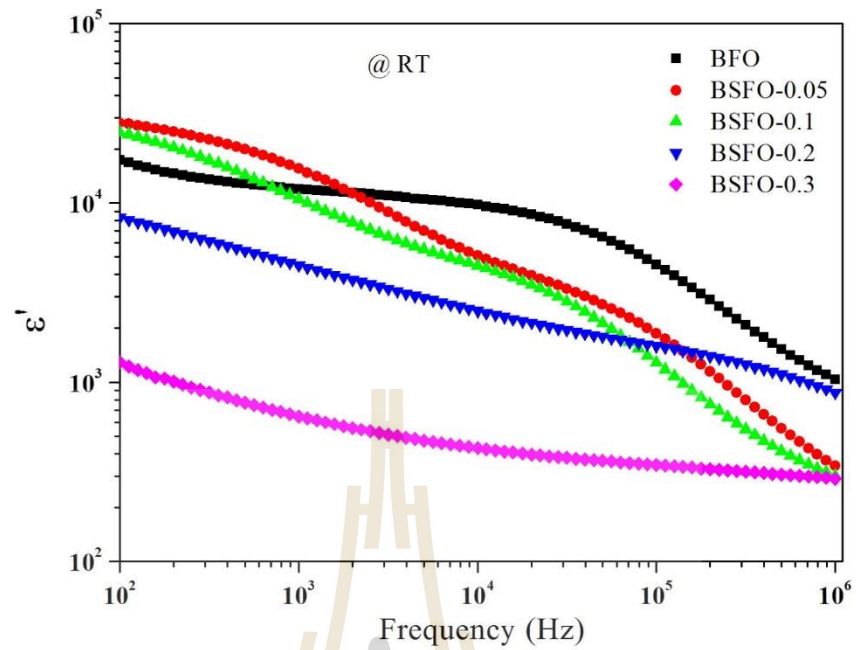


Figure 2.5 Frequency dependence of dielectric constant ϵ' at room temperature of $\text{Bi}_{1-x}\text{Sm}_x\text{FeO}_3$ ceramics (Yotburut *et al.*, 2017).

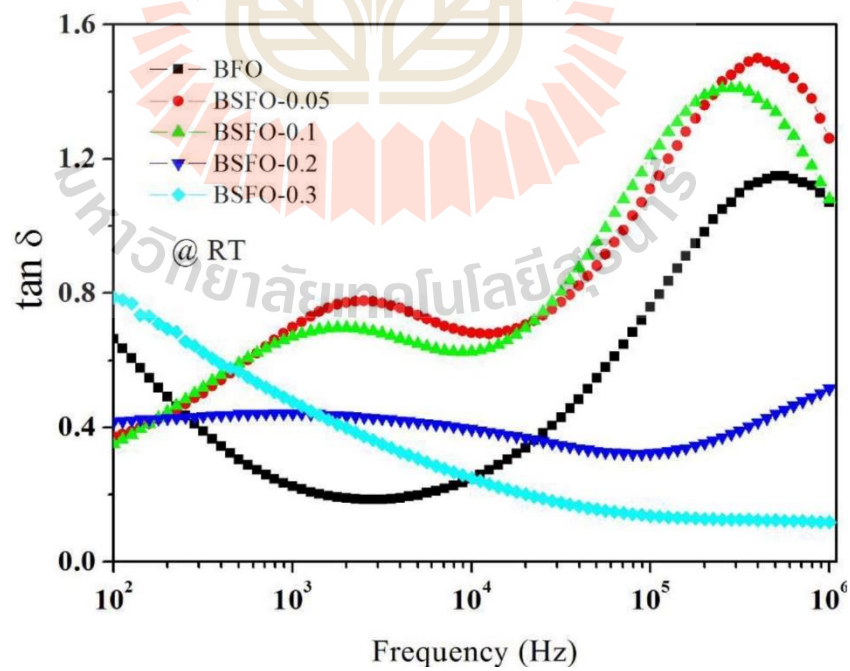


Figure 2.6 Frequency dependence of loss tangent $\tan \delta$ at room temperature of $\text{Bi}_{1-x}\text{Sm}_x\text{FeO}_3$ ceramics (Yotburut *et al.*, 2017).

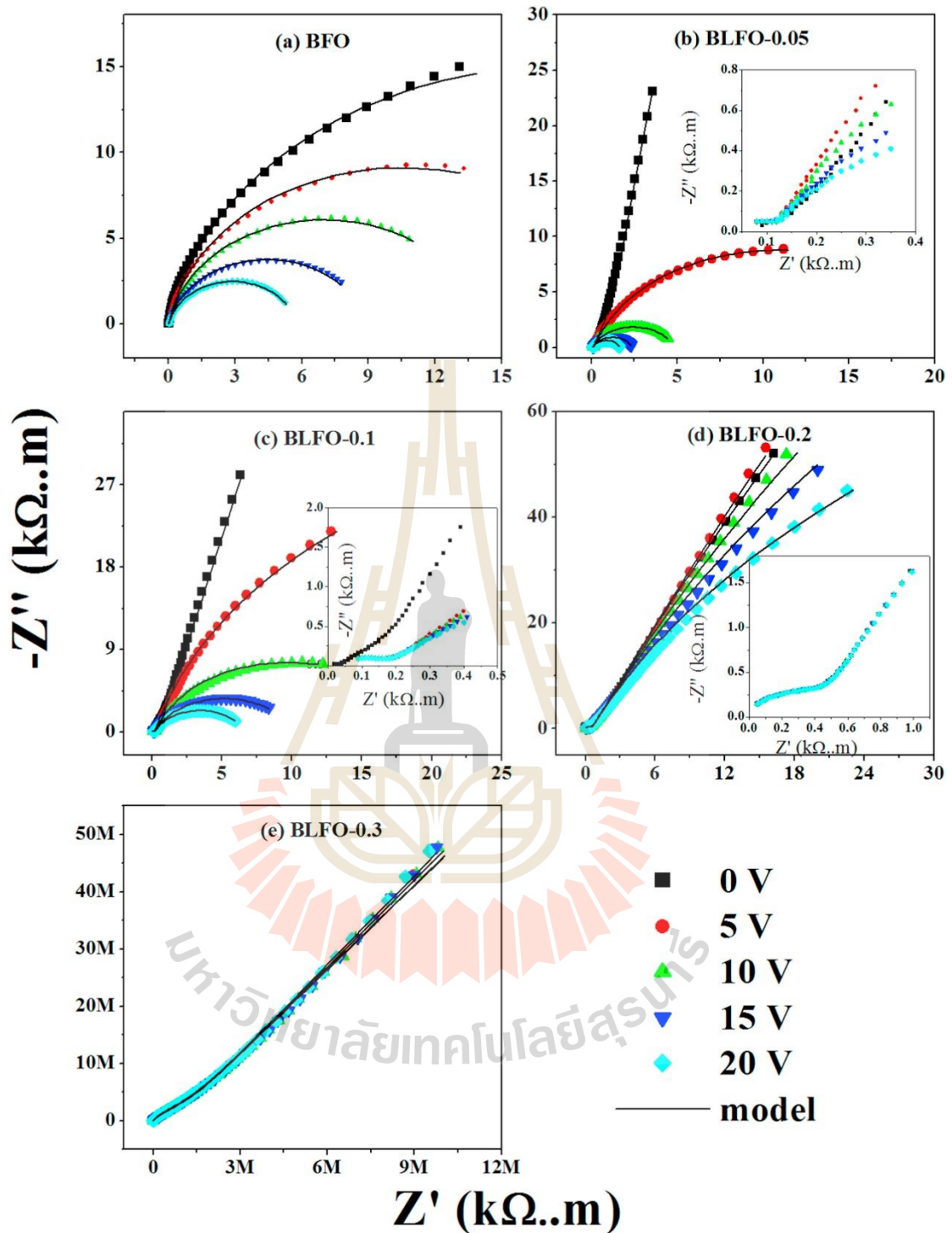


Figure 2.7 Impedance spectra as a function of applied dc bias for $\text{Bi}_{1-x}\text{La}_x\text{FeO}_3$ as (a) $x = 0.0$, (b) $x = 0.05$, (c) $x = 0.1$, (d) $x = 0.2$, and (e) $x = 0.3$ samples and high frequency region inset (b-d) (Yotburut *et al.*, 2017).

The decreasing of electrical properties were observed by complex impedance spectroscopy which showed increasing of grain boundary resistance R_{gb} of La-doped bismuth ferrite nanoparticles that following figure 2.7. The grain boundary resistance R_{gb} can be calculated by using brick-work model. The model proposes a parallel circuit of 2 resistance R_g, R_{gb} and 2 capacity C_g, C_{gb} that shows in figure 2.8.

The magnetic properties of BiFeO_3 nanoparticles were investigated by Cu-doped BiFeO_3 nanoparticles samples which were prepared by simple solution method (condensation part of sol-gel method) (Shirsath *et al.*, 2017). The research presented weak ferromagnetism of Cu doped bismuth ferrite nanoparticles (Khajonrit *et al.*, 2016). The saturation magnetization of Cu-doped BiFeO_3 nanoparticles increased with increasing Cu-doped for 0.07 to 0.55 emu/g, $x = 0.0-0.3$, respectively. The increasing weak ferromagnetism behaviour of Cu-doped BiFeO_3 nanoparticles were explained by nanoparticles size effect due to increasing of multi-domain particles and increasing crystallite structure of $\text{Bi}_2\text{Fe}_4\text{O}_9$.

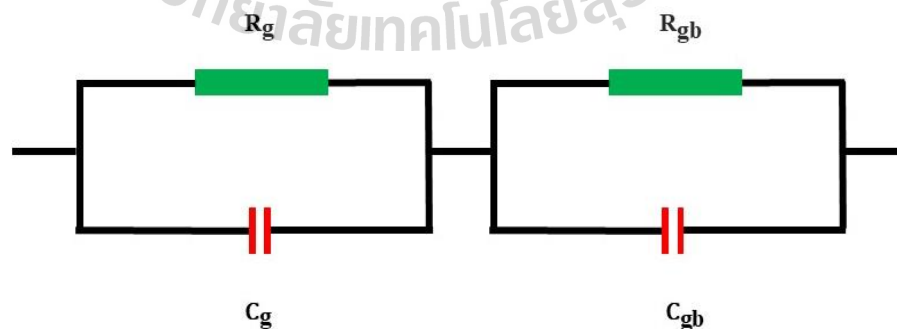


Figure 2.8 The ideal circuit of dielectric materials which shows circuit structure of grain (R_g, C_g) and grain boundary (R_{gb}, C_{gb}).

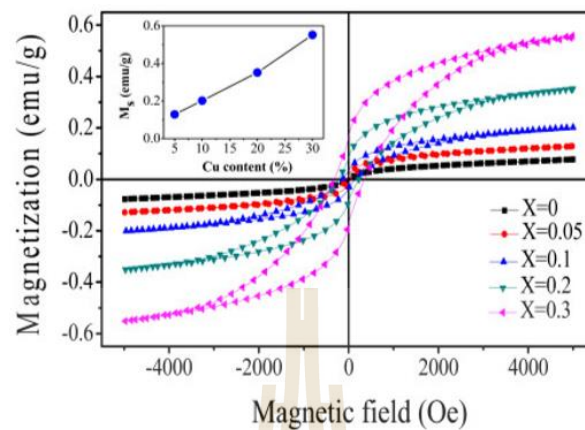


Figure 2.9 Room temperature M–H curves for $\text{BiFe}_{1-x}\text{Cu}_x\text{O}_3$ ($x = 0, 0.05, 0.1, 0.2,$ and 0.3) nanoparticles. Inset: Variations in saturation magnetization as a function of Cu content (%) (Khajonrit *et al.*, 2016).

2.1.2 Bismuth ferrite thin films

Bismuth ferrite thin films were done for modifying bulk materials to films layer dimension that led to better multiferroic properties because of its surface effect. The bismuth ferrite thin films can be prepared by various film fabrication methods such as high radio frequency sputtering, chemical vapor deposition, pulse laser deposition, dip coating, spin coating (Sharif *et al.*, 2018). The spin coating technique is a simple method and low cost equipment price when compared with other techniques (Wang *et al.*, 2010). The spin coating method needs to use initial precursors which were prepared by the sol-gel method. Then, the precursor had been deposited to optimal substrates, such as Pt/Si, Pt/Ti/FTO, Pt/Ti/SiO₂/Si, SrTiO₃/Si. Then, the dropped substrates were spun by spin coating machine with optimum rpm per a minute spinning rate. Next, the spun substrates were baked for drying the samples on substrates. Next, several cycles of

spinning and baking were done until got the anticipation films thickness. Finally, the samples were annealed at optimal temperature conditions. The bismuth ferrite thin films expressed multiferroic properties better than bismuth ferrite nanoparticles, according to multiferroic properties yield of rare earth doped bismuth ferrite thin films that shows in table 2.1.

For instances bismuth ferrite thin films, the x-ray diffraction pattern of bismuth ferrite thin films samples of BiFeO_3 and BFMC_2O_3 ($\text{BiFe}_{0.94}\text{Mn}_{0.04}\text{Cu}_{0.02}\text{O}_3$) thin films are shown in figure 2.10. The homogeneous of the thin films surface and the thin films thickness for 600-700 nm are shown in figure 2.11 (Dong *et al.*, 2014).

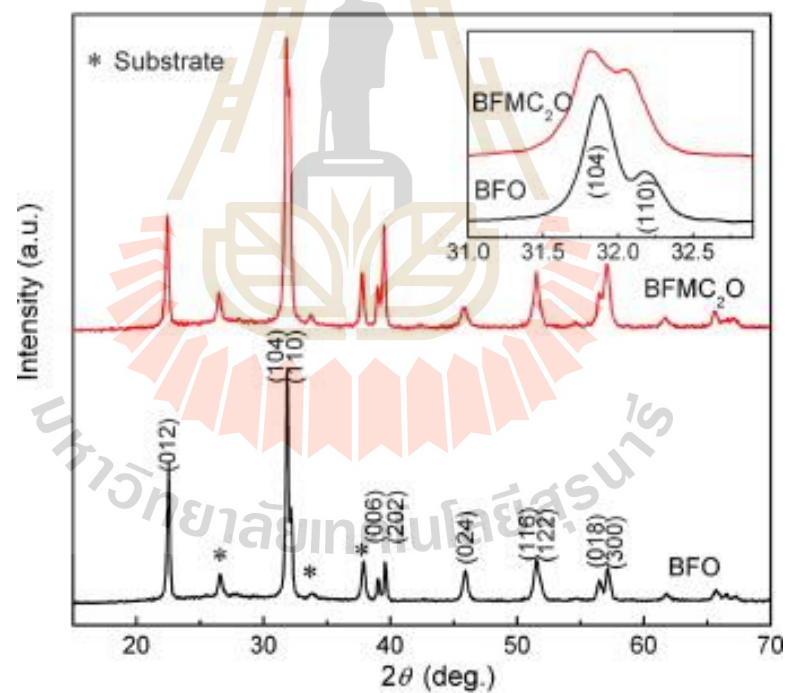


Figure 2.10 X-ray pattern of the pure BFO and BFMC_2O ($\text{BiFe}_{0.94}\text{Mn}_{0.04}\text{Cu}_{0.02}\text{O}_3$) thin films deposited on FTO substrates (Dong *et al.*, 2014).

The electrical properties of Mn-doped bismuth ferrite thin films presented improvement dielectric constant ϵ and loss tangent $\tan \delta$. The dielectric constant increased for $\epsilon \approx 84-105$ at 100 kHz. The same as loss tangent increased for $\tan \delta \approx 0.04-0.2$ at 100 kHz (Ren *et al.*, 2015). Normally, magnetic behavior of BiFeO_3 thin films are paramagnetism behavior. But, doping Mn elements enhanced weak ferromagnetic properties which observed with increasing coercivity $H_c \approx 50-150$ Oe, remanent magnetization $M_r = 0.1-0.5$ emu/cm³ and saturation magnetic $M_s = 0.8-5$ emu/cm³.

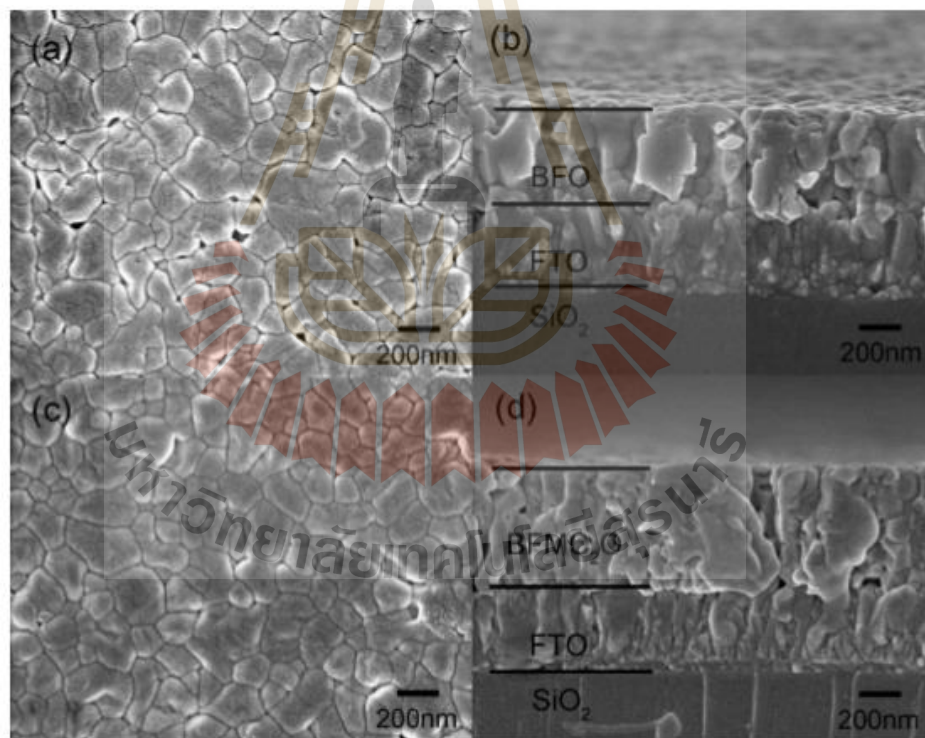


Figure 2.11 FE-SEM images of the surface and the cross-section micrographs BiFeO_3 (a and b) and BFMC_2O_3 (c and d) thin films (Dong *et al.*, 2014).

2.1.3 Experimental results overview of BiFeO₃

Table 2.1 Shows synthesis method, dielectric constant, loss tangent and magnetic parameters of rare earth doped BiFeO₃ thin films.

Materials	Synthesis	ϵ_r	$\tan \delta$	Ref.
Ho-doped BiFeO ₃	PLD thin films	120	0.4	(Sharif <i>et al.</i> , 2018)
Mn-doped BiFeO ₃	Sol-gel Spin coating this films	150	0.1	(Riaz <i>et al.</i> , 2015)
(1-x)BiFeO ₃ - x(SrTiO ₃ - Bi _{0.5} Na _{0.5} TiO ₃)	Solid state reaction	800	0.09	(Qian <i>et al.</i> , 2017)
La-doped BiFeO ₃	Simple precipitation ceramic	5×10^4	1.5	(Yotburut <i>et al.</i> , 2017)
Sm-doped BiFeO ₃	Simple precipitation	1.1×10^4	-	(Yotburut <i>et al.</i> , 2017)

Table 2.1 Shows synthesis method, dielectric constant, loss tangent and magnetic parameters of rare earth doped BiFeO₃ thin films (Continued).

Materials	Synthesis	ϵ_r	$\tan \delta$	Ref.
BiFeO ₃ on Ni tapes	CVD thin films	140	-	(Tang <i>et al.</i> , 2014)
La-doped BiFeO ₃	Sol-gel method	680	-	(Wu <i>et al.</i> , 2015)
0.6SrBiNbO ₃ - 0.4BiFeO ₃	Spin coating thin films	380	0.02	(Xue <i>et al.</i> , 2004)
BiFeO ₃	RF deposition thin films	115	0.5	(Jian <i>et al.</i> , 2013)

Table 2.2 Shows saturation magnetization, remanent magnetization and coercive force of rare earth doped BiFeO₃ thin films.

Materials	Synthesis	M_s	M_r	H_c	Ref.
Ho-doped BiFeO ₃	PLD thin films	18 kA/m	4 kA/m	15 kA/m	(Sharif <i>et al.</i> , 2018)
Mn-doped BiFeO ₃	Sol-gel Spin coating this films	102 emu/cm ³	-	-	(Riaz <i>et al.</i> , 2015)
(1-x)BiFeO ₃ - x(SrTiO ₃ - Bi _{0.5} Na _{0.5} TiO ₃)	Solid state reaction	0.4 emu/g	0.1 emu/g	18 kOe	(Qian <i>et al.</i> , 2017)
Cu-doped BiFeO ₃	Simple solution	0.55 emu/g	0.2 emu/g	0.2 kOe	(Khajonrit <i>et al.</i> , 2016)
Ca-doped BiFeO ₃	Sol-gel method	8 emu/g	0.4 emu/g	40 Oe	(Dhir <i>et al.</i> , 2017)
La-doped BiFeO ₃	Sol-gel method	0.29 emu/cm ³	0.14 emu/cm ³	5 kOe	(Wu <i>et al.</i> , 2015)

Table 2.2 Shows saturation magnetization, remanent magnetization and coercive force of rare earth doped BiFeO₃ thin films (Continued).

Materials	Synthesis	M_s	M_r	H_c	Ref.
La-doped BiFeO ₃	PLD thin films	14.8 emu/cm ³	2.6 emu/cm ³	523 Oe	(Kumar <i>et al.</i> , 2010)
Pr, Mn co-doped BiFeO ₃	Solid state reaction	0.22 emu/g	-	-	(Krishnaswamy <i>et al.</i> , 2015)
BiFeO ₃	RF deposition thin films	3.5 emu/cm ³	0.4 emu/cm ³	200 Oe	(Jian <i>et al.</i> , 2013)
Mn, Cu co-doped BiFeO ₃	CVD thin films	5.25 emu/cm ³	0.5 emu/cm ³	80 Oe	(Dong <i>et al.</i> , 2014)

2.2 Polarization and electrical properties of materials

2.2.1 Dielectric polarization

The polarizations within materials were classified by relaxation time. These polarizations responding depended on frequency and potential of electric field. The materials which have stayed among electric field, are split its charges elements (Hole and electron) from its equilibrium atoms. Fundamentally, dielectric polarizations were classified to electronic polarizations, atomic polarizations, orientation polarizations and interfacial polarizations (Hench, L. L. and West, J. K., 1990). Basically, the definition of each polarization is described follows.

2.2.1.1 Electronic/Atomic polarization

Occurrence of the electronic polarization when dielectric materials atoms were separated holes and electrons charges within an atom. These separations have occurred due to applied external electric field to dielectric materials. Then, these separations created off-center charges element within materials atoms and led to electric/atomic polarization. The optimal frequencies of the polarization are above 10^{15} Hz. However, it needs to consider to optimal potential voltage of external electric field.

2.2.1.2 Ionic polarization

The ionic polarization is involved with bounding between positive ion and negative ion of dielectric materials paired atoms, which the paired atoms have been applied external electric field. Then, the paired atoms created a dipole moment between positive ion and negative ion due to difference electronegativity of an ion atom. The optimal frequencies of the polarization are about 10^{12} - 10^{13} Hz.

2.2.1.3 Dipole/Orientation polarization

The dipole polarization is used to describe dipole molecules of dielectric materials. The independence of dipole molecules can change direction charge poles freely within dielectric materials. The directions of dipole are thermal randomization when the external electric field has been applied through the dipole molecules of materials. Then, the dipole molecules directions are arrayed following the direction of the net external electric field. The optimal frequencies of the polarization are about 10^6 - 10^8 Hz.

2.2.1.4 Interface/Space-Charge polarization

The interface polarization is a polarization which depends on charge mobility or limitation of charge mobility within dielectric materials grain. The charge mobility is involved with grain, grain boundary of materials. The polarization is considered on complex impedance spectra and electrode interface. The optimal frequencies of the polarization are below 10^5 Hz.

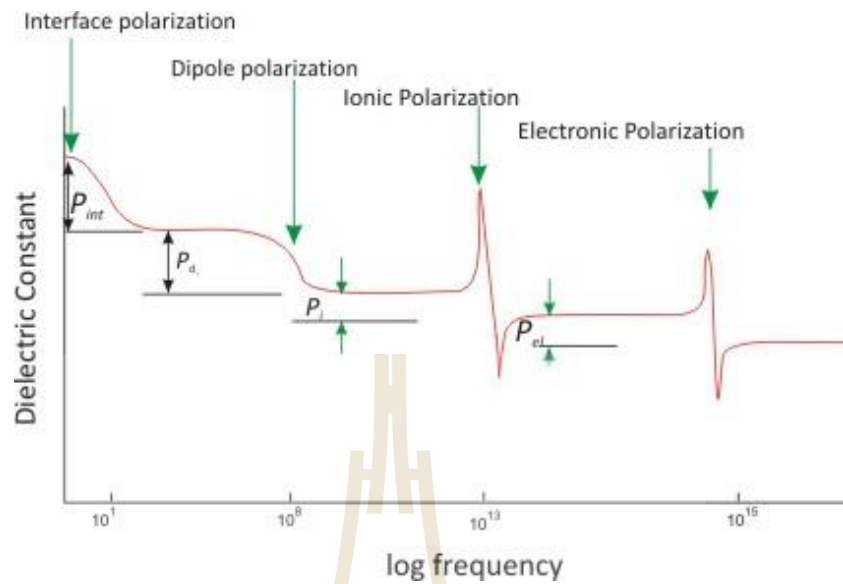


Figure 2.12 Frequency dependence of polarization of dielectric materials (https://nptel.ac.in/courses/113104005/lecture20/20_2.htm).

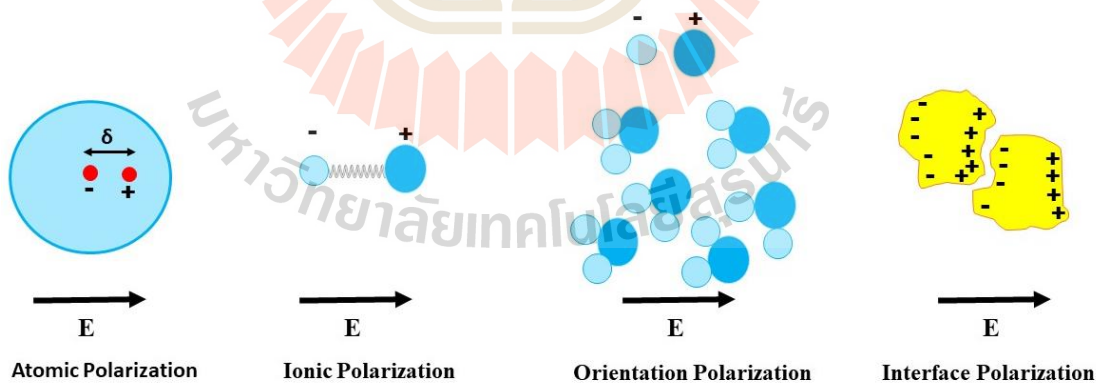


Figure 2.13 The polarization mechanism of each polarization type of dielectric materials (Adapt from Hench L. L., and West J. K., 1990).

2.2.2 Interaction of dielectric and polarization among electric field

The dielectric permittivity is related to total polarization yield of dielectric materials which were placed among alternating electric field. The dielectric permittivity ϵ^* can be described by occurrence polarization within dielectric materials by the following equations

$$\vec{P}_{total} = \vec{P}_{ele} + \vec{P}_{ion} + \vec{P}_{Dip} + \vec{P}_{int} + \vec{P}_{\infty} \quad (2.1)$$

Where P_{total} is restructure yield of total polarization, P_{ele} is electrical polarization, P_{ion} is ionic polarization, P_{Dip} is dipole polarization, P_{int} is interface polarization and P_{∞} is another else polarization. The relation between polarizations and dielectric permittivity can be considered by occurrence polarization.

$$\vec{D} = \epsilon_0 \vec{E} + \vec{P}_{total} \quad (2.2)$$

$$\vec{D} = \epsilon_{permitt}^* \vec{E} \quad (2.3)$$

$$\vec{P}_{total} = \vec{E}(\epsilon_{permitt}^* - \epsilon_0) \quad (2.4)$$

Where \vec{D} is total electric filed in dielectric materials, ϵ_0 is permittivity in space, \vec{E} is electric field, \vec{P}_{total} is polarization within dielectric materials, $\epsilon_{permitt}^*$ is dielectric permittivity. So, the complex dielectric constant can be given by following equations

$$\epsilon^* = \frac{\epsilon_{permitt}^*}{\epsilon_0} \quad (2.5)$$

Where ϵ^* is complex dielectric permittivity constant. From equation 2.4 and 2.5, the polarization can express following equation.

$$\vec{P}_{total} = \vec{E}(\epsilon^* \cdot \epsilon_0 - \epsilon_0) \quad (2.6)$$

$$\epsilon^* = \frac{\vec{P}_{total}}{\epsilon_0 \cdot \vec{E}} + 1 \quad (2.7)$$

2.2.3 Dielectric permittivity constant and alternating electric fields

Alternating electric fields are a factor of polarization and electrical properties phenomenon within dielectric materials. Those electrical interactions can be changed with dependence of frequency and alternating electric potentials voltage. The interactions led to polarization theorem, complex impedance model, thought piezoelectric effect. The relations of dielectric permittivity and alternating electric field can be explained by time dependent charges mobility of alternating current with sinusoidal potentials voltage that following equation.

$$I = \frac{dQ}{dt} = \frac{CdV_{ac}}{dt} \quad (2.8)$$

Where I^* is electric current, $Q = C^*V^*$ is electric charges, $V^* = V \exp^{i\omega t}$ is time dependent potentials voltage and C^* is complex capacitance. So, the equation (2.8) can be dispersed to real part and imaginary part by exponential property

$$I^* = \frac{C^* dV^*}{dt} = j\omega C^* V^* \quad (2.9)$$

$$I^* = j\omega V^* C_0 (\cos \omega t + j \sin \omega t) \quad (2.10)$$

For ideal complex dielectric circuit, the $C_0(\cos \omega t + j \sin \omega t)$ has been replaced by dielectric permittivity ε^* . So, the equation (2.10) were reduced to following form.

$$I^* = j\omega V^* C_0 \varepsilon^* \quad (2.11)$$

Which the dielectric permittivity ε^* is consisted of real part and imaginary part.

$$\varepsilon^* = \varepsilon' - j\varepsilon'' \quad (2.12)$$

Where ε' is real part of dielectric permittivity called dielectric constant and ε'' is imaginary part of dielectric permittivity called dielectric loss.

The dielectric constant is used to indicate insulator properties of dielectric materials. While the dielectric loss indicates to leakage current of dielectric materials. The proportion of dielectric loss and dielectric constant is represented by dissipation factor term “ $\tan \delta$ ”. The dissipation factor is used to describe quantity of energy losses in dielectric materials.

2.2.4 Dielectric permittivity constant and complex impedance spectroscopy

The complex impedance spectroscopy is a theorem which are used to describe electrical mobility interactions within dielectric materials. The interactions are defined by essential parameters for studying and indicating structure of dielectric properties. So, the ideal complex impedance gives dielectric properties in form of two RC circuits parallel of R_g , C_g , R_{gb} and C_{gb} . Where R_g is grain resistance, C_g is grain capacitance, R_{gb} is grain boundary resistance and C_{gb} is grain boundary capacitance. The complex impedance under alternating electric current and voltage potential are explained by following equation.

$$Z^* = \frac{V^*}{I^*} \quad (2.13)$$

Where Z^* is the complex impedance, V^* is alternating voltage potential and I^* is alternating electric current. The Z^* can calculate from following equation 2.13-2.14.

$$Z^* = \frac{1}{j\omega C_0 \varepsilon^*} \quad (2.14)$$

Where $\varepsilon^* = \varepsilon' - j\varepsilon''$, $\omega = 2\pi f$, $C_0 = \frac{\varepsilon_0 A}{d}$, ε' is real part of dielectric permittivity, ε'' is imaginary part of dielectric permittivity, C_0 is capacitance of sample, A is interface area of sample and d is thickness of sample.

The complex impedance spectra Z^* can explain grain, grain boundary and electrical properties of dielectric materials with expression complex impedance Z^* that following equation.

$$Z^* = Z' - jZ'' \quad (2.15)$$

$$Z' - jZ'' = \frac{1}{R_g^{-1} + j\omega C_g} + \frac{1}{R_{gb}^{-1} + j\omega C_{gb}} \quad (2.16)$$

$$Z' = \frac{R_g}{1 + (\omega C_g R_g)^2} + \frac{R_{gb}}{1 + (\omega C_{gb} R_{gb})^2} \quad (2.17)$$

$$Z'' = R_g \left[\frac{\omega C_g R_g}{1 + (\omega C_g R_g)^2} \right] + R_{gb} \left[\frac{\omega C_{gb} R_{gb}}{1 + (\omega C_{gb} R_{gb})^2} \right] \quad (2.18)$$

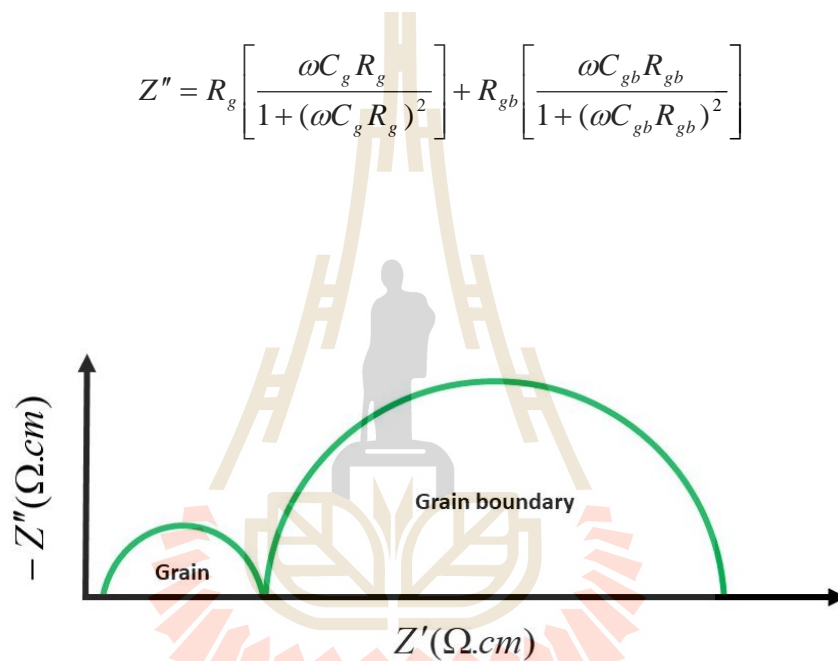


Figure 2.14 Shows ideal complex impedance spectroscopy which consist of grain part and grain boundary part.

2.3 Magnetism and magnetic properties of materials

2.3.1 Magnetism materials

Magnetism materials are materials which express magnetic behavior spontaneously or magnetic responding when applied external magnetic fields. Naturally, the materials which occurred magnetism are called permanence magnet materials. The materials which have occurred magnetic behavior after applied external magnetic fields, are called magnetism materials. The magnetism materials can be classified to types of magnetism by magnetic responding quantity with applying external magnetic field (Supree Pinitsoontorn, 2015). The magnetism can be possible applied to electrical device, communication technology, computer technology. So, magnetic fundamental is an important knowledge which deserving study, and research.

2.3.2 Magnetic field

The magnetic field is a magnetic factor which led to indication magnetic responding quantity of magnetism materials. The magnetic field occurred under permanence magnetic because of strongly magnetic moments yield within permanence magnetic materials which built magnetic dipole and magnetic field between the magnetic poles. The strongly of magnetic field are dependence magnetic flux intensity of magnetic poles that shows in figure (2.15).

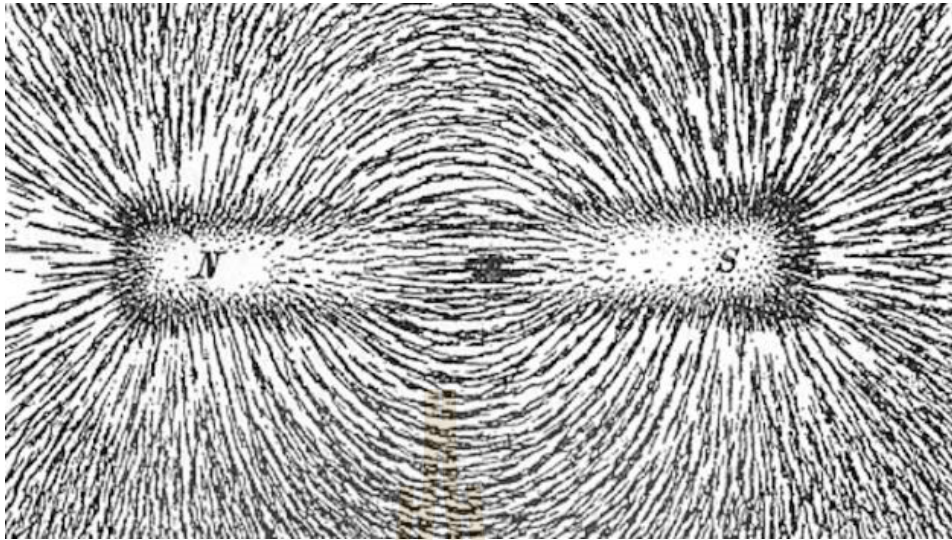


Figure 2.15 Magnetic field of permanent magnetism materials (www.electrical4u.com/magnetic-field).

The magnetic field can also occur under flowing charges around electric conductor wire. The charges mobility can produce magnetic field around its mobility direction. The direction of magnetic fields can be indicated by using Right-Hand rule (Supree Pinitsoontorn, 2015).

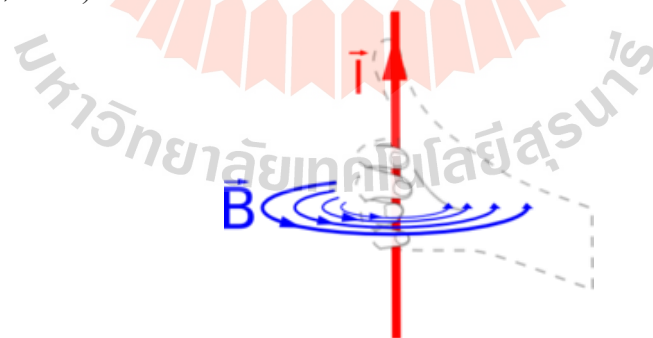


Figure 2.16 Shows electromagnetic field and Right Hand rule for indication direction of magnetic field as \vec{I} is electric current and \vec{B} is magnetic (<https://scienceblogs.com/startswithabang/2009/04/10/the-left-hand-rule>).

The quantity of magnetic field can be calculated by using Ampere's law and Biot-Savart law. For Ampere's law, Ampere had observed behavior of magnetic field and charge current, then explained that the occurrence of magnetic field is dependent on direction and quantity of charges mobility. The Ampere's law is presented in integral magnetic field term of charges mobility's closed direction.

$$\oint \vec{H} d\vec{l} = I \quad (2.18)$$

Where \vec{H} is magnetic field, \vec{l} is length of charges conductor wire and I is total charges current.

For Biot-Savart law, sub magnetic field are expressed by charges cluster I flowing within charges conductor wire $d\vec{l}$ that following equation.

$$d\vec{H} = \frac{1}{4\pi r^2} I d\vec{l} \times \vec{r} \quad (2.19)$$

Where \vec{r} is distance from charges conductor to sub magnetic field which was used to calculate sub-magnetic field. The total magnetic field can be calculated by integral term that shows in equation (2.20).

$$\vec{H} = \int_a^b \frac{1}{4\pi r^2} I d\vec{l} \times \vec{r} \quad (2.20)$$

The intensity of magnetic field can be considered in term of magnetic flux. The magnetic flux supposed to describe magnetic field intensity that the magnetic field consisted with many of magnetic fluxes. The relations between magnetic flux and magnetic field are shown in equation 2.21.

$$\Phi = \mu_0 \int \vec{H} \cdot d\vec{A} \quad (2.21)$$

$$\Phi = \mu_0 \vec{H} \cdot \vec{A} \quad (2.22)$$

Where Φ is magnetic flux, μ_0 is permeability in space and \vec{A} is an area which is used to calculate magnetic flux. The importance law for describing magnetic flux are well known as Gauss's law and Faraday's law. Gauss's law had explained that the magnetic field a direction is existence between magnetic dipole N, S. So, the summation of vector magnetic field yield at closed surface must equal zero following equation.

$$\mu_0 \oint_s \vec{H} \cdot d\vec{A} = 0 \quad (2.23)$$

For Faraday's law had described his discovery that alternating magnetic flux dependence of induced occurrence electromotive force EMF phenomenon within solenoid coil. This phenomenon has been applied the electric generator and called dynamo. This phenomenon can be described by following equation.

$$EMF = -N \frac{d\Phi}{dt} \quad (2.24)$$

Where N is number of solenoid coil.

2.3.3 Magnetic inductor

Magnetic inductor \vec{B} is a vector which almost is the same as \vec{H} , but the magnetic inductor is used to describe flux density per area within magnetism materials. The equation which explained magnetic inductor that following equation (Maciej U. *et. al.*, 2012).

$$B = \frac{\Phi}{A} \quad (2.25)$$

The magnetic inductor and magnetic field almost the same thing in space. However, the relation of magnetic inductor and magnetic within middle can give by that equation.

$$\vec{B} = \mu \vec{H} \quad (2.26)$$

Where μ is permeability within intermediary. The μ can change dependence intermediary.

2.3.4 Magnetic moment

Magnetic moment is a yield of magnetic moment torque which occurred within magnetic materials. The magnetic moment mechanism was explained by orbital magnetic moment M_{orbit} and spin magnetic moment M_{spin} of electrons shell orbitals within magnetic materials.

2.3.4.1 Orbital magnetic moment

The orbital magnetic moment in term of an atom can be described by basically an atom model of a nucleus and an electron which the electron orbits around

the nucleus. From Ampere's law, the magnetic moment in atom model was explained by following equation.

$$I = \frac{Q}{t} = \frac{e}{T} = \frac{ev}{2\pi r} \quad (2.27)$$

Where e is electron charge, T is a time period of electron orbit ($T = \frac{2\pi r}{v}$), and r is a distance between nucleus center and an electron. So, the orbital magnetic moment of single atom can be considered by electron mobility orbits around nucleus center which can figure out as small electric current mobility in a small circle conductor wire. So, the orbital magnetic moment can be calculated by following equation.

$$M_{orbit} = I \cdot A \quad (2.28)$$

$$M_{orbit} = \left(\frac{ev}{2\pi r} \right) \cdot \pi r^2 \quad (2.29)$$

$$M_{orbit} = \frac{evr}{2} = \left(\frac{e}{2m_e} \right) \cdot L_0 \quad (2.30)$$

$$M_{orbit} = \left(\frac{e}{2m_e} \right) \cdot L_0 \quad (2.31)$$

Where A is electron orbit area, m_e is mass of an electron, v is an electron velocity and L_0 is angular momentum orbital ($L_0 = m_e v r$).

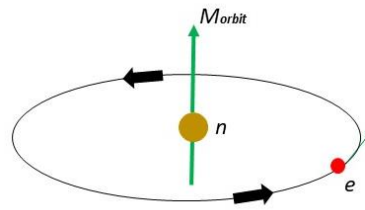


Figure 2.17 Shows orbital magnetic moment within a single atom model.

2.3.4.2 Spin magnetic moment

Other magnetic moment inside a single atom is a spin magnetic moment. The spin magnetic moment occurred due to self-orbit of electron and neutron. These orbiting are the same a small circular charge mobility. The orbited induced magnetic moment which perpendicular with orbited direction. Spin magnetic moment was described by the same equation as orbital magnetic moment. But, the spin magnetic moment is multiplied by g parameter or called g -factor. This factor is a quantity which expressed the magnetic moment characteristic of each particle. So, g -factor are difference for different particles that following equation.

$$m_{ele,spin} = g_e \frac{e}{2m_e} L_e \quad (2.31)$$

Where $m_{ele,spin}$ is spin magnetic moment of electron, g_e is g -factor of electron and L_e is angular magnetic moment of electron.

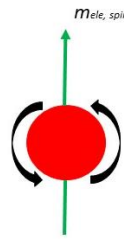


Figure 2.18 Shows spin magnetic moment within a single electron.

2.3.5 Magnetic parameters and hysteresis loop

2.3.5.1 Magnetic parameters

The magnetic properties of magnetism materials can be indicated by variant magnetic parameters such as magnetic field H , magnetic inductor B , magnetization M , saturation magnetization M_s , remanent magnetization M_r , magnetic coercivity H_c , magnetic susceptibility χ . Relations between the parameters are explained by basically magnetic equations. However, an essential parameter is magnetic field H (Goldfarb R. G. *et al.*, 1985). The magnetic field H is a parameter which is used to induce magnetization within magnetism materials. The density of magnetic flux per area of magnetic field is shown in form magnetic inductor B , at equation 2.32. The magnetic inductor B can change its quantity when change an intermediary. But, the magnetic field H still be the original quantity. So, relation between magnetic field and magnetic inductor can describe with following equation.

$$\vec{B} = \mu_0 \vec{H} \quad (2.32)$$

$$\vec{B} = \mu \vec{H} \quad (2.33)$$

Where μ_0 is magnetic permeability in space and μ is magnetic permeability in an intermediary.

Magnetism materials are explained by expression of magnetization. The magnetization of the materials is presented by proportional of material's moment magnet per volume or mass. So, the magnetization can consider in term of mass and volume that are shown in equation.

$$M_v = \frac{m}{V} \quad (2.34)$$

$$M_w = \frac{m}{w} \quad (2.35)$$

Where M_v is magnetization magnet by volume, M_w is magnetization magnet by weight, m is magnetic moment, V is materials volume and w is materials weight.

The relation between B and H parameters of magnetism materials were given by following equation.

$$B = \mu_0(H + M) \quad (2.36)$$

$$B = \mu_0(H + M) \quad (2.37)$$

$$B = \mu_0 H \left(1 + \frac{M}{H}\right) \quad (2.38)$$

$$\mu = \frac{B}{H} = \mu_0(1 + \chi) \quad (2.39)$$

Where χ is proportion of magnetization per magnetic field which is called magnetic susceptibility.

2.3.5.2 Hysteresis loop

Actually, magnetic hysteresis loop is a magnetism measurement technique, which is used to investigate magnetic properties of magnetism materials. The magnetic hysteresis loop can be used to classify kinds of magnetism materials. The hysteresis loop occurred due to changing of magnetic moment responding within materials with applying external magnetic fields H . While the external magnetic field has been applied from 0 to H , the material's magnetization is induced from 0 to M . The initial slope of $M-H$ with applying any external magnetic is called initial susceptibility χ , that is shown in equation 2.39. Then, the highest of magnetization is called saturated point or saturation magnetization M_s (F. Karl *et al.*, 1997). Then, the external magnetic field has been increased from H to 0. So, the magnetization is decreased from M_s to M_r because of decreasing of applying external magnetic field from H to 0. The M_r is magnetization remaining of magnetism materials when the applying external magnetic field. Then, external magnetic field has been decreased from 0 to $-H_c$ while the magnetization is decreased from M_r to 0. The H_c is called magnetic coercive force, which induced remanent magnetization to zero. Next, the magnetic field has been decreased from $-H_c$ to $-H$ while the magnetization is induced to saturated point again, but as the opposite direction $-M_s$. Next, the external magnetic has been changed for $-H \rightarrow 0 \rightarrow H_c$ $H_c \rightarrow H \rightarrow 0$. Finally, the graph of magnetization M loop versus magnetic field H is expressed. The hysteresis graph of $M-H$ is shown in figure 2.19.

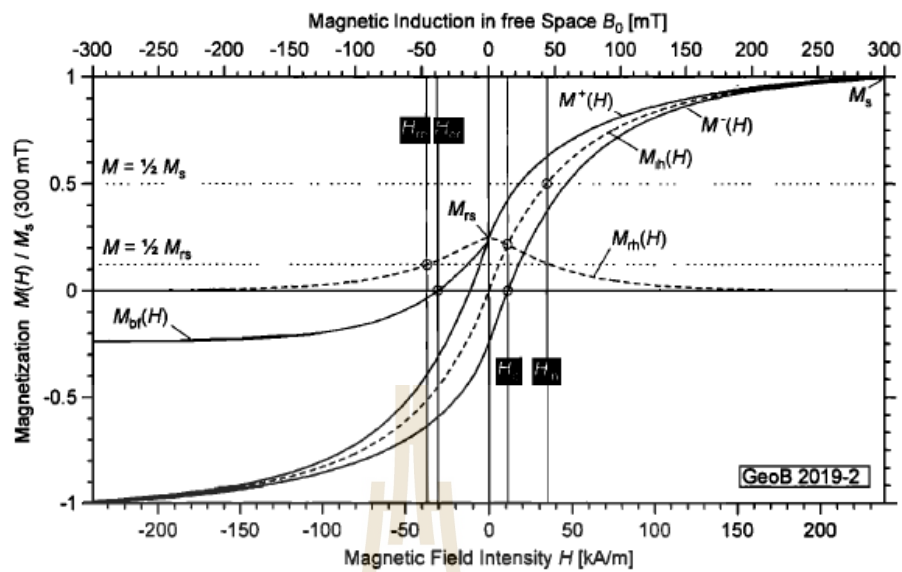


Figure 2.19 Shows simulated magnetic hysteresis loop graph of M - H (Fabian and von Dobeneck, 1997).

2.3.6 Classification of magnetism materials and theory

2.3.6.1 Classification of magnetism materials

The materials are classified to magnetic kinds by responding of its magnetization with applying external magnetic field. Normally, the magnetism materials can be indicated magnetic kinds by using magnetic susceptibility χ and coercive force H_c . So, the classification of magnetism materials is shown in table 2.3 and figure 2.24.

Table 2.3 Classification table of magnetism materials and indicator parameters (Supree Pinitsoontorn, 2015).

Magnetic kinds	Magnetic Behavior	Materials
Diamagnetic	The diamagnetism materials are consisted of too small magnetic moment, and express opposition magnetic moment with applying external magnetic field. The magnetic susceptibility χ is stayed between -10^{-6} to 10^{-5} .	Normally, the diamagnetism materials are inert gases and some materials such as Ar, He, Ne, Cu, Au, Hg, NaCl, CaCl ₂ .
Paramagnetic	The paramagnetism materials are consisted of magnetic moment random arrangements. The magnetic moment yield expressed some magnetization with applying external magnetic field. The magnetic susceptibility is stayed between 10^{-5} to 1.	Instance of paramagnetism materials are diatom gases, metals element, some salt compound atom, rare earth oxide such as O ₂ , NO, Al, Mg, Bi ₂ O ₃ .

Table 2.3 Classification table of magnetism materials and indicator parameters (Supree Pinitsoontorn, 2015) (Continued).

Magnetic kinds	Magnetic Behavior	Materials
Antiferromagnetic	<p>The antiferromagnetism materials have occurred due to good alignment of its magnetic moment, which are consisted of 2 magnetic moments alignment direction. The magnetic moment yield is the same as paramagnetism materials at above neel temperature. But, at below neel temperature. The magnetic susceptibility is between 10^{-5} to 1.</p>	<p>Instance of antiferromagnetism materials are some transition elements, metals oxide, ABO_3 structures such as Mn, CO_2, Fe_2O_3, Cu_2O_3, MnO.</p>
Ferromagnetic	<p>The magnetic moments of ferromagnetism materials are aligned by good regular alignment. So, the magnetic moment yield is too strong. The magnetic susceptibility more than 1.</p>	<p>Instance of ferromagnetism materials are transition metals, metals oxide, alignment moment magnet atom structure such as Co, Ni, Fe, FeO, $FeO-Fe_2O_3$, $CuO-Cu_2O_3$.</p>

2.3.6.2 Diamagnetism materials

The diamagnetism mechanism occurred due to the electrons shell orbital of atom were fulfilled with electron pair of every electron shells, according to Russell-Saunders coupling and Hund's rules. So, the responding of magnetic moment or spin-orbit vector summation are too small with applying external magnetic field. These hypotheses are reasonable of weak magnetization and small magnetic susceptibility, which occur within diamagnetism materials. However, the diamagnetism materials can be applied to scientist equipment with some devices for protection disturbance of environment magnetic field such as magnetic earth.

Due to magnetism of materials was mostly described by orbital and spin magnetic moment. So, the theorems for explaining spin and orbital magnetic of moment yield are Russell-Saunders coupling and Hund's rules (Supree Pinitsoontorn, 2015).

The Russell-Saunders coupling has been defined spin and orbital magnetic of moment that interactions spin and orbital are consisted of spin-spin, orbital-orbital and spin-orbital. Those coupling have been considered only spin-spin and orbital-orbital coupling. The spin-orbital are ignored due to its too small quantity of magnetic moment when has compared with spin-spin and orbital-orbital coupling. So, the yield of total angular momentum is given by equation 2.40.

$$J = L + S, L + S - 1, \dots, |L - S| \quad (2.40)$$

Where S is resultant yield of spin angular momentum, L is resultant yield of orbital angular momentum and J is spin-orbital summation yield. The Russell-Saunders

coupling has been considered by vector of electrons spin and electrons orbit. So, for example J of C^6 atom can be found J by following equation.

$$S = s_1 + s_2, s_1 + s_2 - 1, \dots, |s_1 - s_2| \quad (2.41)$$

$$L = l_1 + l_2, l_1 + l_2 - 1, \dots, |l_1 - l_2| \quad (2.42)$$

The C^6 electrons orbital have been aligned following $C^6 = 1S^2, 2S^2, 2P^2$. So, the Russell-Saunders coupling for $2P^2$ electrons orbital can be described by following figure 2.20.

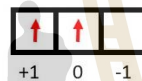


Figure 2.20 Shows $2P^2$ electrons orbital alignment of a C^6 atom.

From figure 2.20, the electrons spin are the same direction as $s_1 = s_2 = \frac{1}{2}$. The electrons orbital are $l_1 = +1$ and $l_2 = 0$. So, the electrons spin summation and electrons orbital summation are calculated by following equation.

$$S_{total} = \sum s = \frac{1}{2} + \frac{1}{2} = 1 \quad (2.43)$$

$$L_{total} = \sum l = 1 + 0 = 1 \quad (2.44)$$

The term of electrons spin summation is $S_{total} = 1$, and term of electrons orbital summation is $L_{total} = 1$. So, the total summation J is consisted of $S_1 = 1, L_2 = 1$, and

$S_1 = 0, L_2 = 1$ cases. The spin and-orbital summation can be calculated by following equation.

$$J_{L,S} = J_{1,1} = 1 + 1, 1 + 1 - 1, 1 - 1 = 2, 1, 0 \quad (2.45)$$

So, the spin and orbital summation of $2P^2$ electrons orbital of C^6 can be replaced by its possible state symbol for 3P_0 , 3P_1 and 3P_2 for $J_{1,1}$, according to Russell-Saunders term symbol. However, the Hund's third rule has indicated the ground state of d^2 configuration coupling that the ground state of under half fill fully electrons orbital is the lowest of J . So the ground state magnetic moment of $2P^2$ electrons orbital of C^6 is 3P_0 .

2.3.6.3 Paramagnetism materials

The paramagnetism materials have occurred because of the materials atoms have small magnetic moments responding when were applied external magnetic field. But, the magnetization and susceptibility are small quantity due to random alignment position of magnetic moment within materials. The susceptibility of paramagnetism materials can be changed with changing environment temperature, according to Curie law. The Curie law equation were found by Pierre Curie, which susceptibility of paramagnetism is inversely proportional with environment temperature. The Curie law equation is shown in equation 2.46.

$$\chi = \frac{C}{T} \quad (2.46)$$

Where C is a Curie constant and T is an environment temperature in kelvin unit.

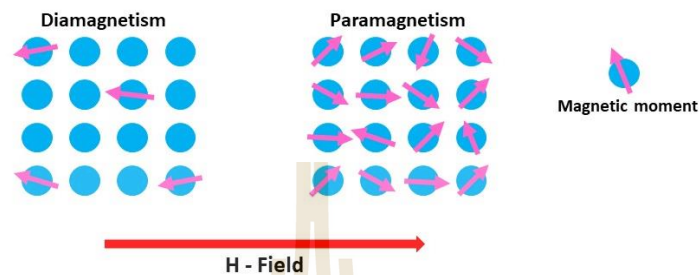


Figure 2.21 Shows magnetic moment responding of diamagnetism and paramagnetism materials with applying external magnetic field.

2.3.6.5 Ferromagnetism materials

The alignment of magnetic moments within ferromagnetism materials is an indicator which led to the description of ferromagnetic behavior. For ferromagnetism materials, the magnetic moments of ferromagnetism have been aligned in the same direction. So, the strong magnetization and high magnetic susceptibility of ferromagnetism materials are expressed. Normally, ferromagnetism materials should be permanent magnet materials. But actually, some ferromagnetism materials do not be permanent magnets. This phenomenon can be explained by magnetic domains. A magnetic domain is defined as a region consisting of many magnetic moment particles. Each magnetic moment particle has a unique magnetization direction. So, that is the reason why some ferromagnetism materials do not be permanent magnets. The magnetization of ferromagnetism materials has been found that its magnetization decreased with increasing environment temperature. The

temperature points which destroyed ferromagnetic magnetization or decreased magnetization to zero is called Curie temperature T_c . The magnetic behavior of

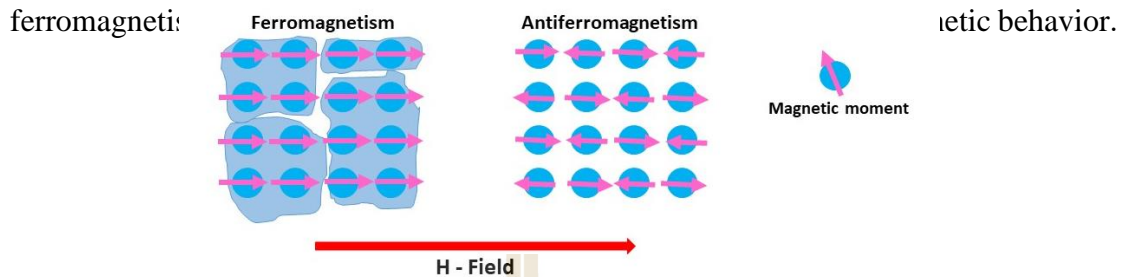


Figure 2.22 Shows magnetic moment responding of ferromagnetism and Antiferromagnetism materials with applying external magnetic field.

2.3.6.6 Antiferromagnetism materials

Antiferromagnetism materials is magnetism materials which consisted of magnetic moment as same as ferromagnetism materials. But, magnetic behavior is the as paramagnetism materials at above critical temperature. However, the magnetic moments direction of antiferromagnetism atoms have been aligned as oppositional direction with neighbor magnetic domains atoms at critical temperature. So, the yield of magnetic moments at the critical temperature are dropped down with applying external magnetic field. The critical temperature point is called neel temperature. The temperature dependence of susceptibility has been explained by Curie-Weiss law. The Curie-Weiss law had been modified to describe antiferromagnetism materials by adding θ to the Curie law equation.

$$\chi = \frac{C}{T - \theta} \quad (2.47)$$

Where θ is a constant unit which depends on antiferromagnetism materials.

At below neel temperature point, the antiferromagnetism materials are described by two magnetic domain field of A and B atoms within materials.

$$H_A = -\mu_{AB}M_B \quad (2.48)$$

$$H_B = -\mu_{AB}M_A \quad (2.49)$$

Where H_A is magnetic field of magnetic domain A which induced magnetization in domain B , H_B is magnetic field of magnetic domain B which induced magnetization in domain A , μ_{AB} is permeability of domain A and B , and M_A, M_B are magnetic moment of domain A and B .

From equations 2.48 and 2.49, the magnetic field of each magnetic domain induced oppositional magnetization of each other domain. At below neel temperature, the moment magnet has destructed each other moment magnet to zero when do not apply external magnetic field that show in equation 2.50.

$$M_{total} = M_A + M_B = M_A + (-M_A) = 0 \quad (2.50)$$

When the external magnetic field H is applied to antiferromagnetism materials at below neel temperature. The magnetization of domain A and B have been considered by 2 events of vertical H_{\perp} and parallel H_{\parallel} external magnetic field. For the vertical case, the H_A and H_B are bended to destruct external magnetic field, but the magnetization M_A, M_B are induced to the same direction of external magnetic field. However, the quantity of M_A, M_B are dependent of angle of the magnetic field of

domain bending. The yield of magnetic field within antiferromagnetism materials is expressed by following equation 2.51-2.55 and figure 2.21.

$$|H_A| \sin \alpha + |H_B| \sin \alpha = H \quad (2.51)$$

$$|H_A| \sin \alpha = |H_B| \sin \alpha \quad (2.52)$$

$$2|H_A| \sin \alpha = H \quad (2.53)$$

$$2\mu_{AB} M_A \sin \alpha = H \quad (2.54)$$

$$M_{total} = 2\mu_{AB} M_A \sin \alpha \quad (2.55)$$

Where α is a bending angle magnetic field of magnetic domain from its original axis.

So, the magnetization of antiferromagnetic with vertical external field are union and increment tend. This effect also led to slightly increases susceptibility of antiferromagnetism at below neel temperature.

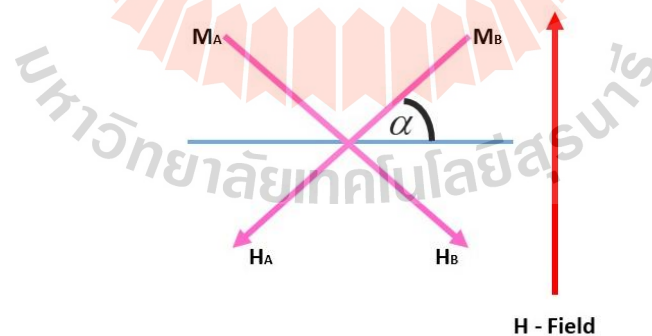


Figure 2.23 Shows effect of applying vertical external magnetic field to antiferromagnetism at below neel temperature.

For applying parallel external magnetic field, the total magnetization of antiferromagnetism are decreased because of effect of magnetic induction with

applying parallel external magnetic field. In event, the direction of external magnetic field have the same direction as magnetization M_A . The magnetization M_A is increased to $M_A + \Delta M_A$. On the other hand, the magnetization M_B which is an oppositional direction have been decreased to $M_B - \Delta M_B$. So, the total magnetization is defined by following equation.

$$M_{total} = (M_A + \Delta M_A) - (M_B - \Delta M_B) = \Delta M_A + \Delta M_B \quad (2.56)$$

$$M_{total} = \Delta M_A + \Delta M_B \quad (2.57)$$

From the equation 2.55 and equation 2.57, the total magnetization of antiferromagnetism materials which applying parallel external magnetic field are less than applying vertical external magnetic field. For the powder antiferromagnetism materials, the direction of parallel and vertical external magnetic field do not effect to magnetization yield because of its magnetic moments are arranged random address. So, the total powder materials magnetization is consisted of vertical and parallel cases with applying external magnetic field. The total magnetization of powder antiferromagnetism materials M_p are considered by following equation 2.54 and equation 2.57.

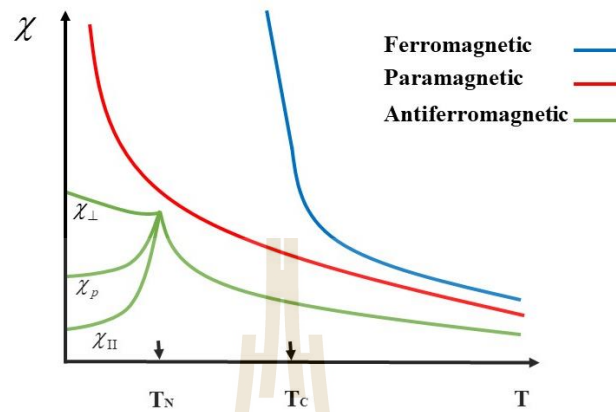


Figure 2.24 Shows ideal temperature dependence of magnetic susceptibility of paramagnetic, ferromagnetic and antiferromagnetic.

2.3.7 Magnetism of 3d transition metal oxide

The 3d transition metals oxide are popular materials which were studied about magnetic properties because of its special electrons orbital conducive to express magnetic behavior interaction such as exchange force, super exchange, double exchange, magnetic order, band theory (Seria Fizica, 2009). In this research, the essential valence electron orbital interactions of 3d transition metals oxide are focused to super exchange and double exchange interactions. The super exchange interaction is a pair atoms of valence electrons alignment on the 3d transition metals oxide which the 3d transition pair atoms have been consisted of half-filled 3d orbital atom A and each other half filled 3d transition orbital atom B. The intermediary between both atoms is an oxygen atom which can be represented by A-O-B. So, the both half-filled 3d orbitals

are forced to spin up for atom A and spin down for atom B because of electrons bounding with oxygen atom. Those spin orbital direction lead to destruction of magnetization between magnetic moment of atom A and magnetic moment of atom B. Usually, the super exchange interaction occurs within antiferromagnetism materials. However, the super exchange interaction does not always occur with 3d transition metals oxide, which are half-filled 3d orbital such as EuS , ZnCr_2Se_4 .

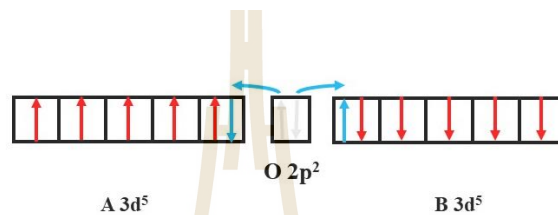


Figure 2.25 Shows super exchange interaction of 3d⁵ orbitals of a pair transition metal oxide atoms.

Double exchange interaction is an interaction which looked like the super exchange interaction. A little different things of double exchange interaction and super exchange interaction are same transition element of paired atoms and difference of oxidation state equal 1 such as $\text{Fe}^{2+} - \text{O} - \text{Fe}^{3+}$, $\text{Mn}^{3+} - \text{O} - \text{Mn}^{4+}$, $\text{Cu}^{2+} - \text{O} - \text{Cu}^{3+}$. The interaction between different oxidation pair atoms have been conducive to electrons coupling bonding of an oxygen and metal pair atoms. The electron coupling can force spinning direction of the bounded-orbitals. The spinning direction yield of electrons orbital pair atoms are the same direction because of forced-bounding orbitals under double exchange interaction of an oxygen and metal transition pair atoms that shows in figure 2.26. So, double exchange interaction leads to strong magnetization yield within magnetism materials.

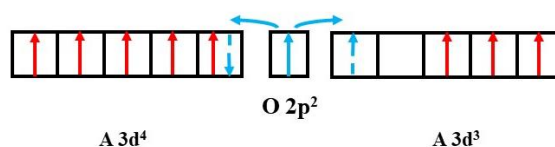


Figure 2.26 Shows double exchange interaction of $3d^3$ and $3d^4$ electron orbital of a pair transition metal oxide atoms.

2.3.7 Magnetic Units

Another essential thing for description magnetism materials are magnetic units of magnetic parameter. In this research, the units are based on Gaussian and cgs/emu units. So, those magnetic parameter units are shown in table 2.4.

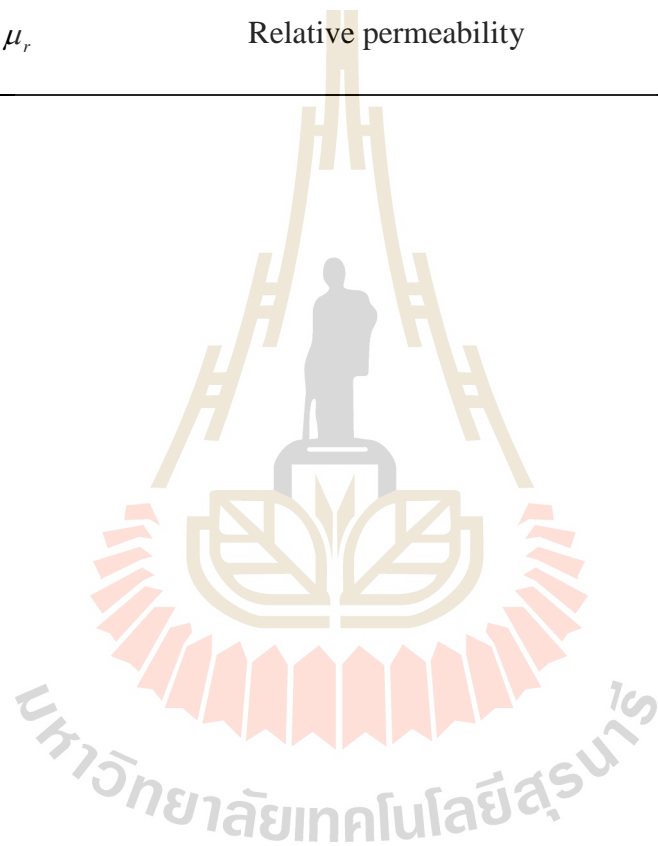
Table 2.4 Magnetic parameters units (Goldberg *et al.*, 1991).

Symbol	Quantity	Gaussian & cgs emu
B	Magnetic induction	Gauss (G)
Φ	Magnetic flux	G.cm ²
H	Magnetic field	Oersted (Oe)
M	Magnetization	emu/cm ³
m	Magnetic moment	emu
χ	Magnetic susceptibility	dimensionless

μ	Permeability	dimensionless
-------	--------------	---------------

Table 2.4 Magnetic parameters units (Goldberg *et al.*, 1991) (Continued).

Symbol	Quantity	Gaussian & cgs emu
μ_r	Relative permeability	dimensionless



CHAPTER III

EXPERIMENTAL PROCEDURE

The chapter III consists of experimental procedures of this research. The outlines of procedures are listed by following sections.

3.1 Fabrication of Cu doped BiFeO₃ thin films

3.1.1 Precursor preparation

The precursor BiFe_{1-x}Cu_xO₃ thin films as $x = 0.0, 0.01, 0.02, 0.03, 0.05, 0.1, 0.2$ and 0.3 were prepared by using sol-gel method. But, only condensation sol process of the sol-gel method was used to prepare the precursor. Initially, the method was started by calculation mass of materials element on suitable ratio and concentration of Bi, Fe and Cu elements. In this research, the optimal proportional of Bi and Fe_{1-x}Cu_x elements is 1.05:1.00, at concentration 0.0625 molar. Then, the mixed precursor solution of bismuth (III) acetate (Bi(CH₃CO₂)₃), iron(II) acetate (Fe(C₂H₃O₂)₂) and copper (II) acetate (Cu(CO₂CH₃)₂) from Sigma-Aldrich as purity 99.99%, were dissolved by the selected solvents of acetone, acetic acid, acetylacetone, deionized water and ethylene glycol (Qi *et al.*, 2006). Then, 20 ml of deionized water, 20 ml of ethylene glycol, 10 ml of acetone, 10 ml of acetylacetone, and 5 ml of acetic acid were stirred by a magnetic stirrer machine. The precursor had been stirred at 80 °C for 30 hours, and 120 °C until

the precursor solution reached to condensation state. For this research, the sufficient concentration of the precursor solution after heating are 0.125 molar because of the precursor stickiness is optimal for spin coating on Pt/Si n-type substrates.

Table 3.1 list of materials and solvent for fabrication Cu doped $\text{BiFe}_{1-x}\text{Cu}_x\text{O}_3$ thin films.

Materials/Solvents	Source	Purity
Bismuth(III)acetate	Sigma-Aldrich	99.99%
Iron(II)acetate	Sigma-Aldrich	99.99%
Copper(II)acetate	Sigma-Aldrich	99.99%
Ethylene glycol	SIAL	99.98%
Acetone	Sigma-Aldrich	99.99%
Acetylacetone	SIAL	99.5%
Acetic acid	Sigma-Aldrich	100%

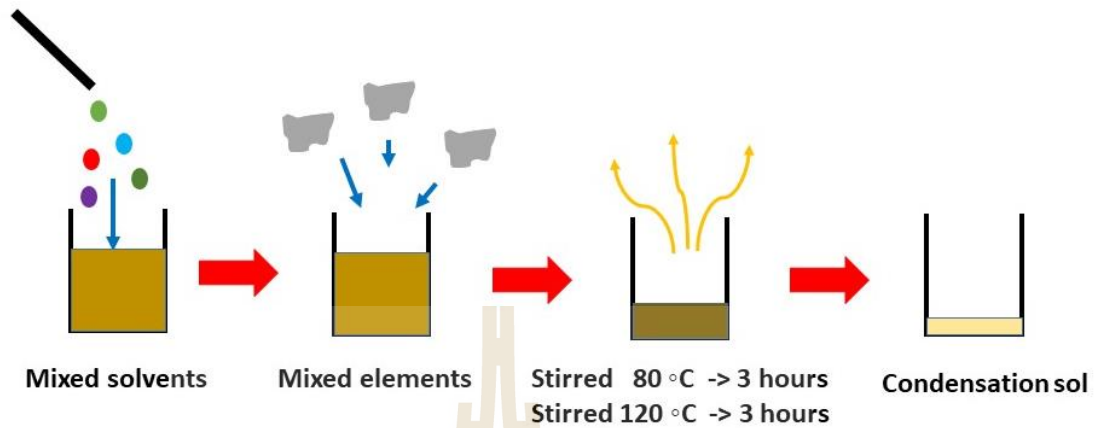


Figure 3.1 Shows illustration of $\text{BiFe}_{1-x}\text{Cu}_x\text{O}_3$ thin films precursor preparation of condensation sol process.

3.1.2 Substrate preparation

The Pt/Si-n type substrates were selected to deposition $\text{BiFe}_{1-x}\text{Cu}_x\text{O}_3$ thin films because of high temperature resistance and undisturbance for materials purity. In the first, the substrates had been started from $\text{SiO}_2/\text{Si-n}$ type. Then, the $\text{SiO}_2/\text{Si-n}$ type plates were cut for 5x4 mm, and removed SiO_2 surface by hydrofluoric acid. The SiO_2 surface had been polished by infusing the SiO_2/Si substrates to hydrofluoric acid for 10 minutes. Then, the Si-n type substrates were washed by Di-water and drying at 100 °C for 30 minutes. Then the Si-n type substrates had been coated Pt films by DC sputtering, and were annealed at 800 °C for 3 hours. The annealing method was done to enhancement high stickiness of PT/Si films layers interfaces.

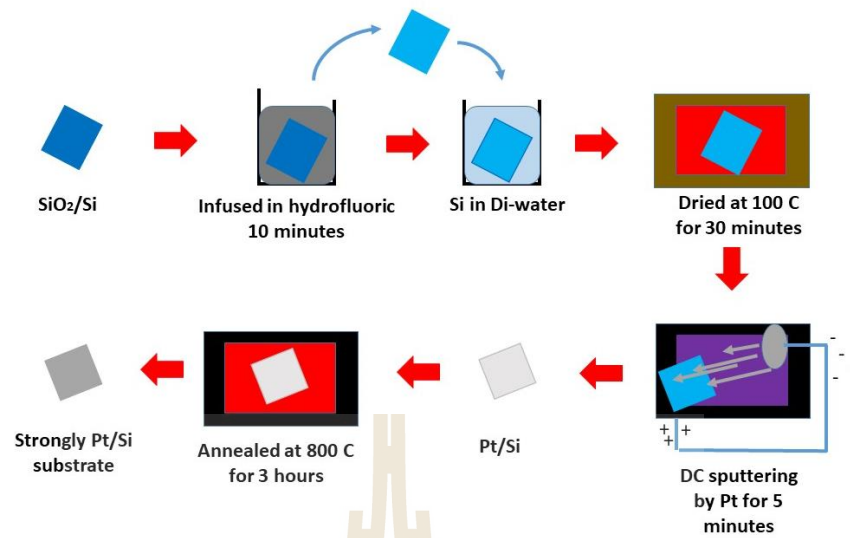


Figure 3.2 Shows illustration of Pt/Si substrates preparation.



Figure 3.3 Shows DC plasma sputtering machine, SUT.

3.1.3 Spin coating and annealing of Cu doped BiFeO₃ thin films

For spin coating method, the precursor had been deposited on Pt/Si-n type substrates by dropping from micro-pipette device. Then, the precursors were spread by spin coating machine at spin rate 1000 rpm for 1 minute, and 4000 rpm for 1 minute. Next, the coated substrates were dried at 100 °C for 2 minute. Those methods were done again until the samples had sufficient film thickness. For this research, the samples had been done for 15 times per sample. Then, the coated substrates were annealed at 600 °C for 6 hours with increasing temperature 1 °C/min. Finally, the samples were cooled down to room temperature.

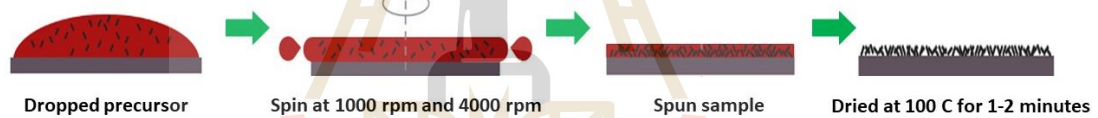


Figure 3.4 Shows spin coating methods to fabricate pre-annealing samples.



Figure 3.5 Shows spin coating machine, VTC-100, SUT.

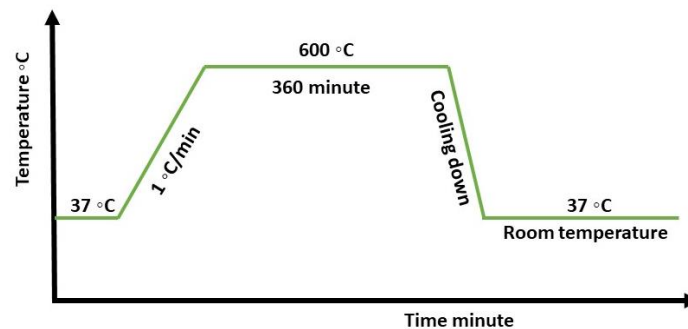


Figure 3.6 Shows scheme of annealing Cu-doped BiFeO₃ thin films.

3.2 Materials characterization

In this work, the sample of Cu-doped BiFeO₃ had been studied crystallite structure and crystallite size, local oxidation structure component elements, and binding energy component of materials element. The technical characterizations details and methods are listed by following sub-topics.

3.2.1 X-ray diffraction

The crystallite structure of Cu-doped BiFeO₃ thin films had been investigated by X-ray diffraction technique. This technique was used to indicate crystallite structure pattern of bismuth ferrite. The pattern of x-ray diffraction spectroscopy was compared with standard x-ray pattern structure of bismuth ferrite. However, the x-ray diffraction of the thin films samples was consisted by another x-ray patterns. So, the x-ray diffraction standard has to have a huge data base for investigation, and comparison those x-ray diffraction patterns. The importance theory of x-ray diffraction is Bragg's law scattering. Bragg's law had described interference of x-ray diffraction that the reflected beam had been constructed and destructed with each other beam. However,

the construction and destruction are depended on its diffraction angles. Those interferences are explained by following equation.

$$2d \sin \theta = n\lambda \quad (3.1)$$

Where d is space between crystallite plan, θ is an angle of x-ray incident beam, λ is x-ray wavelength, which the wavelength is 0.15406 nm, and n is number of x-rays beam interference as destruction and construction.

The x-rays diffraction pattern intensity and its pattern width were used to calculate crystallite sizes of the thin films samples. The crystallite sizes had been calculated by using Debye-Scherrer equation that shows in equations 3.2 (Patterson, 1939).

$$D = \frac{k\lambda}{\beta \cos \theta} \quad (3.2)$$

Where D is a crystallite size, k is a spherical factor, which the factor is $k \approx 0.9$, and β is a full width half maximum (FWHM) intensity of x-ray diffraction peak.

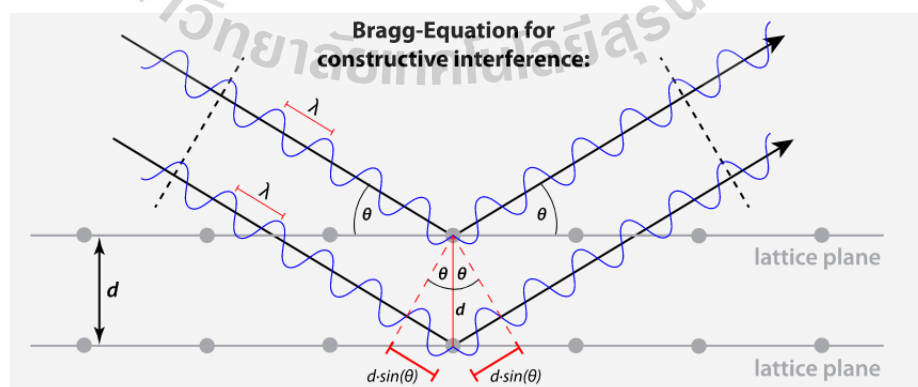


Figure 3.7 Shows x-ray incident and diffraction, according to Bragg's law (www.didaktik.physik.uni-muenchen.de/elektronenbahnen/en/index.php).



Figure 3.8 Shows X-ray diffraction machine, D8-Bruker, SUT.

3.2.2 Scanning electron microscopy

The scanning electron microscopy (SEM) is a scientist equipment which has been used to reveal morphology of object with high multiplier resolution for $1x - 100000x$ of original object. The scanning electron microscopy had been operated by electron scattering reflection detector. So, the sample of object need to dry out water molecules, and coat with gold element. The SEM equipment can be used to indicate materials components by using EDS technique. For this research, the SEM technique was used to image surface morphology and thickness of the thin films. The measurement technique for films thickness called SEM cross section. The SEM cross section technique is the same as normal SEM, but the sample holder is different. The cross section holder had been used to set vertical with the sample plane before the films thickness were imaged. The scanning electron microscopy is shown in figure 3.9.



Figure 3.9 Shows scanning electron microscopy, FE-SEM, SUT.

3.2.3 X-ray absorption spectroscopy

The x-ray absorption spectroscopy (XAS) is a technique which is used to study materials elements structure by using absorption spectra of x-ray beam. The transmission and reflection intensity of x-ray incident beam are used to indicate oxidation state of local elements inside materials sample. Due to, each electron orbital of materials elements can absorb unique x-ray frequencies. So, the x-ray absorption spectra of those element's electron orbitals are used to describe materials structure. For the thin films samples, the x-ray absorption is set by reflection mode because of high intensity x-ray in transmission mode. The equation for measurement x-ray absorption spectra are shown in equation 3.3.

$$\mu_E \propto \frac{I_f}{I_0} \quad (3.3)$$

Where μ_E is coefficient of reflection intensity, I_f is x-ray reflection intensity and I_0 is x-ray incident intensity.

The coefficient and energy of I_0 . Has been plotted in term of μ_E versus E . When E is energy of incident x-ray. The measurement technique scheme is shown in figure 3.10.

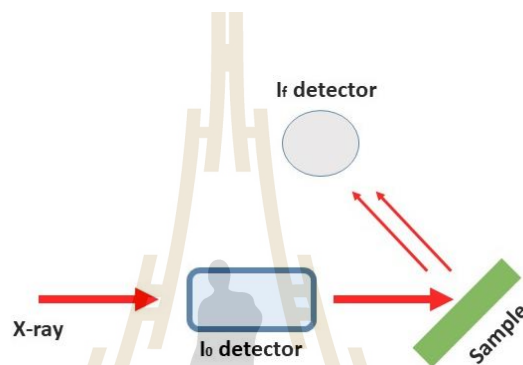


Figure 3.10 Shows measurement scheme of x-ray absorption reflection mode.

3.2.4 X-ray photoelectron spectroscopy

The x-ray photoelectron (XPS) are used to measure electrons binding energy of materials surface elements, according to phenomenon photoelectron emission. This technique uses x-ray beam ejection to materials samples surface. The emission electrons of the materials samples surface are measured kinetic energy by spherical electric field measurement probe. The data analysis consists of x-ray energy ejection and electrons emission quantity. The electrons emission quantity reveals the binding energy of each electrons orbital which are leaded to oxidation states of the electron orbital. The equipment scheme is shown in figure 3.11.

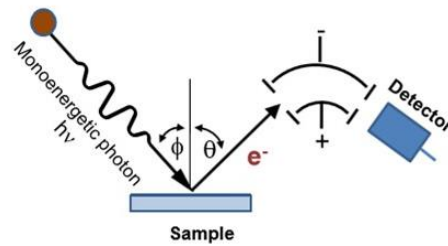


Figure 3.11 Shows equipment scheme of x-ray photoelectron spectroscopy (Applied from Narong Chanlek, 2016).

3.2 Electrical and magnetic properties

3.2.1 Electrical properties

The Cu-doped BiFeO₃ thin films had been studied electrical properties by using Agilent 4294A precision impedance analyzer for measurement ϵ_r , $\tan \delta$ and Z complex impedance. The Z complex impedance spectra are used to indicated grain conductance σ_g and grain boundary conductance σ_{gb} . The conductance is an opposite parameter of resistance. So, the σ_g and σ_{gb} can be calculated by following equation.

$$\sigma_g = \frac{1}{R_g} \quad (3.4)$$

$$\sigma_{gb} = \frac{1}{R_{gb}} \quad (3.5)$$

Where R_g and R_{gb} are defined by equation 2.18. The high conductance parameter indicates to high quantity of electrical properties of materials. But, the loss tangent $\tan \delta$ is used to indicate defective electrical properties of materials. The Agilent 4294A precision impedance analyzer is shown at figure 3.11.



Figure 3.12 Shows Agilent 4294A precision impedance analyser, KKKU.

3.2.2 Magnetic properties

The magnetic properties of Cu-doped BiFeO₃ thin films had been revealed by vibrating sample magnetometer (VSM). This machine is used to measure magnetization of sample, which were applied external magnetic field. The external magnetic field are applied through the sample for induce the magnetization of sample. The magnetization is used to describe magnetism and magnetic behavior of the materials samples by magnetic analysis methods such as susceptibility, temperature

dependence, ZFC – FCC, ZFC-FCW, $\frac{M_r}{M_s}$ versus $\frac{B_{cr}}{B_c}$. Those parameters explain to

magnetic behavior that are shown in equation 2.18-2.57. The vibrating sample magnetometer is shown in figure 3.13.



Figure 3.13 Shows vibrating sample magnetometer, Versalab, KKU.



CHAPTER IV

RESULTS AND DISCUSSION

Chapter IV is consisted of whole experimental results as characterization part and properties part of $\text{BiFe}_{1-x}\text{Cu}_x\text{O}_3$ thin films at $x = 0.01, 0.02, 0.03, 0.05, 0.1, 0.2$ and 0.3 . The experiment results have been proposed by science hypothesis method and specific theory of each result part. The results and discussion are divided to five section of x-ray diffraction results, scanning electron microscope results, x-ray absorption results, x-ray photo electron results, magnetic properties and electric properties, respectively.

4.1 X-ray diffraction

The x-ray diffraction patterns had been used to investigate $\text{BiFe}_{1-x}\text{Cu}_x\text{O}_3$ thin films structure by theorem of Bragg's law. In the first, this work was looking for an optimal synthesis method to fabricate $\text{BiFe}_{1-x}\text{Cu}_x\text{O}_3$ thin films. So, the initial synthesis had been focused on synthesis pure BiFeO_3 thin films. Due to the many literature reviews had reported that fabrication BiFeO_3 thin films were mostly synthesized by sol-gel method. So, the research started from sol-gel method by using nitrate route of ethylene glycol and metals element of bismuth nitrate and iron nitrate (Khajonrit *et al.*, 2018). Then, acetate route of deionized water, acetone, acetic acid of Bi acetate and Fe acetate (Qi *et al.*, 2006) were synthesized for comparison with nitrate route. Initially, the researcher had used grazing incident x-ray diffraction mode because trying to reduce x-ray diffraction background of the Pt/Si substrates (Lee and Wu, 2007). Then, the researcher

had been advised to use normal incident x-ray diffraction mode because of low resolution of the grazing incident x-ray diffraction mode. So, the x-ray diffraction results are consisted of both x-ray diffraction grazing incident and normal incident x-ray diffraction mode. The x-ray patterns of BiFeO_3 thin films were compared with standard ICSD #15299 (Moreau *et al.*, 1971), Si (Kasper and Richards, 1964), Pt (Bredig and Allolio, 1927), PtO (Kumar and Saxena, 1989), PtO_2 (Muller and Roy, 1968), $\text{Bi}_2\text{Fe}_4\text{O}_9$ (Tutov and Markin, 1970), $\text{Bi}_{25}\text{FeO}_{40}$ (RANGAVITTAL *et al.*). The first x-ray diffraction results of acetate route and nitrate route are shown in figure 4.1. Both of the solutions had been prepared and annealed at 600°C for 6 hours.

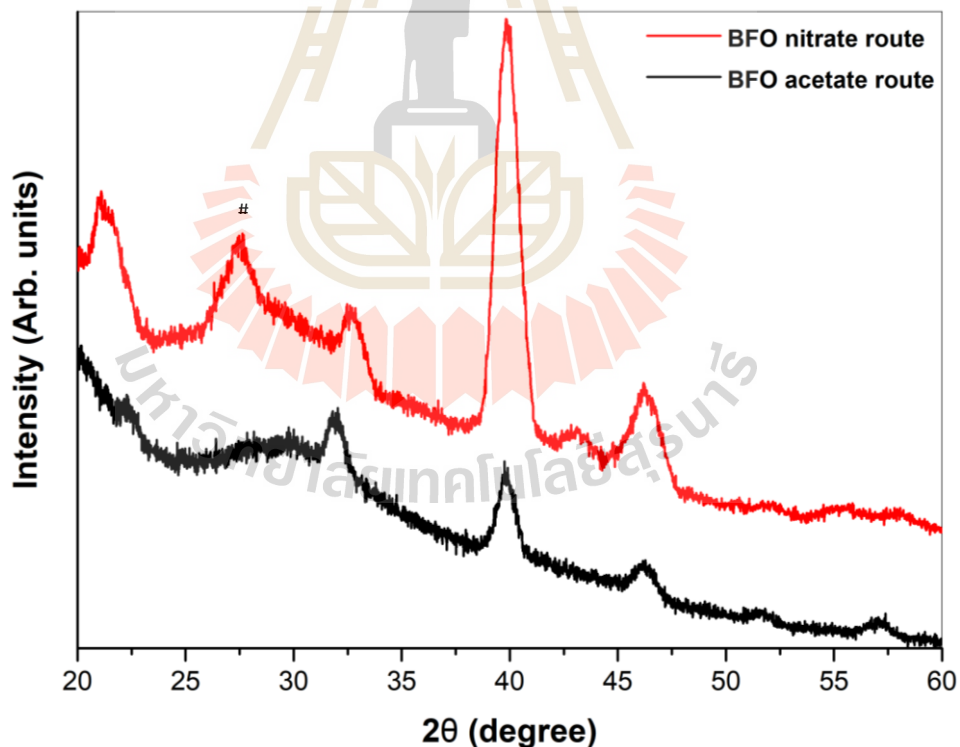


Figure 4.1 Shows grazing incident x-ray diffraction pattern of BiFeO_3 nitrate route and BiFeO_3 acetate route.

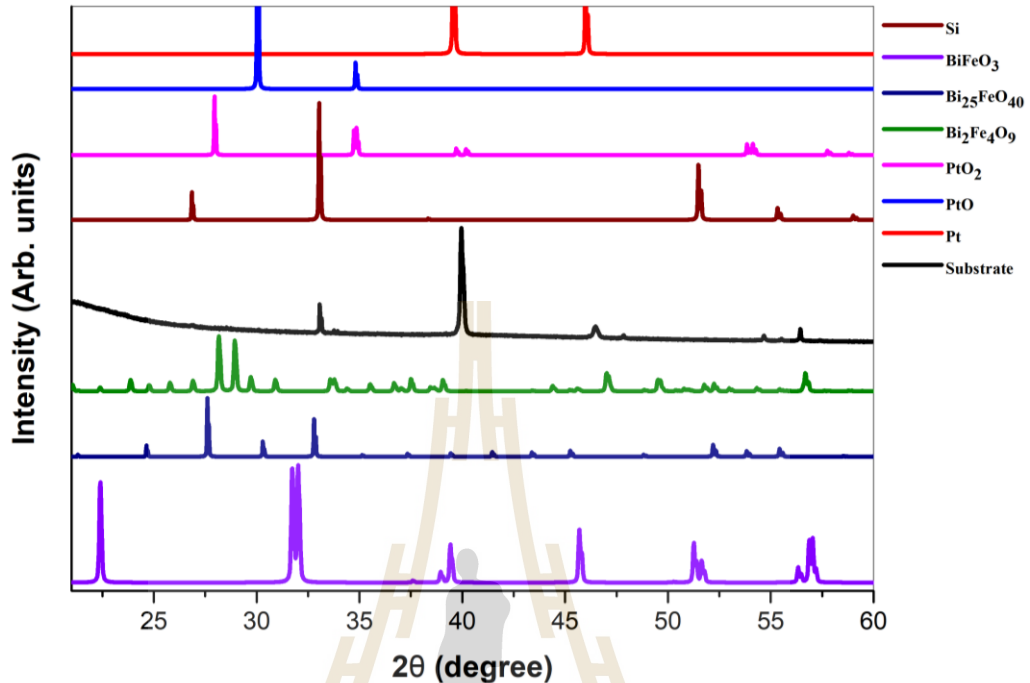


Figure 4.2 Shows x-ray diffraction pattern of substrate, Si, Pt, PtO, PtO₂, Bi₂Fe₄O₉, Bi₂₅FeO₄₀ and BiFeO₃.

The impurity phase of Bi₂Fe₄O₉ had occurred in BiFeO₃ thin films structure, which were prepared by nitrate route at x-ray diffraction angles for $2\theta \approx 27.3$ degree. While the impurity phase did not occur in BiFeO₃ thin films which prepared by acetate route. So, the acetate route has selected to fabricate BiFe_{1-x}Cu_xO₃ thin films. Then, mixture solvents of the acetate route were investigated an optimal proportion of the mixture solvents, and also were compared with another solvent. Next, acetone solvent was investigated by varying quantity of acetone solvent for 0, 2.5, 7.5, 10 and 20 ml into acetate route precursor. The results are shown in figure 4.3.

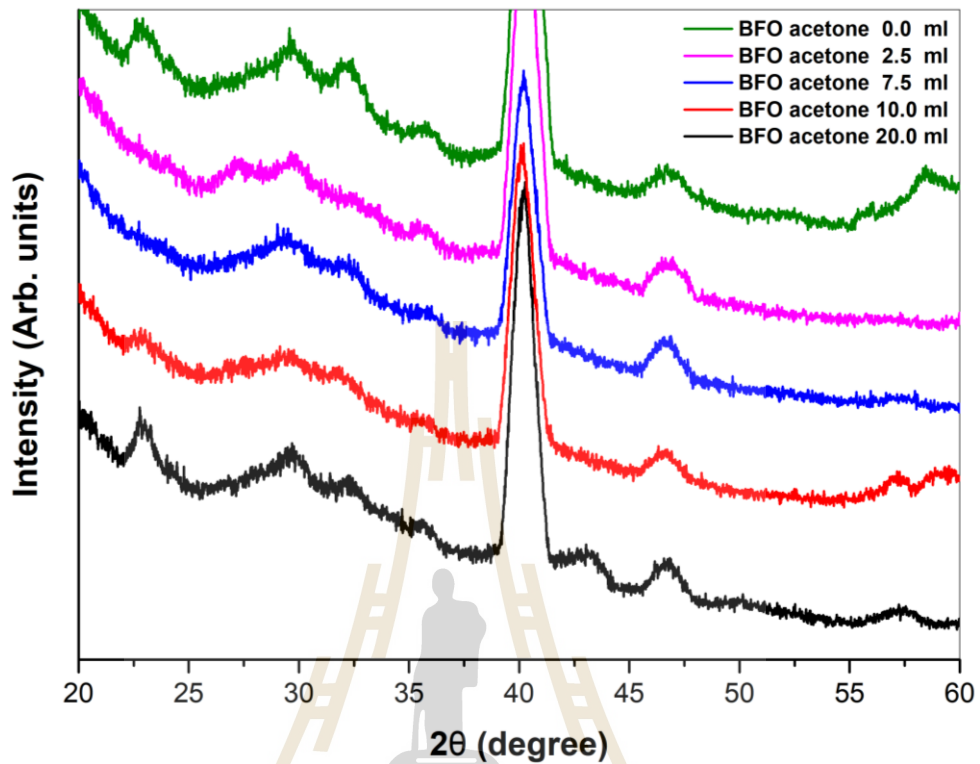


Figure 4.3 Shows grazing incident x-ray diffraction pattern of BiFeO₃ dependence of acetone solvent quantity as 0.0, 2.5, 7.5, 10 and 20 ml.

From the figure 4.3, the optimal quantity of acetone solvent for fabrication BiFeO₃ thin films is 10 ml. Then, acid kinds had been investigated by acetic acid and citric acid. The x-ray diffraction yield of BiFeO₃ thin films which were prepared by acetic acid and citric acid, are shown in figure 4.4.

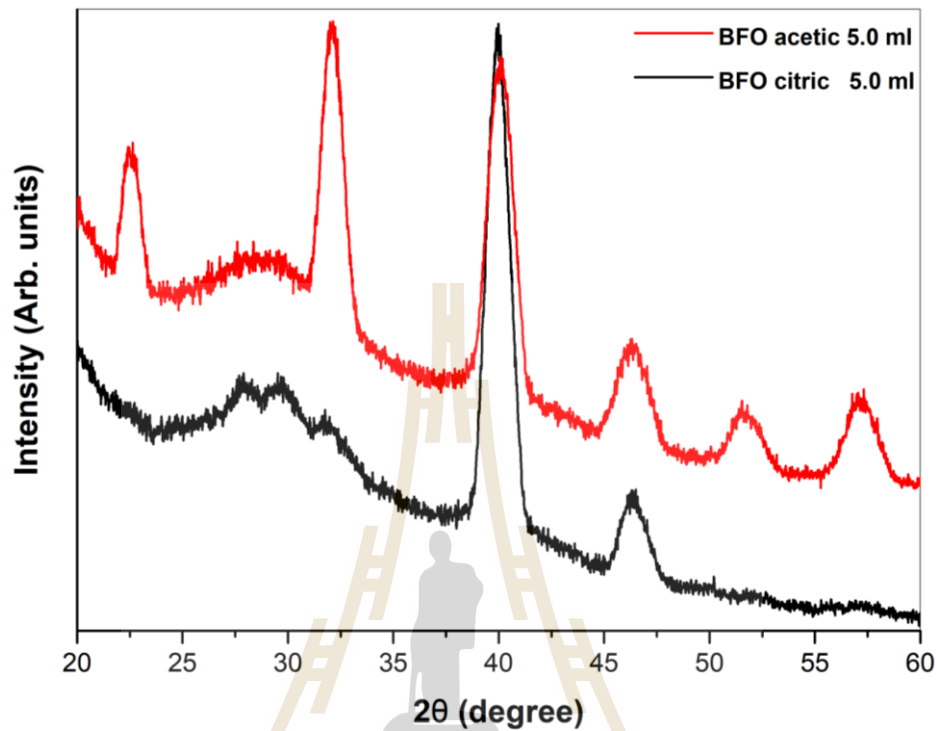


Figure 4.4 Shows grazing incident x-ray diffraction pattern of BiFeO_3 thin films which were prepared by acetic acid and citric acid.

From figure 4.4, the x-ray diffraction pattern of BiFeO_3 thin films which was prepared by citric acid solvent did not occurred purity phase of BiFeO_3 . Due to, the sample restructured phase of $\text{Bi}_2\text{Fe}_4\text{O}_9$ which can be observed by strongly diffraction peak for $2\theta \approx 27\text{-}30$ degree. So, the acetic acid is an optimal solvent for fabrication BiFeO_3 thin films. Then, quantity of acetic acid was investigated by varying quantity of acetic acid solvent as 2.5, 5, 10 and 15 ml. The x-ray diffraction patterns dependence of acetic acid quantity was shows in figure 4.5.

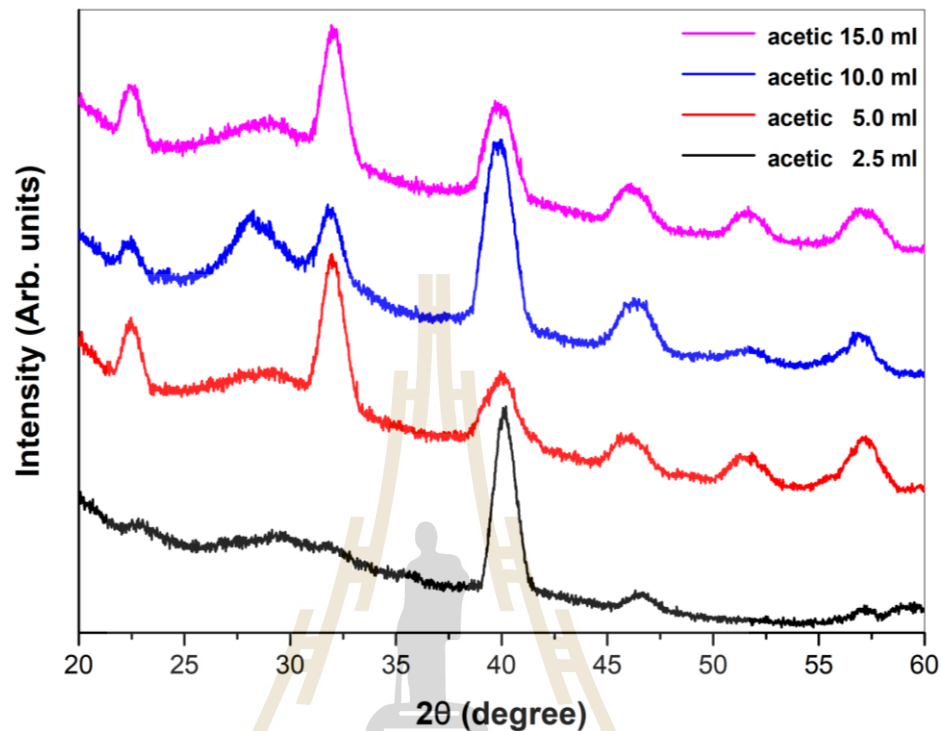


Figure 4.5 Shows grazing incident x-ray diffraction pattern of BiFeO_3 thin films dependent on acetic acid quantity as 2.5, 5, 10 and 15 ml.

From the figure 4.5, the optimal acetic acid quantity for fabricated BiFeO_3 thin films is 5 ml and 15 ml. The acetic acid as 5 ml and 15 ml were considered crystallinity quality of BiFeO_3 thin films. Then, the 5 ml of acetic acid quantity was selected because it had a better x-ray diffraction intensity peaks sharpness for $2\theta \approx 56\text{-}58$ degree. Due to the literature review reported that temperature for forming BiFeO_3 orthorhombic R3c was 600°C (Kumar *et al.*, 2010). Then, the experiment was concerned to find annealing temperatures for forming purity phase structure of BiFeO_3 thin films. So, the selected annealing temperature for comparison results are 600 , 700 and 800°C . The x-ray diffraction pattern dependence of annealing temperature is shown in figure 4.6.

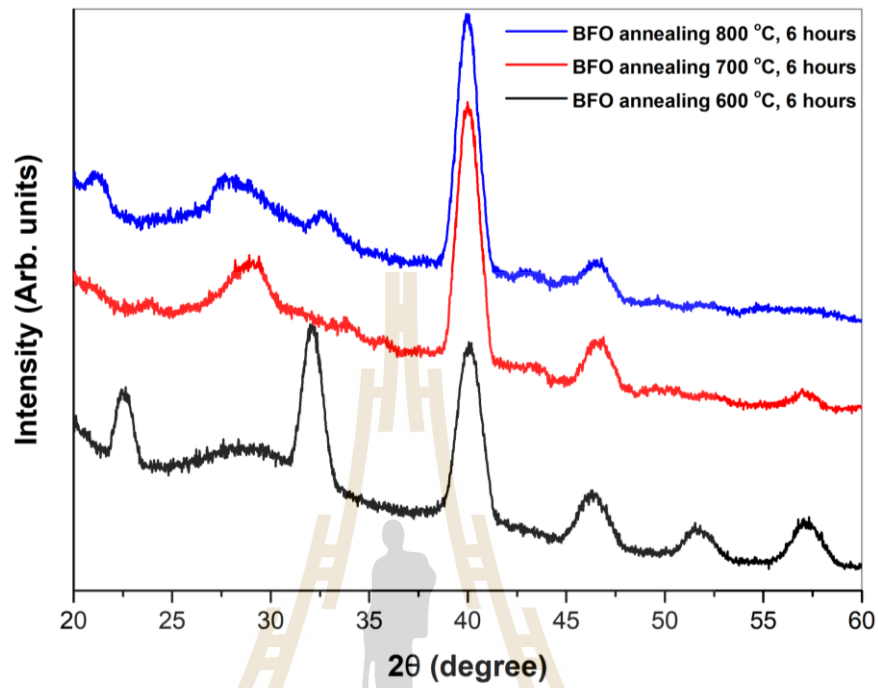


Figure 4.6 Shows grazing incident x-ray diffraction pattern BiFeO₃ thin films dependence of annealing temperature as 600, 700 and 800 °C

From figure 4.6, the purity phase of BiFeO₃ thin films has expressed at annealing temperature as 600 °C while another annealing temperature presented impurity phase of Bi₂Fe₄O₉, according to x-ray diffraction standard patterns peak in figure 4.2. So, the optimal elements sources, solvents proportional, acid kind and annealing temperature for fabrication BiFe_{1-x}Cu_xO₃ thin films have been investigated. However, the x-ray diffraction pattern of BiFeO₃ expressed unknown curve peak at between $2\theta \approx 25-30$ degree. The researcher tried to find a reason and info for describing the unknown curve peak. Presumption of expert materials scientist expert, the unknown curve peak may be peak of XRD holder. For proof the reason, the polyethylene terephthalate XRD holder was done for replacement original XRD holder by following

figure 4.7. The polyethylene terephthalate XRD holder were used to compare x-ray diffraction patterns peak background yield with XRD original holder. The x-ray diffraction patterns peak background of polyethylene terephthalate XRD holder and XRD original holder are shown in figure 4.8 and figure 4.9.

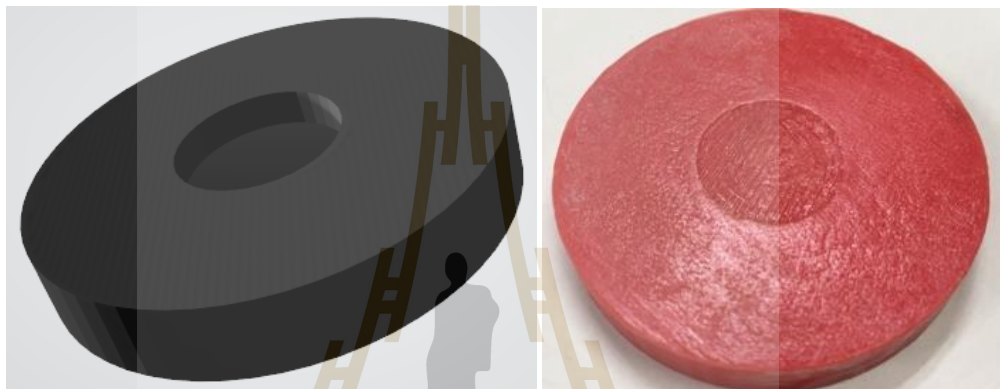


Figure 4.7 Shows polyethylene terephthalate XRD holder from 3D printer.



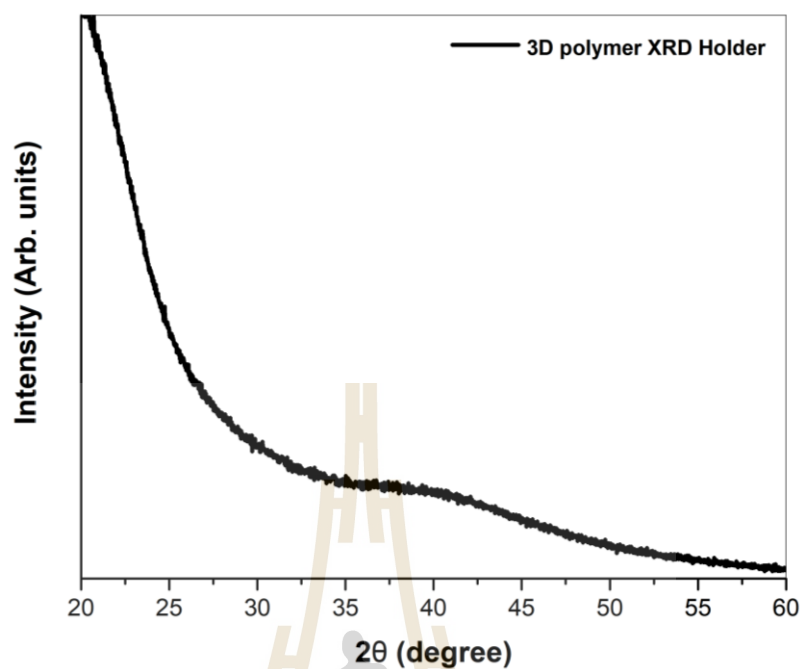


Figure 4.8 Shows grazing incident x-ray diffraction pattern background of polyethylene terephthalate XRD holder.

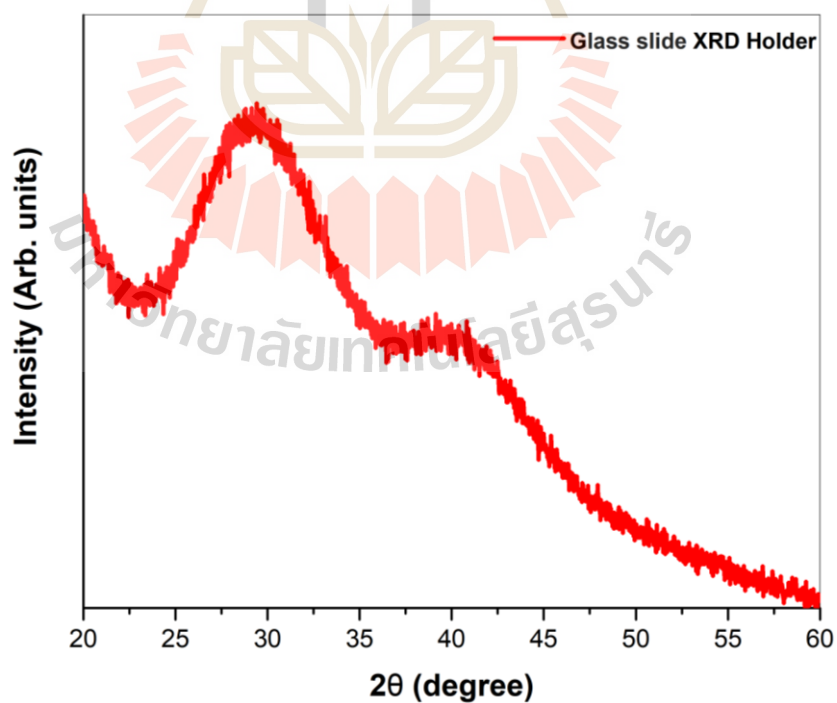


Figure 4.9 Shows grazing incident x-ray diffraction pattern background of Glass slide XRD holder.

From the figure 4.8 and 4.9, it clearly that the unknown peak between $2\theta \approx 25-30$ degree are peak of original XRD holder. Then, the prepared BiFeO_3 thin films had been measured x-ray diffraction pattern on polyethylene terephthalate holder and original XRD holder for comparison the x-ray diffraction pattern yields. The yields of both x-ray diffraction pattern were used to confirm unknown curve peak effect, and were used to check impurity phase of BiFeO_3 thin films.

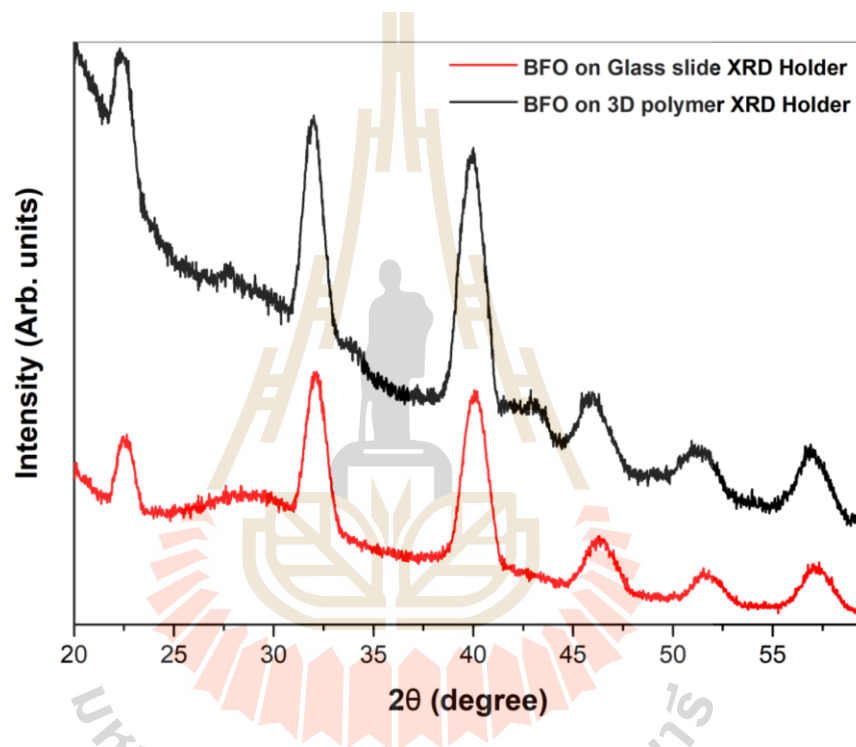


Figure 4.10 Shows grazing incident x-ray diffraction pattern of BiFeO_3 thin films on Glass slide XRD holder and 3D polymer holder.

From figure 4.10, the unknown curve peak has been confirmed. However, the grazing incident mode of x-ray diffraction pattern cannot use to calculate crystallite sizes because of its huge FWHM peak, and some diffraction peak were merged by neighbor peak. So, x-ray diffraction normal beam is used to investigate the x-ray diffraction pattern of BiFeO_3 thin film. The x-ray diffraction pattern yield of BiFeO_3

thin films which have been measured by grazing incident and normal incident x-ray diffraction mode, are shown in figure 4.11.

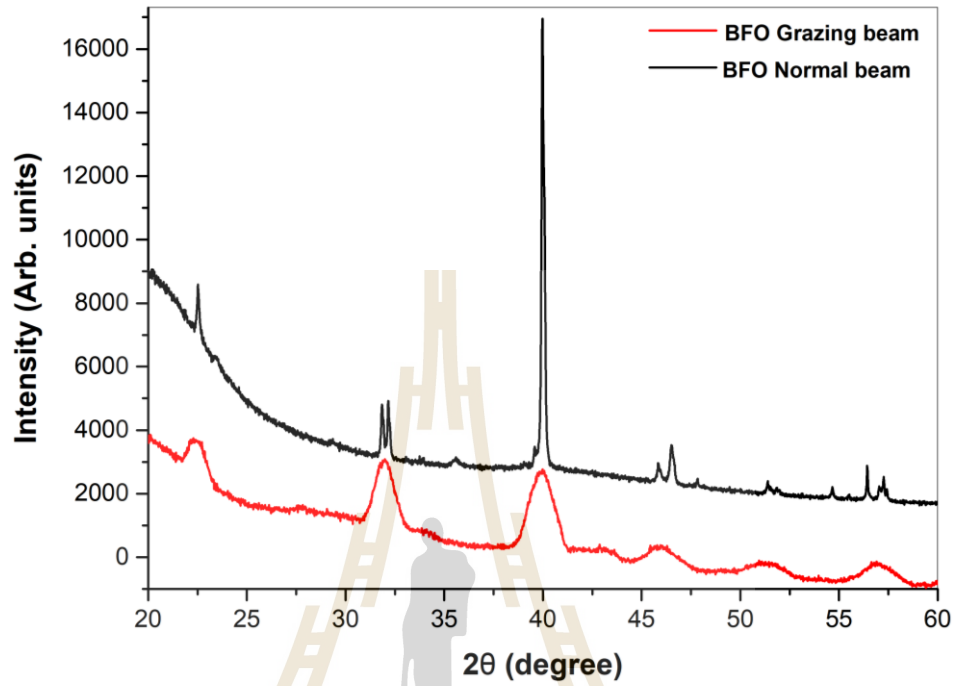


Figure 4.11 Shows x-ray diffraction pattern of BiFeO_3 thin films which were measured by measured grazing incident beam, and normal incident beam.

From figure 4.11, the x-ray normal incident x-ray diffraction pattern of BiFeO_3 thin films reveals some impurity phase of $\text{Bi}_2\text{Fe}_4\text{O}_9$ as ICSD #20067 (Tutov and Markin, 1970) which were hidden by grazing incident x-ray diffraction mode. For higher resolution of x-ray diffraction pattern and convenient for calculation crystallite sizes, the normal incident x-ray diffraction mode has been used to investigate crystallite structure of all $\text{BiFe}_{1-x}\text{Cu}_x\text{O}_3$ thin films samples. The x-ray diffraction pattern of $\text{BiFe}_{1-x}\text{Cu}_x\text{O}_3$ thin films as $x = 0.01, 0.02, 0.03, 0.05, 0.1, 0.2$ and 0.3 which were prepared by modified acetate route at 600°C and annealed for 6 hours, are shown in figure 4.12.

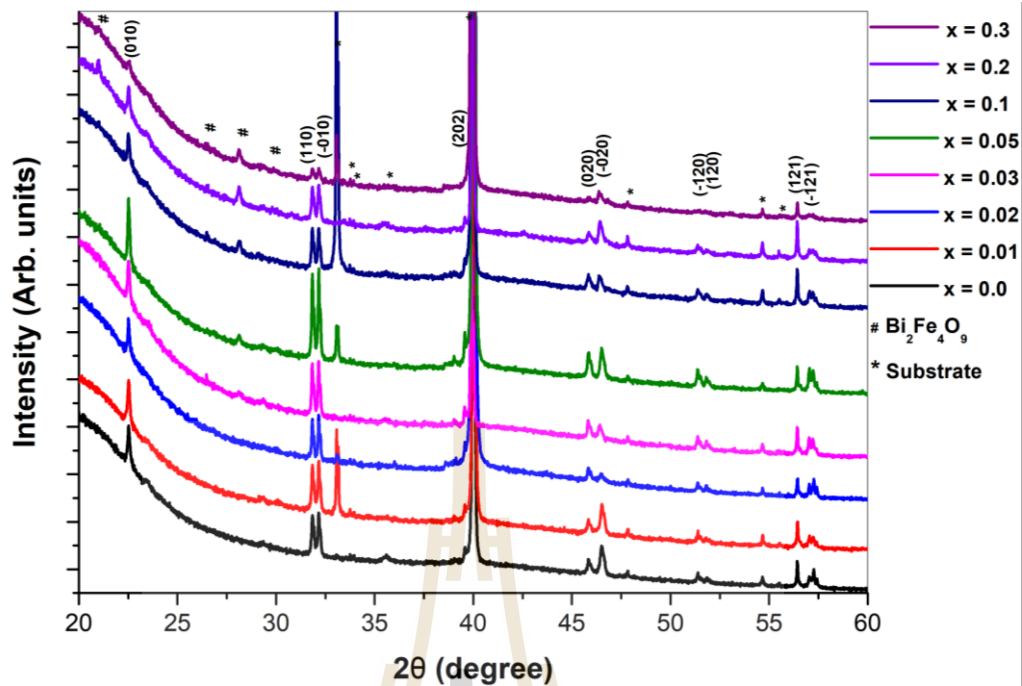


Figure 4.12 Shows normal incident x-ray diffraction pattern of BiFe_{1-x}Cu_xO₃ thin films as x = 0.0, 0.01, 0.02, 0.03, 0.05, 0.1, 0.2 and 0.3.

From figure 4.12, the x-ray diffraction patterns of BiFe_{1-x}Cu_xO₃ thin films as x = 0.0, 0.01, 0.02, 0.03, 0.05, 0.1, 0.2 and 0.3 reveal almost impurity phase of x-ray diffraction pattern of BiFeO₃ orthorhombic R3c structure ICSD #15299 (Moreau *et al.*, 1971). But, some impurity phase of Bi₂Fe₄O₉ ICSD #20067 (Tutov and Markin, 1970) and substrate phase of Si Ia3 0 ICSD #009282 (Kasper and Richards, 1964), PtO₂P3m1 ICSD #1008935 (Muller and Roy, 1968) are also occurred within BiFe_{1-x}Cu_xO₃ thin films structure. The impurity phase intensity of Bi₂Fe₄O₉ increased with increasing Cu-doped on crystallite structure of BiFe_{1-x}Cu_xO₃ thin films. The x-ray diffraction intensity of bismuth ferrite structure increased with increasing Cu doping concentration as x = 0.01-0.05, according to the same result of literature review report (Riaz *et al.*, 2015). The literature review report had expressed that the variant of x-ray diffraction intensity

did not change bismuth ferrite structure (Li *et al.*, 2013). The increasing of x-ray diffraction intensity peaks may because of substitution of Cu doing elements enhanced crystallinity of the bismuth ferrite structure. The peaks shifting of x-rays diffraction peaks are about 0.01 degree due to substitution of smaller Cu element, and consequently peak shift forward (Li *et al.*, 2014; Wu *et al.*, 2015) . The peak shifting of Cu-doped bismuth ferrite thin films are shown in figure 4.13.

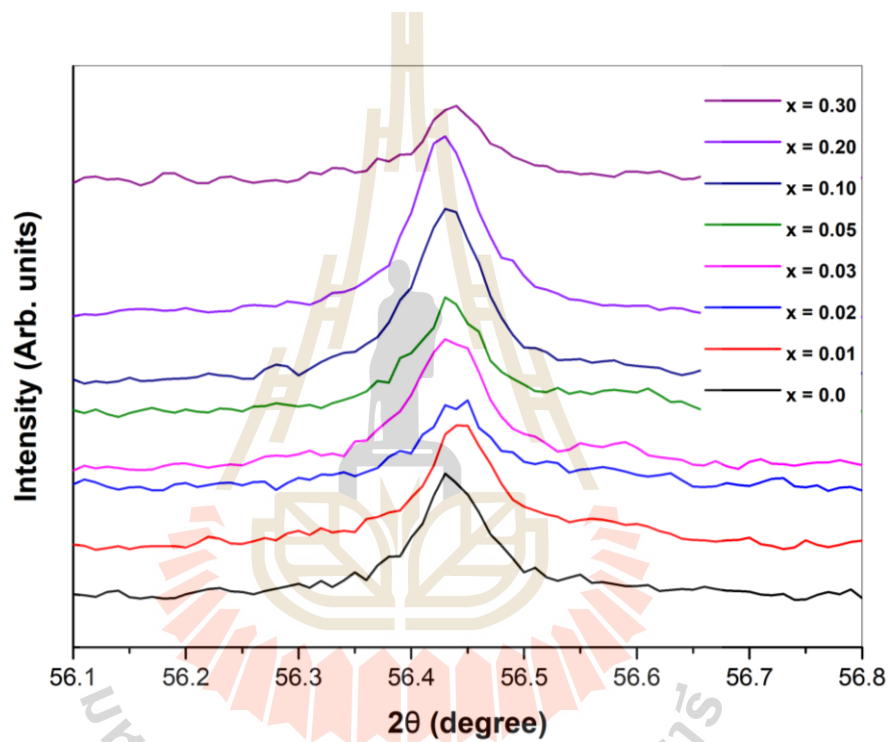


Figure 4.13 Shows peak shifting of BiFe_{1-x}Cu_xO₃ thin films as x = 0.0, 0.01, 0.02, 0.03, 0.05, 0.1, 0.2 and 0.3 at $2\theta \approx 56.42$.

However, the phase shifting of x-rays diffraction peak did not occurred when doped Cu elements as x = 0.2 and 0.3. The x-ray diffraction peak shifting stopped Cu doping as x = 0.2 and 0.3 may because of BiFe_{1-x}Cu_xO₃ thin films were doped Cu elements more than optimal doping concentration. The crystallite sizes effect of Cu-

doped bismuth ferrite thin films which were calculated by Debye-Scherer equation (equation 3.2), are shown in figure 4.14.

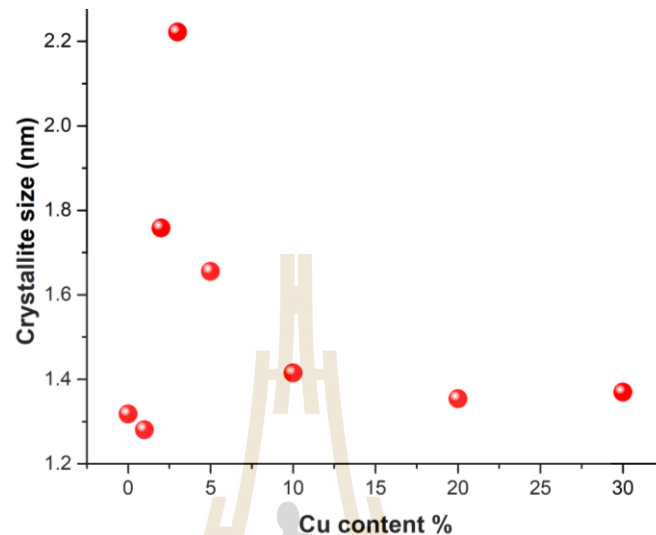


Figure 4.14 Shows crystallite sizes dependence of Cu content %.

The crystallite size of $\text{BiFe}_{1-x}\text{Cu}_x\text{O}_3$ thin films increased with increasing Cu content % as $D = 1.31, 1.28, 1.76$ and 2.22 nm with $x = 0.0, 0.01, 0.02$ and 0.03 . Then, the crystallite size decreased with increasing Cu content % as $D = 1.65, 1.41, 1.35$ and 1.37 nm with $x = 0.05, 0.1, 0.2$ and 0.3 . The decreasing of crystallite sizes at Cu content % as $x = 0.05-0.3$ because of over optimal doping of Cu doping contents (Khajonrit *et al.*, 2016), and consequently incompletely substitution and high impurity intensity phase that can observe in figure 4.12. The increment feature of the crystallite size also occurred with another perovskite structure materials as Dy-doped BiFeO_3 nanoparticles (Priya *et al.*, 2016), Mn-doped LaFeO_3 (Jeong *et al.*, 2018).

4.2 Scanning electron microscopy

The scanning electron microscopy has been used to revealed morphology surface and films thickness of $\text{BiFe}_{1-x}\text{Cu}_x\text{O}_3$ thin films. The samples were prepared by drying sample method and gold coating method. The prepared sample were imaged by SEM machine of SUT equipment facility center service. Initially, the $\text{BiFe}_{1-x}\text{Cu}_x\text{O}_3$ thin films were placed to anneal as 1 hour, 3 hours and 6 hours for finding optimal grain forming time of the thin films. But, 1 hour annealing of BiFeO_3 did not form grain, according to SEM imaged of a literature review (Tang *et al.*, 2014), also the same for 3 hours annealing of Dy-doped bismuth ferrite thin films (Priya *et al.*, 2016). So, the 6 hours for annealing had been selected, according to sintering ceramic materials were initial started at 6 hours (Boonlakhorn *et al.*, 2014).

The SEM imaged and SEM cross section are shown in figure 4.15 and figure 4.16. Those selected images are the best of $\text{BiFe}_{1-x}\text{Cu}_x\text{O}_3$ thin films SEM images as $x = 0.0$ and 0.1 . The figure 4.15 are SEM images of $\text{BiFe}_{1-x}\text{Cu}_x\text{O}_3$ thin films as $x = 0.0$. Those images were multiplied as 3k, 10k, 30k and 50k, respectively. Films surface morphology of the $\text{BiFe}_{1-x}\text{Cu}_x\text{O}_3$ thin films revealed any nonhomogeneous of mountain films, which occurred as the same resulted in literature review report of BiFeO_3 thin films on Ni substrate (Tang *et al.*, 2014). The SEM cross section images of the thin films express films thickness about 200-300 nm that are shows in figure 4.15(e) and 4.15(f). The EDS technique had been requested for identifying the mountain films elements was denied by SEM operator. A reason of denying was occurrence magnetism behavior of $\text{BiFe}_{1-x}\text{Cu}_x\text{O}_3$ thin films while had been measured electron black scattering, and may consequently any destructive SEM detector probe. Form figure 4.16, the SEM images show nonhomogeneous of mountain films over surfaces of $\text{BiFe}_{1-x}\text{Cu}_x\text{O}_3$ thin

films as $x = 0.1$. Due to incompletely sintering grain of $\text{BiFe}_{1-x}\text{Cu}_x\text{O}_3$ thin films, and consequently metals oxide particles split out from the films surface. Increasing of Cu doping contents were effect directly to increase nonhomogeneous films surface which presented at many split out of the metals oxide in figure 4.16. The SEM cross section images of $\text{BiFe}_{1-x}\text{Cu}_x\text{O}_3$ thin films as $x = 0.1$ show films thickness about 200-300 nm. The thickness of $\text{BiFe}_{1-x}\text{Cu}_x\text{O}_3$ thin films as $x = 0.0$ and 0.1 are almost the same thickness for 200-300 nm that are shown in figure 4.15(f) and 4.16(f).



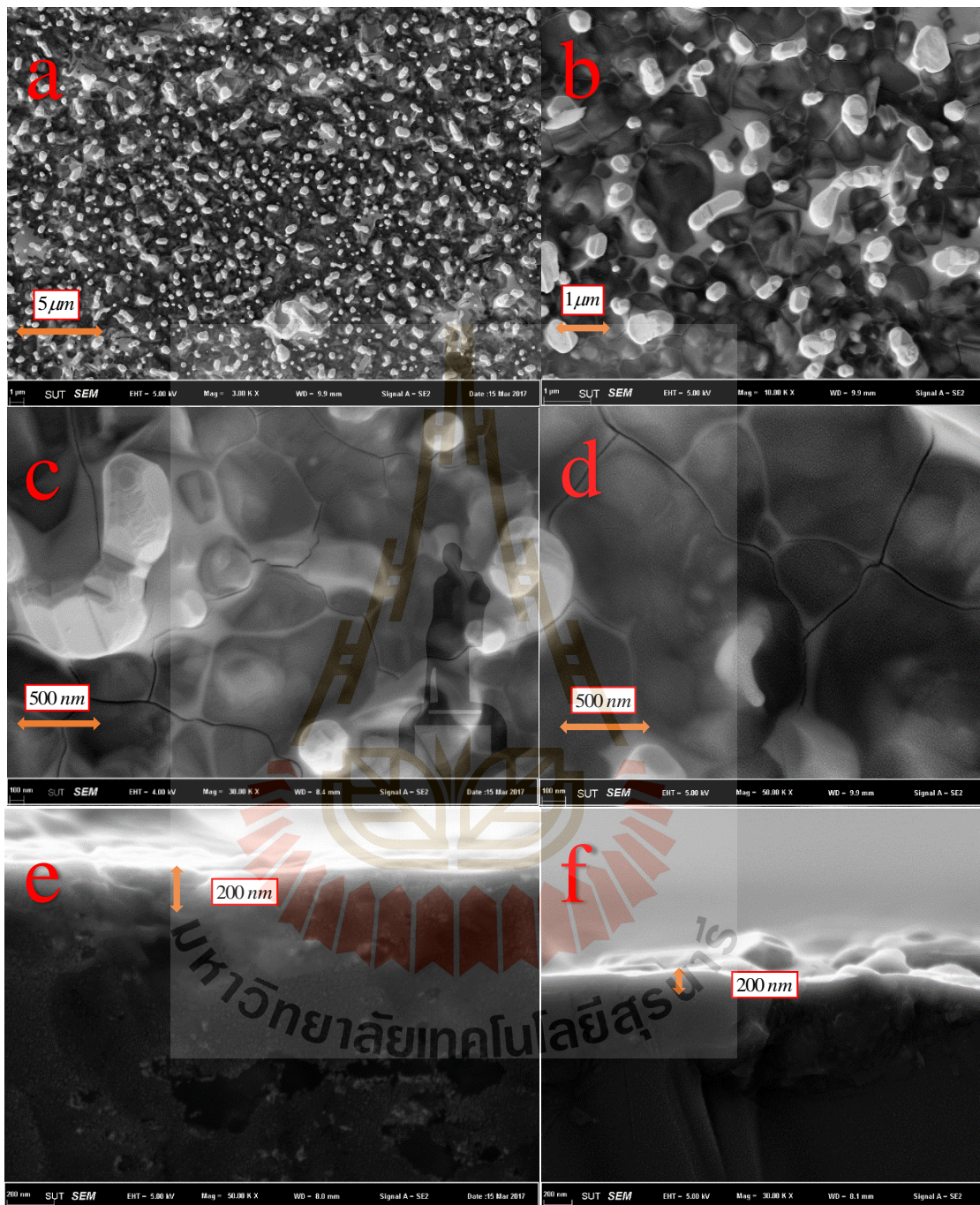


Figure 4.15 Shows SEM and SEM cross section images of $\text{BiFe}_{1-x}\text{Cu}_x\text{O}_3$ thin films as $x = 0.0$ (SEM images as, a at 3k, b at 10k, c at 30k and d at 50k, and SEM cross section images as, 50k of e, f)

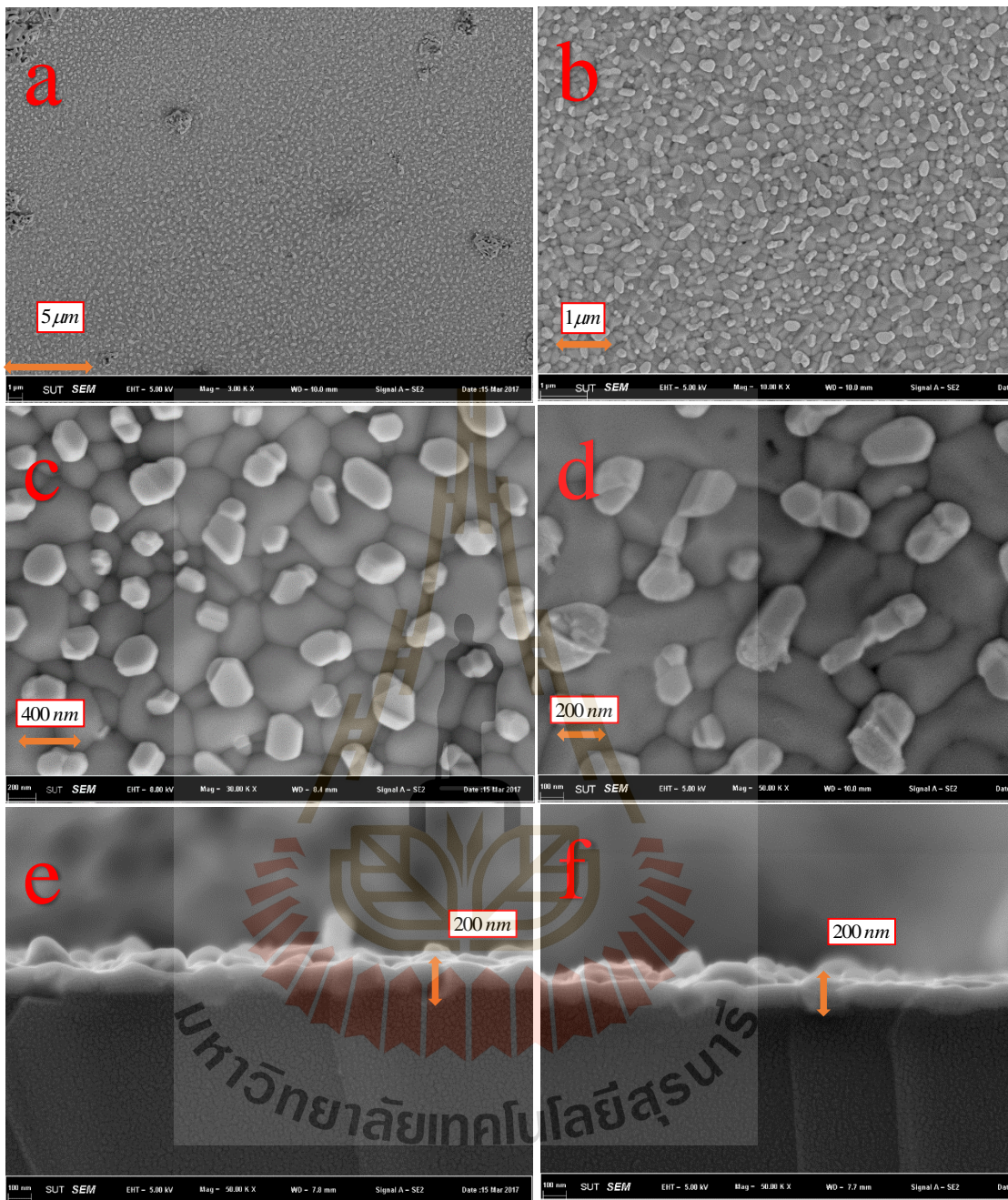


Figure 4.16 Shows SEM and SEM cross section images of $\text{BiFe}_{1-x}\text{Cu}_x\text{O}_3$ thin films as $x=0.1$ (SEM images as, a at 3k, b at 10k, c at 30k and d at 50k, and SEM cross section images as, 50k of e, f).

4.3 X-ray absorption spectroscopy

The x-ray absorption spectroscopy has been used to investigate local oxidation structure of Cu-doped bismuth ferrite thin films elements. The x-ray adsorption mode for measurement absorption spectra of the thin films samples is fluorescent mode because of too much x-ray transition for thin film sample in transition mode. The theory and analysis method of x-ray absorption fluorescent mode had been explained at experimental procedure part. The absorption and x-ray incident energy are used to indicate oxidation state of targets elements atom. The first derivative edge energy shift of reflection intensity coefficient (μ_E) and Energy (eV) are used to plotted x-ray absorption spectra graph. The facility of measurement x-ray absorption had been provided by synchrotron light research institute, Thailand. The x-ray absorption spectroscopy at Fe-K edge of $\text{BiFe}_{1-x}\text{Cu}_x\text{O}_3$ thin films revealed first derivative absorption edge of all samples at Energy $\approx 7,124$ eV. The first derivative absorption Fe K-edge of $\text{BiFe}_{1-x}\text{Cu}_x\text{O}_3$ thin films as $x = 0.0-0.3$ had been compared with Fe K-edge standard of FeO and Fe_2O_3 (SLRI BL 5.2). The first derivative absorption Fe K-edge of $\text{BiFe}_{1-x}\text{Cu}_x\text{O}_3$ thin films are the same Fe K-edge standard of Fe_2O_3 . So, the oxidation state of $\text{BiFe}_{1-x}\text{Cu}_x\text{O}_3$ thin films as $x = 0.0-0.3$ samples are Fe^{3+} . The x-ray absorption spectra Fe K-edge of FeO, Fe_2O_3 and $\text{BiFe}_{1-x}\text{Cu}_x\text{O}_3$ thin films are shown in figure 4.17. The software which have been used to normalize experimental results, are Athena software (Ravel and Newville, 2006).

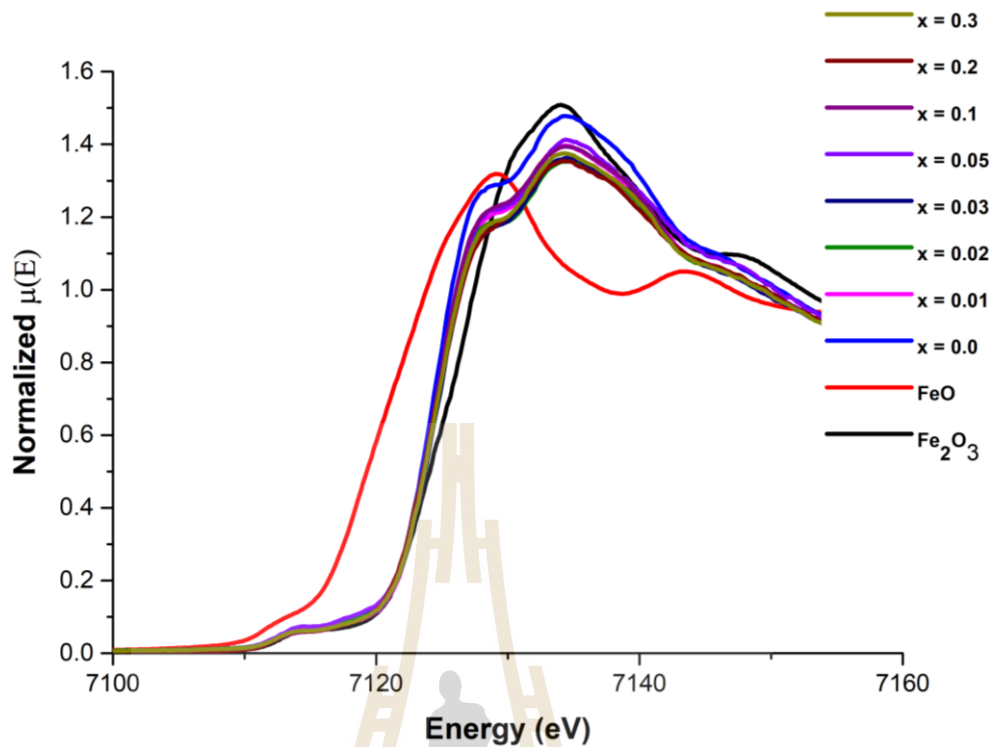


Figure 4.17 Shows x-ray absorption spectra Fe K-edge of $\text{BiFe}_{1-x}\text{Cu}_x\text{O}_3$ thin films as $x = 0.0, 0.01, 0.02, 0.03, 0.05, 0.1, 0.2$ and 0.3 , and FeO , Fe_2O_3 standard.

Then, the Cu K-edge and Bi M5-edge of $\text{BiFe}_{1-x}\text{Cu}_x\text{O}_3$ thin films as $x = 0.0-0.3$ were investigated the oxidation state as the same Fe K-edge method. But, the first derivative absorption Cu K-edge of $\text{BiFe}_{1-x}\text{Cu}_x\text{O}_3$ thin films as $x = 0.0-0.3$ are possible consisted of Cu^{2+} and Cu^{3+} when compared with CuO and CuSO_4 standard (SLRI BL 5.2). Due to the first derivative absorption Cu K-edge of $\text{BiFe}_{1-x}\text{Cu}_x\text{O}_3$ thin films as $x = 0.0-0.3$ are slightly shifted more than CuO and CuSO_4 . The x-ray absorption spectroscopy of Cu K-edge of $\text{BiFe}_{1-x}\text{Cu}_x\text{O}_3$ thin films as $x = 0.0-0.3$, CuO and CuSO_4 are shown in figure 4.18.

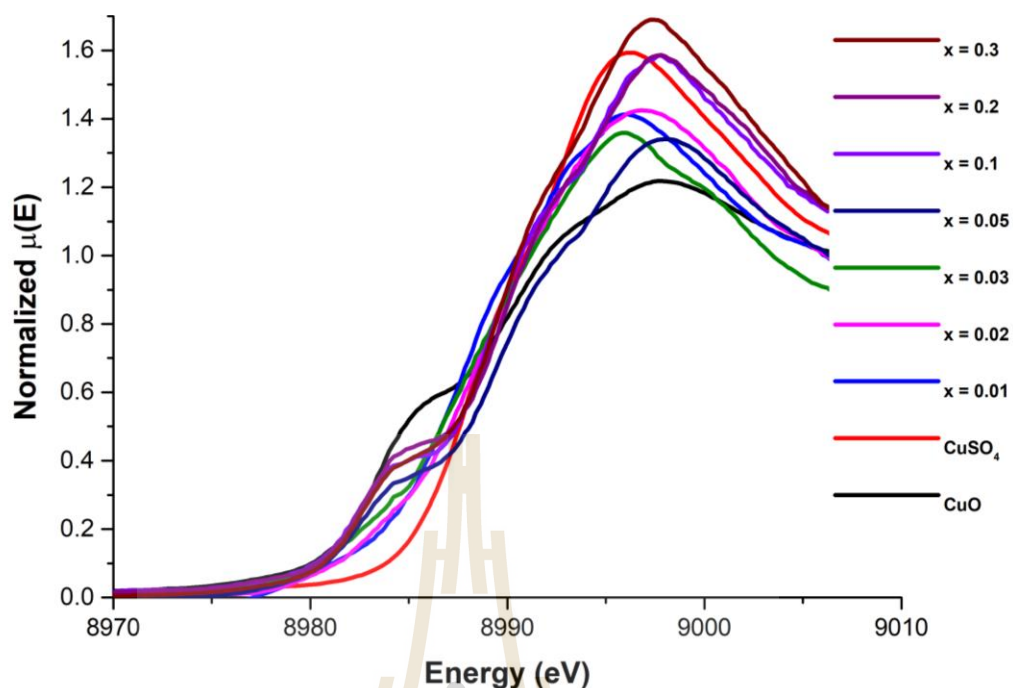


Figure 4.18 Shows x-ray absorption spectra Cu K-edge of $\text{BiFe}_{1-x}\text{Cu}_x\text{O}_3$ thin films as $x = 0.0, 0.01, 0.02, 0.03, 0.05, 0.1, 0.2$ and 0.3 , and CuO , CuSO_4 standard.

The Bi M-edge of $\text{BiFe}_{1-x}\text{Cu}_x\text{O}_3$ thin films were measured x-ray absorption spectra by gas (He) flowing technique because of low x-ray absorption of Bi M5-edge had been disturbed by leakage air. The first derivative absorption Bi M5-edge of $\text{BiFe}_{1-x}\text{Cu}_x\text{O}_3$ thin films as $x = 0.0-0.3$ are shown in figure 4.19. The oxidation state of Bi M-edge of the thin films are Bi^{3+} when compared with Bi M5-edge of Bi_2O_3 standard (SLRI BL 5.2). But, the weak absorption spectra Bi M-edge of $\text{BiFe}_{1-x}\text{Cu}_x\text{O}_3$ thin films led to fluctuate coefficient of reflection intensity which presented in figure 4.19. However, the oxidation state Bi elements of $\text{BiFe}_{1-x}\text{Cu}_x\text{O}_3$ thin films had been confirmed again by x-ray photoelectron spectroscopy at next the section.

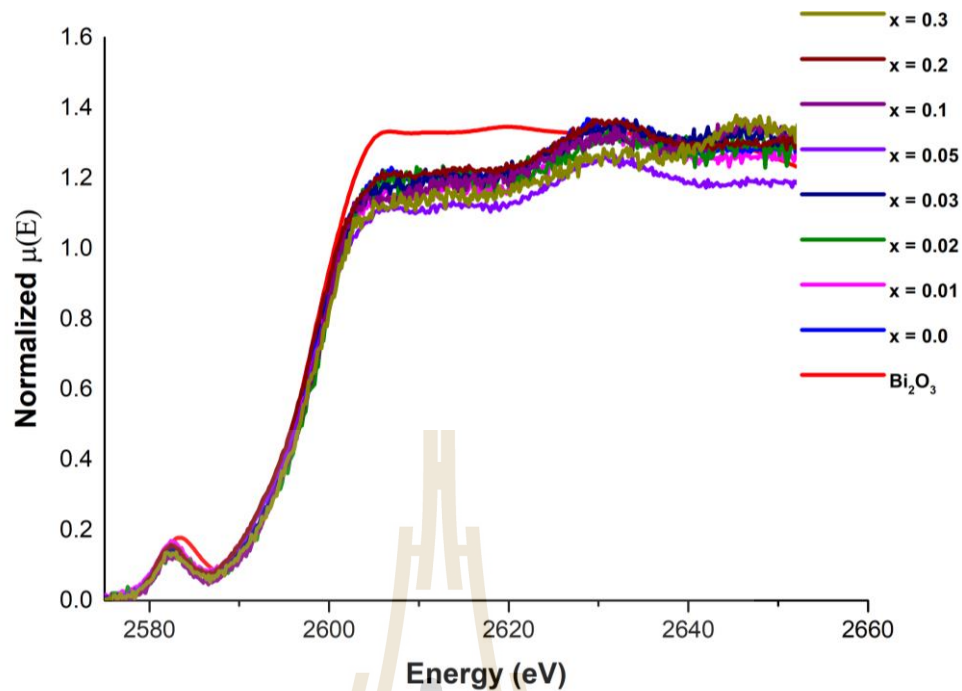


Figure 4.19 Shows x-ray absorption spectra Bi M5-edge of $\text{BiFe}_{1-x}\text{Cu}_x\text{O}_3$ thin films as $x = 0.0, 0.01, 0.02, 0.03, 0.05, 0.1, 0.2$ and 0.3 , and Bi_2O_3 standard.

4.4 X-ray photoelectron spectroscopy

The x-ray photoelectron spectroscopy has been used to reveal binding energy of valence electron shell of materials elements. The electrons emission from samples surface are separated by using kinetic energy measurement probe. The Cu-doped bismuth ferrite thin films as $x = 0.0-0.3$ were investigated valence electron emission kinetic energy to reveal its valence electrons binding energy and its elements oxidation state. The first Bi was the first element, which had been measured x-ray photoelectron spectra because of the x-ray absorption spectra of Bi^{3+} elements are too weak. So, the electrons valence band $\text{Bi } 4f_{5/2}$ and $\text{Bi } 4f_{7/2}$ of Cu-doped bismuth ferrite thin films as $x = 0.0-0.3$ were investigated binding energy. The x-ray photoelectron spectra $\text{Bi } 4f_{5/2}$ and $\text{Bi } 4f_{7/2}$ of $\text{BiFe}_{1-x}\text{Cu}_x\text{O}_3$ thin films are shown in figure 4.20 and figure 4.21. The

electrons binding energy Bi $4f_{5/2}$ and Bi $4f_{7/2}$ of the thin films stayed at 164.5 eV and 159 eV. From figure 4.20 and figure 4.21, the electrons binding energy Bi $4f_{5/2}$ and Bi $4f_{7/2}$ indicate to $\text{Bi}^{3+} 4f_{5/2}$ and $\text{Bi}^{3+} 4f_{7/2}$ when compared with $\text{Bi}^{3+} 4f_{5/2}$ and $\text{Bi}^{3+} 4f_{7/2}$ binding energy standard (<https://xpssimplified.com/elements/bismuth.php>). So, the Bi^{3+} oxidation state of $\text{BiFe}_{1-x}\text{Cu}_x\text{O}_3$ thin films as $x = 0.0-0.3$ are confirmed by XAS and XPS.

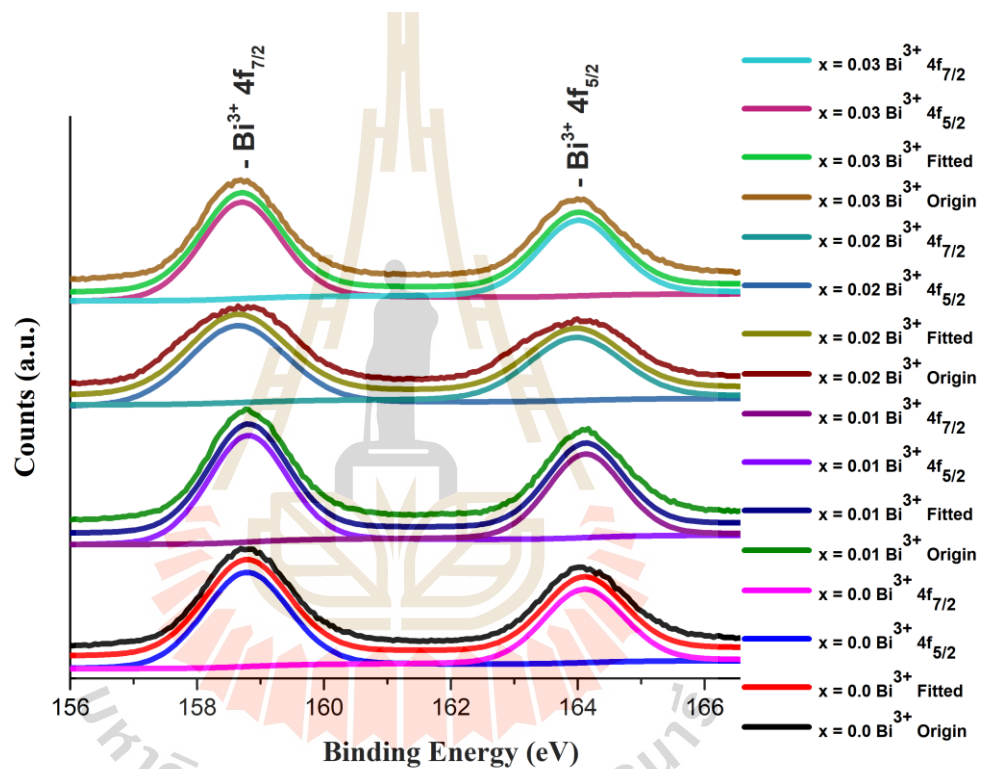


Figure 4.20 Shows x-ray photoelectron spectra valence electron Bi $4f_{5/2}$ and Bi $4f_{7/2}$ of $\text{BiFe}_{1-x}\text{Cu}_x\text{O}_3$ thin films as $x = 0.0, 0.01, 0.02$ and 0.03 .

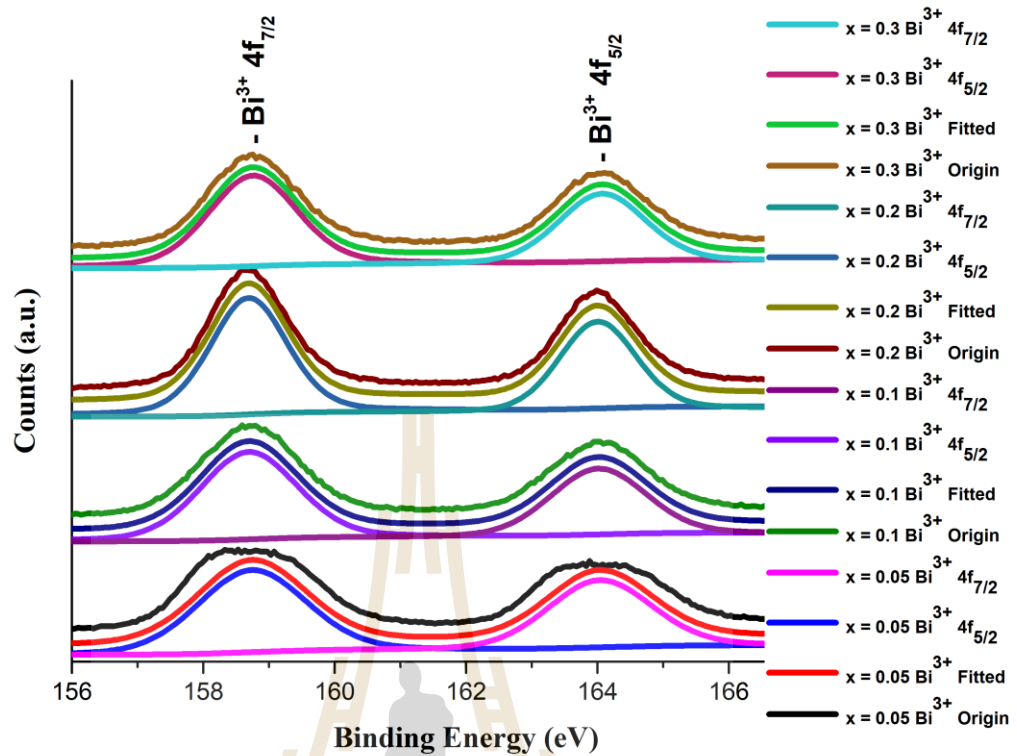


Figure 4.21 Shows x-ray photoelectron spectra valence electron Bi $4f_{5/2}$ and Bi $4f_{7/2}$ of $\text{BiFe}_{1-x}\text{Cu}_x\text{O}_3$ thin films as $x = 0.05, 0.1, 0.2$ and 0.3 .

Then, valence electrons Fe $2p_{1/2}$, $2p_{3/2}$ and Cu $2p_{1/2}$, $2p_{3/2}$ of the $\text{BiFe}_{1-x}\text{Cu}_x\text{O}_3$ thin films were measured binding energy at the same method of Bi $4f_{5/2}$ and Bi $4f_{7/2}$. The number of emission valence electrons Fe $2p_{1/2}$ and $2p_{3/2}$ of the thin films are weak than Bi $4f_{5/2}$ and Bi $4f_{7/2}$, but it is still enough for analysis its binding energy. The electrons binding energy Fe $2p_{1/2}$ and $2p_{3/2}$ of $\text{BiFe}_{1-x}\text{Cu}_x\text{O}_3$ thin films as $x = 0.0-0.3$ are about 725.2 and 711.3 eV, respectively. From figure 4.22 and figure 4.23, the electrons binding energy Fe $2p_{1/2}$ and $2p_{3/2}$ of $\text{BiFe}_{1-x}\text{Cu}_x\text{O}_3$ thin films as $x = 0.0-0.3$ indicate to $\text{Fe}^{3+} 2p_{1/2}$ and $\text{Fe}^{3+} 2p_{3/2}$ when compared with binding energy standard (<https://xpsimplified.com/elements/iron.php>). However, for the count number of valence electrons emission Cu $2p_{1/2}$ and Cu $2p_{3/2}$ of the $\text{BiFe}_{1-x}\text{Cu}_x\text{O}_3$ thin films are too weak and cannot

identify the valence electron binding energy $\text{Cu } 2p_{1/2}$ and $\text{Cu } 2p_{3/2}$ of $\text{BiFe}_{1-x}\text{Cu}_x\text{O}_3$ thin films. But, trying to fix binding energy valence electron $\text{Cu}^{2+} 2p_{3/2}$ of $\text{BiFe}_{1-x}\text{Cu}_x\text{O}_3$ thin films as $x = 0.0-0.3$. are shown in figure 4.24 and figure 4.25.

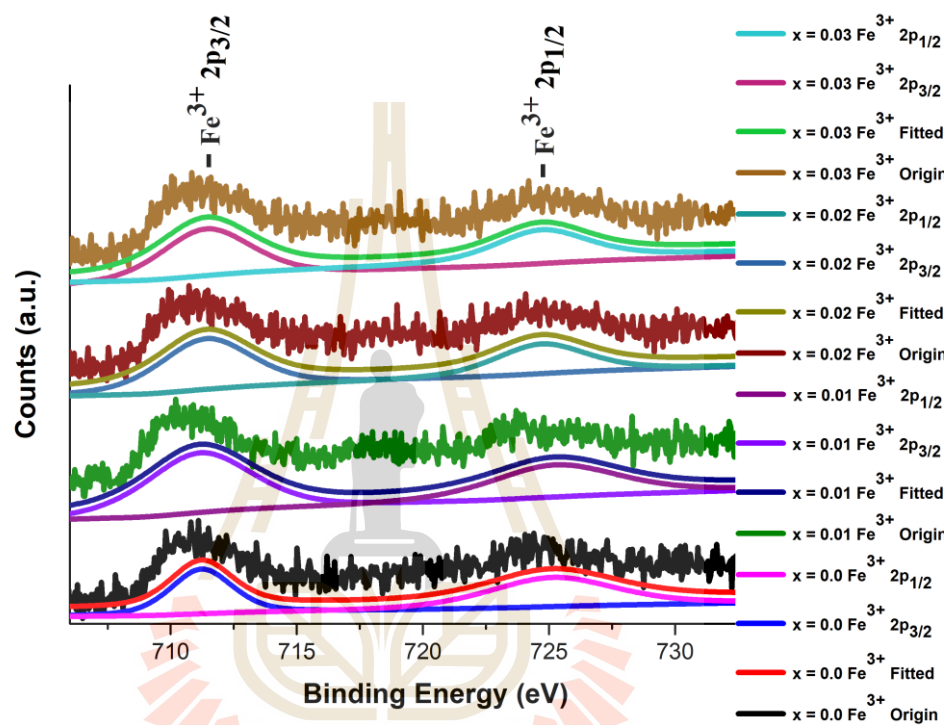


Figure 4.22 Shows x-ray photoelectron spectra valence electron $\text{Fe}^{3+} 2p_{3/2}$ and $\text{Fe}^{3+} 2p_{1/2}$ of $\text{BiFe}_{1-x}\text{Cu}_x\text{O}_3$ thin films as $x = 0.00, 0.01, 0.02$ and 0.03 .

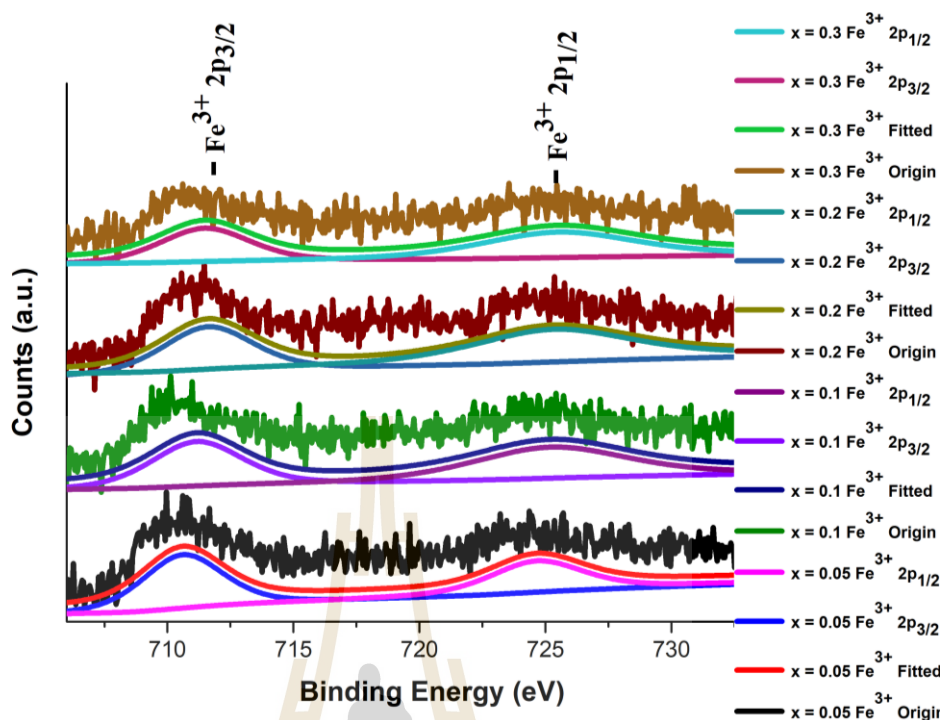


Figure 4.23 Shows x-ray photoelectron spectra valence electron $\text{Fe}^{3+} 2p_{1/2}$ and $\text{Fe}^{3+} 2p_{3/2}$ of $\text{BiFe}_{1-x}\text{Cu}_x\text{O}_3$ thin films as $x = 0.05, 0.1, 0.2$ and 0.3 .

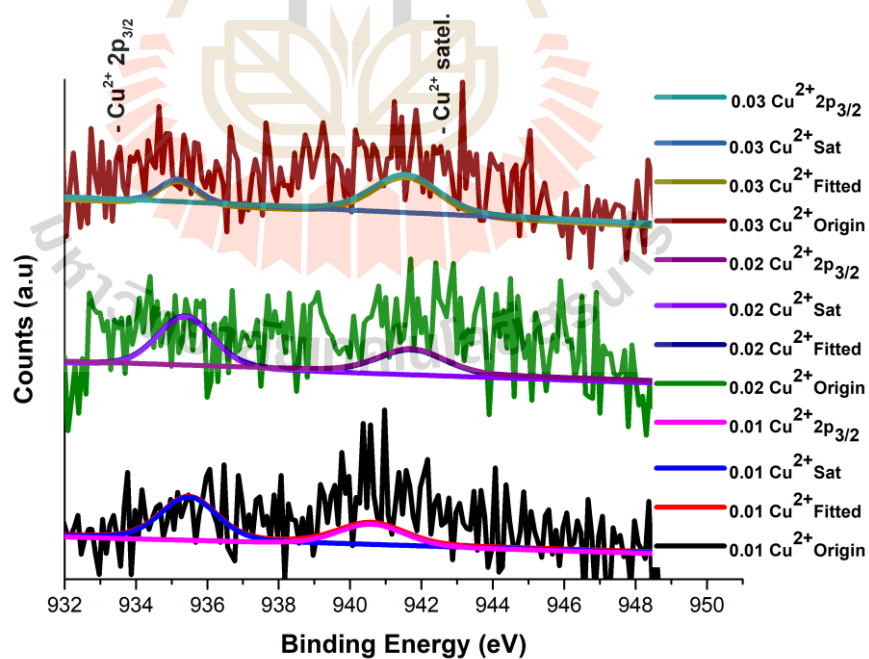


Figure 4.24 Shows x-ray photoelectron spectra valence electron $\text{Cu}^{3+} 2p_{1/2}$ and $\text{Cu}^{3+} 2p_{3/2}$ of $\text{BiFe}_{1-x}\text{Cu}_x\text{O}_3$ thin films as $x = 0.01, 0.02$ and 0.03 .

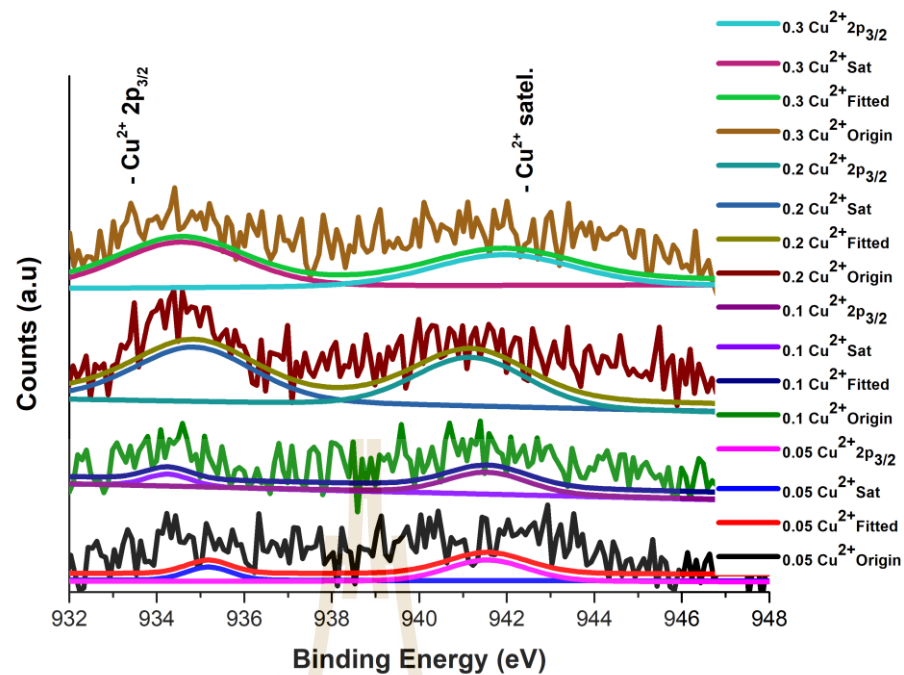


Figure 4.25 Shows x-ray photoelectron spectra valence electron $\text{Cu}^{3+} 2p_{1/2}$ and $\text{Cu}^{3+} 2p_{3/2}$ of $\text{BiFe}_{1-x}\text{Cu}_x\text{O}_3$ thin films as $x = 0.05, 0.1, 0.2$ and 0.3 .

Another benefit of XPS technique, x-ray photoelectron spectra can be used to indicate oxygen bonding metals element O 1s and defect oxygen O_v . So, the valence electron O 1s and O_v of $\text{BiFe}_{1-x}\text{Cu}_x\text{O}_3$ thin films as $x = 0.0-0.3$ were measured valence electron kinetic energy. The electrons emission binding O 1s and O_v of $\text{BiFe}_{1-x}\text{Cu}_x\text{O}_3$ thin films as $x = 0.0-0.3$ are about 529 eV and 531.2 eV. From figure 4.26 and figure 4.27, the O 1s and O_v binding energy of $\text{BiFe}_{1-x}\text{Cu}_x\text{O}_3$ thin films are confirm existence of oxygen bonding metals and defect oxygen within the thin films when compared the O 1s binding energy with binding energy standard (<https://xpssimplified.com/elements/iron.php>), and with literature review reports (Mishra *et al.*, 2012; Li *et al.*, 2013).

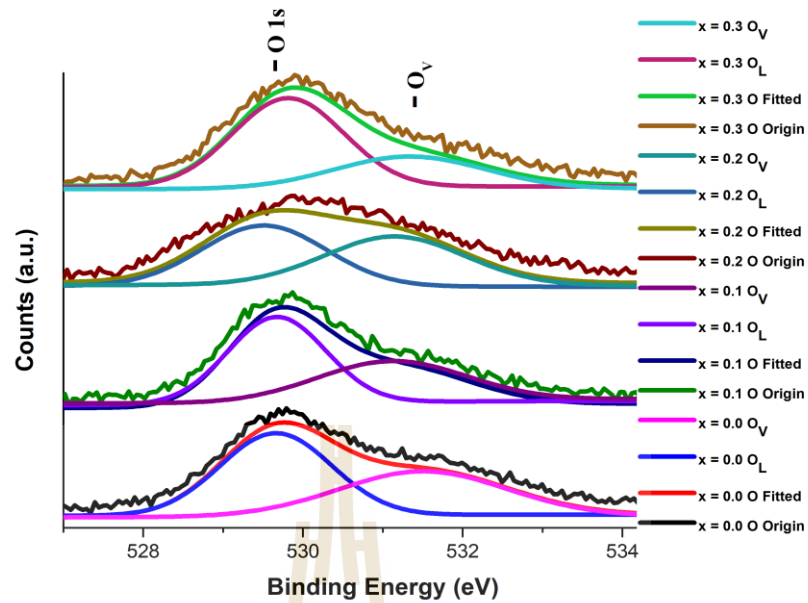


Figure 4.26 Shows x-ray photoelectron spectra valence electron O 1s and O_v of BiFe_{1-x}Cu_xO₃ thin films as x = 0.00, 0.01, 0.02 and 0.03.

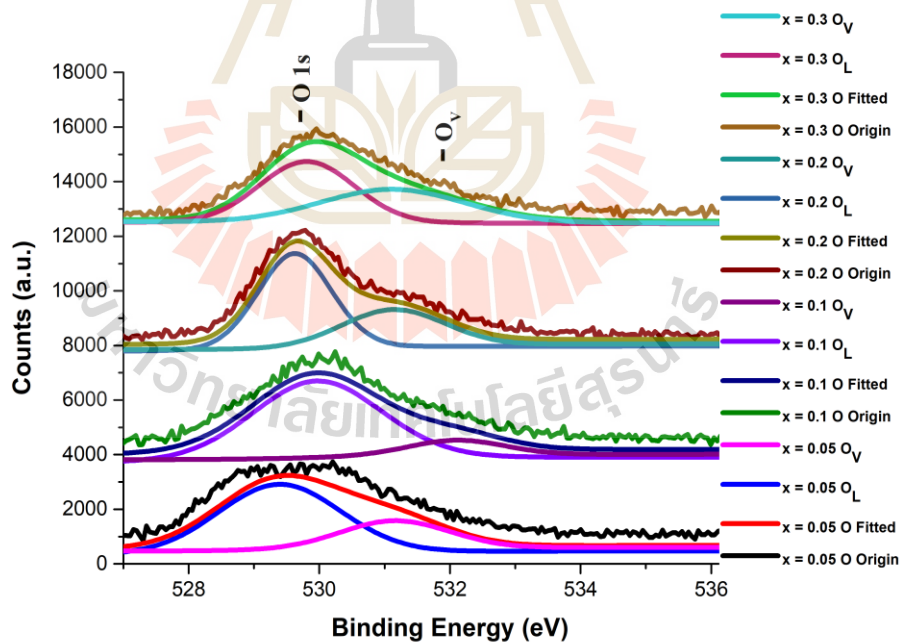


Figure 4.27 Shows x-ray photoelectron spectra valence electron O 1s and O_v of BiFe_{1-x}Cu_xO₃ thin films as x = 0.00, 0.01, 0.02 and 0.03.

The binding energy position, counts valence electron intensity, full width at half maximum, Gauss fixed quantity and Chisquared of photoelectrons emission values of $\text{Bi}^{3+} 4f_{5/2}$, $\text{Bi}^{3+} 4f_{7/2}$, $\text{Fe}^{3+} 2p_{1/2}$, $\text{Fe}^{3+} 2p_{3/2}$, O 1s and O_v are shown in tables 4.1, 4.2 and 4.3, respectively.

Table 4.1 Shows binding energy positions counts valence electron intensity, full width at half maximum and Gauss fixed quantity $\text{Bi}^{3+} 4f_{5/2}$ and $\text{Bi}^{3+} 4f_{7/2}$ of $\text{BiFe}_{1-x}\text{Cu}_x\text{O}_3$ thin films as $x = 0.0-0.3$.

Cu doped contents (x)	B.E. position eV		Counts number		FWHM		Gauss %	
	$\text{Bi}^{3+} 4f_{5/2}$	$\text{Bi}^{3+} 4f_{7/2}$						
	0.0	164.1	158.7	11745	15211	1.50	1.58	85
0.01	164.1	158.8	13317	17235	1.41	1.47	85	85
0.02	163.9	158.6	9797	12744	1.74	1.81	85	85
0.03	164.0	158.7	11925	15766	1.50	1.51	85	79
0.05	164.0	158.7	10472	12765	1.86	1.94	85	85
0.1	164.0	158.6	10359	13474	1.71	1.72	85	85
0.2	164.0	158.6	13739	17912	1.37	1.37	85	77
0.3	164.0	158.7	10679	13938	1.58	1.58	80	79

Table 4.2 Shows binding energy positions counts valence electron intensity, full width at half maximum and Gauss fixed quantity $\text{Fe}^{3+} 2p_{1/2}$ and $\text{Fe}^{3+} 2p_{3/2}$ of $\text{BiFe}_{1-x}\text{Cu}_x\text{O}_3$ thin films as $x = 0.0-0.3$.

Cu doped contents (x)	B.E. position eV		Counts number		FWHM		Gauss %	
	$\text{Fe}^{3+} 2p_{1/2}$	$\text{Fe}^{3+} 2p_{3/2}$						
0.0	725.1	711.2	245	378	6.00	2.93	60	60
0.01	725.2	711.1	267	510	6.00	5.05	60	60
0.02	724.6	711.4	250	429	4.34	4.34	60	60
0.03	724.6	711.2	252	426	4.30	4.34	60	60
0.05	724.6	710.6	222	396	4.34	3.84	60	60
0.1	725.2	711.1	224	332	7.27	4.34	60	60
0.2	725.3	711.6	216	337	7.27	4.34	60	60
0.3	725.5	711.4	180	253	7.27	4.34	60	60

Table 4.3 Shows binding energy positions counts valence electron intensity, full width at half maximum and Gauss fixed quantity O 1s and O_v of BiFe_{1-x}Cu_xO₃ thin films as x = 0.0-0.3.

Cu doped contents (x)	B.E. position eV		Counts number		FWHM		Gauss %	
	O 1s	O _v	O 1s	O _v	O 1s	O _v	O 1s	O _v
0.0	529.6	531.5	2860	1582	1.64	2.50	90	93
0.01	529.6	531.1	3022	1371	1.44	2.18	90	94
0.02	529.5	531.1	2113	1721	1.84	2.09	100	90
0.03	529.8	531.3	3083	1116	1.63	2.21	100	100
0.05	529.3	531.1	2.20	1.96	2529	1014	100	100
0.1	529.9	532.1	2.35	1.74	7673	1057	90	95
0.2	529.6	531.1	1.33	1.83	3540	1320	90	100
0.3	529.8	531.1	1.72	2.58	2241	1210	100	100

4.5 Magnetic properties

The magnetic properties of bismuth ferrite are well known as antiferromagnetic properties (Li *et al.*, 2013). In this research, the BiFe_{1-x}Cu_xO₃ thin films. Were studied magnetic properties by analysis saturation magnetization, remanent magnetization, coercive force and magnetic susceptibility. The BiFe_{1-x}Cu_xO₃ thin films were investigated magnetic behavior by vibration sample magnetometer. The magnetization of BiFe_{1-x}Cu_xO₃ thin films had been converted to emu/cm³ unit and Oe unit for convenient calculation. Magnetic hysteresis loop had been used to study magnetic kinds of BiFe_{1-x}Cu_xO₃ thin films as x = 0.0-0.3 at 298 K. The hysteresis loop of BiFe_{1-x}Cu_xO₃ thin films as x = 0.0-0.3 at 298 K are shown in figure 4.28.

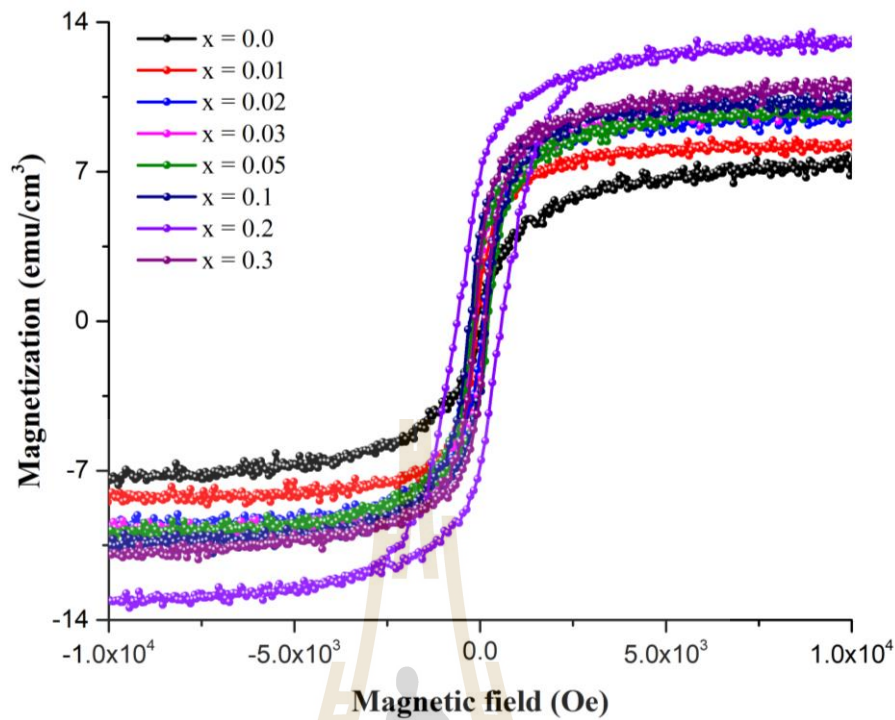


Figure 4.28 Shows hysteresis loop of $\text{BiFe}_{1-x}\text{Cu}_x\text{O}_3$ thin films as $x = 0.00, 0.01, 0.02, 0.03, 0.05, 0.1, 0.2$ and 0.3 .

From figure 4.28, the saturation magnetization of $\text{BiFe}_{1-x}\text{Cu}_x\text{O}_3$ thin films increased for $M_s \approx 6.0, 7.7, 9.0, 9.1, 9.5, 10.1$ and 12.5 emu/cm^3 with increasing Cu-doping as $x = 0.0, 0.01, 0.02, 0.03, 0.05, 0.1,$ and 0.2 . But, the saturation magnetization had been decreased to $M_s \approx 10.4 \text{ emu/cm}^3$ when Cu doping contents were doped as $x = 0.3$. It is the same increment as remanent magnetization and coercive force, which increased for $M_r \approx 1.5, 3.0, 4.5, 5.1, 5.1, 6.0, 8.2 \text{ emu/cm}^3$, and $H_c \approx 55, 120, 185, 240, 250, 260, 650 \text{ Oe}$ with increasing Cu-doping as $x = 0.0, 0.01, 0.02, 0.03, 0.05, 0.1, 0.2$. But, remanent magnetization and coercive force had been decreased to $M_r \approx 6.1 \text{ emu/cm}^3$, and $H_c \approx 220 \text{ Oe}$ when Cu doping content were doped as $x = 0.3$. The increment graphs are shown in figure 4.29-4.30. The increasing of saturation

magnetization, remanent magnetization and coercive force indicate to increase ferromagnetic behavior of $\text{BiFe}_{1-x}\text{Cu}_x\text{O}_3$ thin films. The increasing ferromagnetism of the thin films are evident of $\text{CuO-Cu}_2\text{O}_3$ double exchange effect, which involved with mixture oxidation state of $\text{Cu}^{2+}, \text{Cu}^{3+}$. The existence of $\text{Cu}^{2+}, \text{Cu}^{3+}$ had been investigated by x-ray absorption spectra Cu K-edge of the thin films. Moreover, increasing of ferromagnetic behaviour of the thin films are also evident of existence of oxygen defects, which had been investigated by x-ray photoelectron spectra valence electron O_{1s} and O_v of the thin films. Due to the oxygen defect lead to occur free single valence electron of metals oxide materials (Li *et al.*, 2013). The single valence electron of metals oxide materials are easy induced its magnetic moment direction by applying external magnetic field (Li *et al.*, 2013)

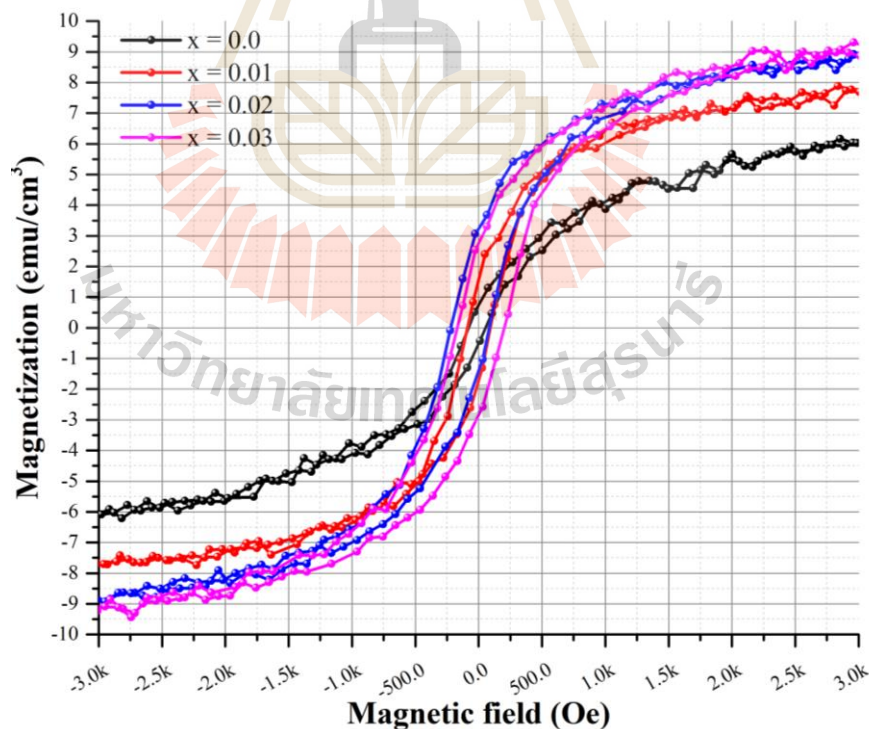


Figure 4.29 Shows hysteresis loop grid scales of $\text{BiFe}_{1-x}\text{Cu}_x\text{O}_3$ thin films as $x = 0.00$, 0.01 , 0.02 and 0.03 .

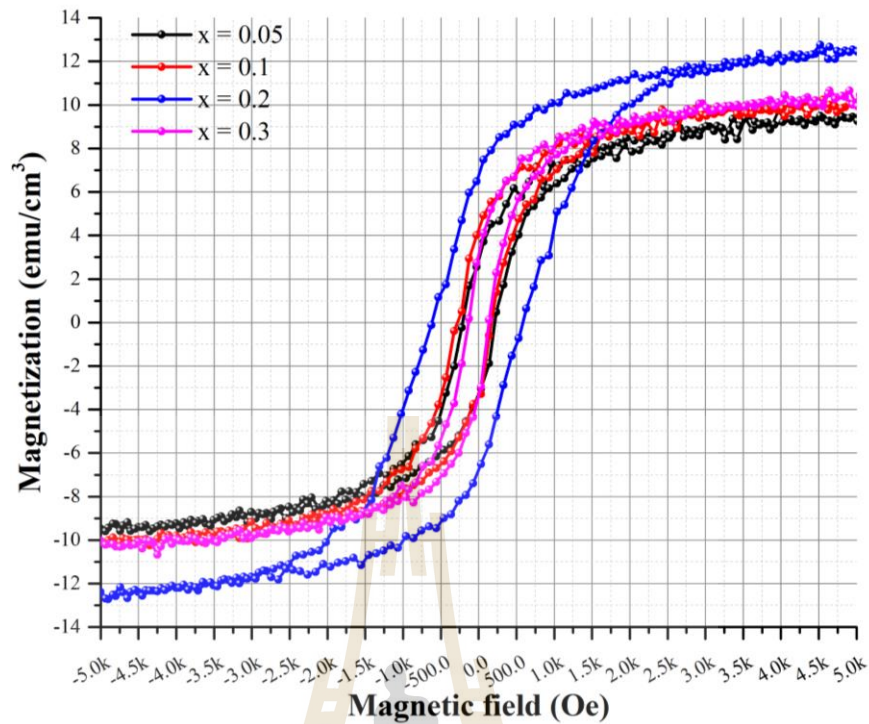


Figure 4.30 Shows hysteresis loop on grid scales of $\text{BiFe}_{1-x}\text{Cu}_x\text{O}_3$ thin films as $x = 0.05, 0.1, 0.2$ and 0.3 .

Another indicator which has been used to indicate magnetic behavior, is temperature dependence of magnetic susceptibility. The theory and calculation had been explained at literature review part (Lin *et al.*, 2015). Normally, the susceptibility is calculated by average proportion of $\frac{M}{H}$ at small magnetization and small applying external magnetic field. However, the coercive force of $\text{BiFe}_{1-x}\text{Cu}_x\text{O}_3$ thin films are narrow hysteresis loop. So, the susceptibility had been approximated by susceptibility point of $\frac{M}{H}$ (Jun L. *et al.*, 2010). Then, the environment temperature was varied from 400 K to 50 K for study temperature dependence of susceptibility. Due to measurement temperature dependence of susceptibility need to use time for measurement about 7 hours per samples. So, the $\text{BiFe}_{1-x}\text{Cu}_x\text{O}_3$ thin films as $x = 0.0$,

0.02, 0.05 and 0.2 were selected for survey of the susceptibility measurement. The temperature dependence of magnetic susceptibility is shown in figure 4.31 and figure 4.32.

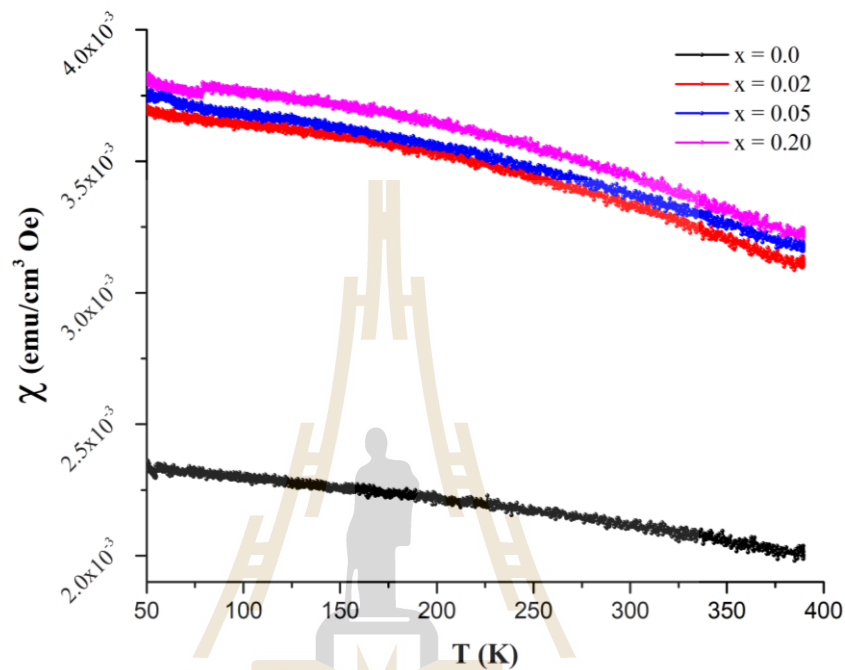


Figure 4.31 Shows temperature dependence of susceptibility $\text{BiFe}_{1-x}\text{Cu}_x\text{O}_3$ thin films as $x = 0.0, 0.02, 0.05$ and 0.2 at 2.5 kOe.

The coercive force of $\text{BiFe}_{1-x}\text{Cu}_x\text{O}_3$ thin films revealed a little shifting of magnetic hysteresis loop axis in figure 4.29 and 4.30. The shifting had occurred due to mixture of antiferromagnetic materials and ferromagnetic materials, which lead to a little shift of magnetic hysteresis loop axis. This phenomenon calls exchange anisotropy or exchange bias, which possible applied to spin valve device in hard disk reader probe (Choudhuri *et al.*, 2014) . From literature reviews, the exchange bias phenomenon occurred at low temperature $T \approx 5$ K (Schumacher *et al.*, 2013). But in this work, exchange bias occurred at room temperature, according to figure 4.29 and 4.30.

From figure 4.32, the temperatures dependence of susceptibility $\text{BiFe}_{1-x}\text{Cu}_x\text{O}_3$ thin films reveals neel temperature point at nearly 50 K of Cu-doping $x = 0.5$, and at 80 K of Cu-doping $x = 0.2$. The neel temperature increasing of $\text{BiFe}_{1-x}\text{Cu}_x\text{O}_3$ thin films indicated to increase ferromagnetism behavior of $\text{BiFe}_{1-x}\text{Cu}_x\text{O}_3$ thin films. So, it clearly that Cu doping have enhanced ferromagnetism of $\text{BiFe}_{1-x}\text{Cu}_x\text{O}_3$ thin films.

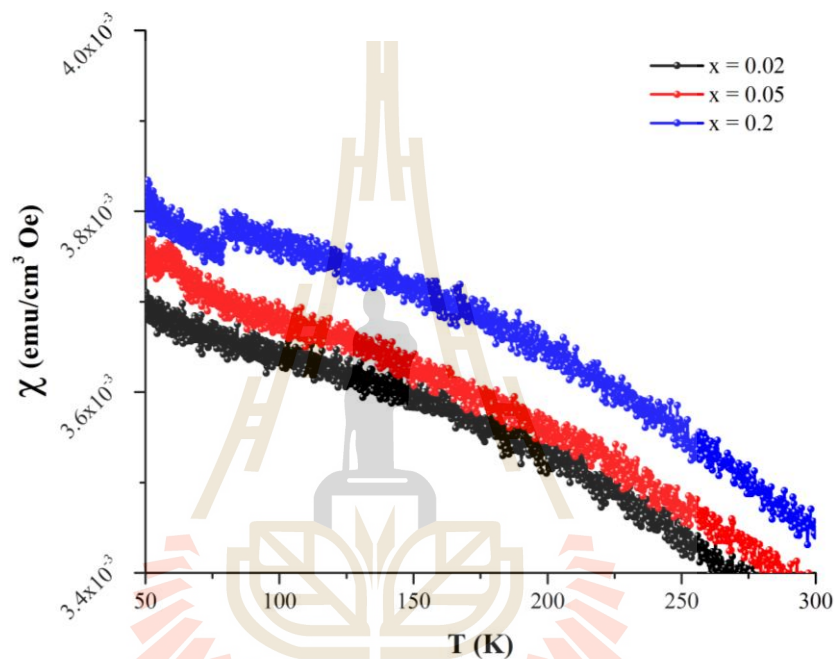


Figure 4.32 Shows temperature dependence of susceptibility of $\text{BiFe}_{1-x}\text{Cu}_x\text{O}_3$ thin films as $x = 0.02, 0.05$ and 0.2 at 2.5 kOe.

The saturation magnetization, remanent magnetization and coercive force values of $\text{BiFe}_{1-x}\text{Cu}_x\text{O}_3$ thin films as $x = 0.0, 0.01, 0.02, 0.03, 0.05, 0.1, 0.2$ and 0.3 are show in table 4.4.

Table 4.4 Shows list of saturation magnetization, remanent magnetization and coercive force of $\text{BiFe}_{1-x}\text{Cu}_x\text{O}_3$ thin films as $x = 0.0, 0.01, 0.02, 0.03, 0.05, 0.1, 0.2$ and 0.3 .

Cu-doped contents (x)	Saturation Magnetization M_s (emu/cm ³)	Remanent Magnetization M_r (emu/cm ³)	Coercivity Force H_c (Oe)
0.0	6.0	1.5	55
0.01	7.7	3.0	120
0.02	9.0	4.5	185
0.03	9.1	5.1	240
0.05	9.5	5.1	250
0.1	10.1	6.0	260
0.2	12.5	8.2	650
0.3	10.4	6.1	220

4.6 Electrical properties

The electrical properties of the thin films had been measured by Agilent 4294A Precision impedance analyser. The ϵ' and ϵ'' are measured and calculated by dielectric calculation method which were explained in literature review part. The conductivity of the thin films was considered by dielectric permittivity and loss tangent parameters. The loss tangent has used to indicate leakage current while the real part of dielectric permittivity is used to describe resistivity. The complex impedance spectroscopy has been converted to grain and grain boundary of resistance, and conductance by equation (2.18). The real permittivity ϵ' and imaginary permittivity ϵ'' of $\text{BiFe}_{1-x}\text{Cu}_x\text{O}_3$ thin films, and loss tangent of $\text{BiFe}_{1-x}\text{Cu}_x\text{O}_3$ thin films are shown in figure 4.33, 4.34 and 4.35.

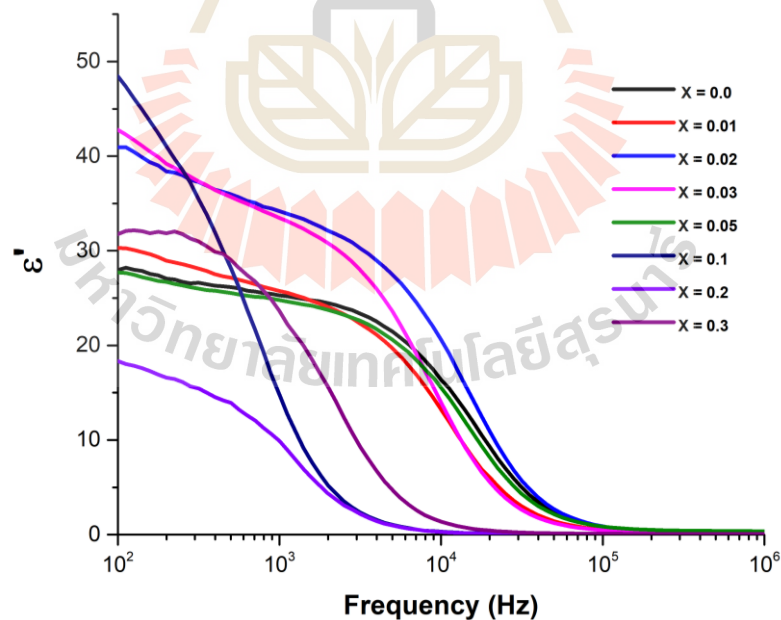


Figure 4.33 Shows frequency dependence of real part dielectric permittivity of $\text{BiFe}_{1-x}\text{Cu}_x\text{O}_3$ thin films as $x = 0.0, 0.01, 0.02, 0.03, 0.05, 0.1, 0.2$ and 0.3 .

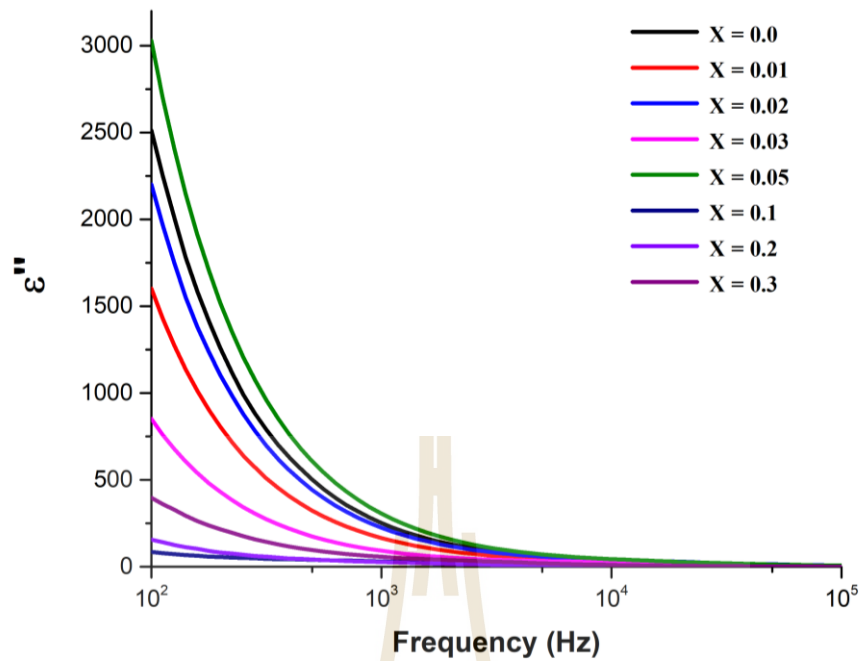


Figure 4.34 Shows frequency dependence of imaginary part dielectric permittivity of $\text{BiFe}_{1-x}\text{Cu}_x\text{O}_3$ thin films as $x = 0.0, 0.01, 0.02, 0.03, 0.05, 0.1, 0.2$ and 0.3 .

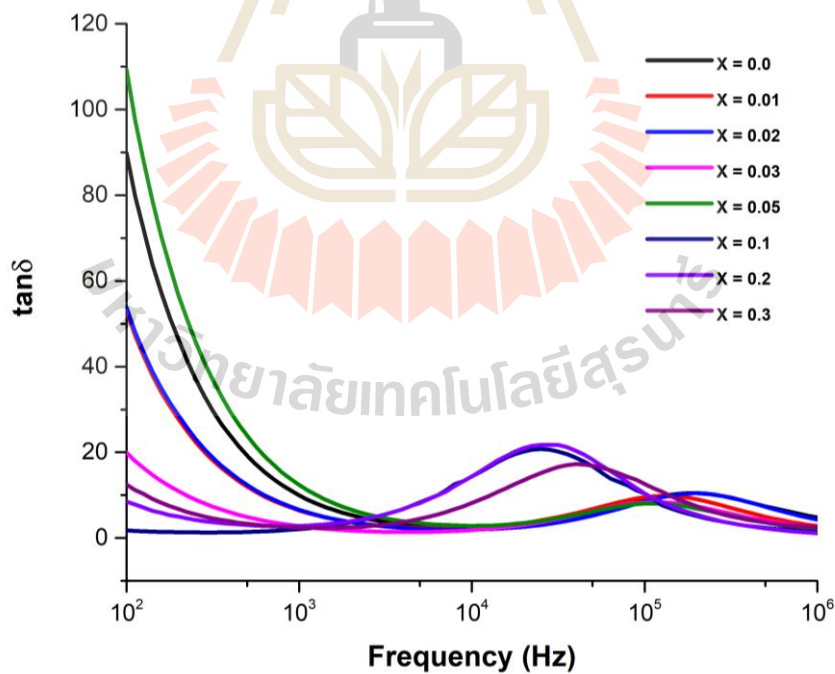


Figure 4.35 Shows frequency dependence of loss tangent of $\text{BiFe}_{1-x}\text{Cu}_x\text{O}_3$ thin films as $x = 0.0, 0.01, 0.02, 0.03, 0.05, 0.1, 0.2$ and 0.3 .

From figure 4.33, the real part dielectric permittivity of $\text{BiFe}_{1-x}\text{Cu}_x\text{O}_3$ thin films, were nonlinear trend with increasing Cu-doped content (Shah *et al.*, 2015). The highest of real dielectric permittivity constant of $\text{BiFe}_{1-x}\text{Cu}_x\text{O}_3$ thin films are stayed at Cu-doped as $x = 0.1$. The loss tangent and imaginary part dielectric permittivity also are nonlinear trend with increasing Cu-doped content. The experimental results of real part dielectric permittivity and conductivity of the thin films were considered by trend for 2 case with Cu doping quantity. The first, the increment of real part dielectric permittivity as Cu-doped $x = 0.0-0.03$ were describe by increasing of grain size due to enhancement of crystallite sizes of the thin films. The increment of crystallite sizes leaded to increasing of grain size, which conducted to increase complex mobility of charges within the thin films (Rhidwan *et al.*, 2017). However, some work the increment of crystallite sizes did not lead to increasing of grain size (Lopez Maldonado *et al.*, 2014). The second case, decreasing real part dielectric permittivity of $\text{BiFe}_{1-x}\text{Cu}_x\text{O}_3$ thin films as $x = 0.1-0.3$ were gave a reasoned explanation by increasing of $\text{Bi}_2\text{Fe}_4\text{O}_9$ phase. Due to the decreasing of ϵ' did not involve with crystallite size effect, according to crystallite sizes in figure 4.14. So, increment of $\text{Bi}_2\text{Fe}_4\text{O}_9$ phase was conducive to increasing of the real part dielectric. Imaginary part dielectric permittivity trend looked like loss tangent trend because of straight related between ϵ'' and ϵ' for $\epsilon'' = \epsilon' \tan \delta$ (Boonlakhorn *et al.*, 2014). The conductivity also straight related to imaginary part dielectric permittivity.

Moreover, the complex impedance spectroscopy was used to define resistance and conductance indicator of the thin films by fitting parameter of $R_g, R_{gb}, C_g, C_{gb}, \sigma_g$ and σ_{gb} , according to ideal complex impedance circuit of two parallel of R and C in figure 2.8. The original complex impedance spectra of

$\text{BiFe}_{1-x}\text{Cu}_x\text{O}_3$ thin films as $x = 0.0, 0.01, 0.02, 0.03, 0.05, 0.1, 0.2$ and 0.3 are shown in figure 4.36. The fitted complex impedance spectroscopy is shown in figure 4.37.

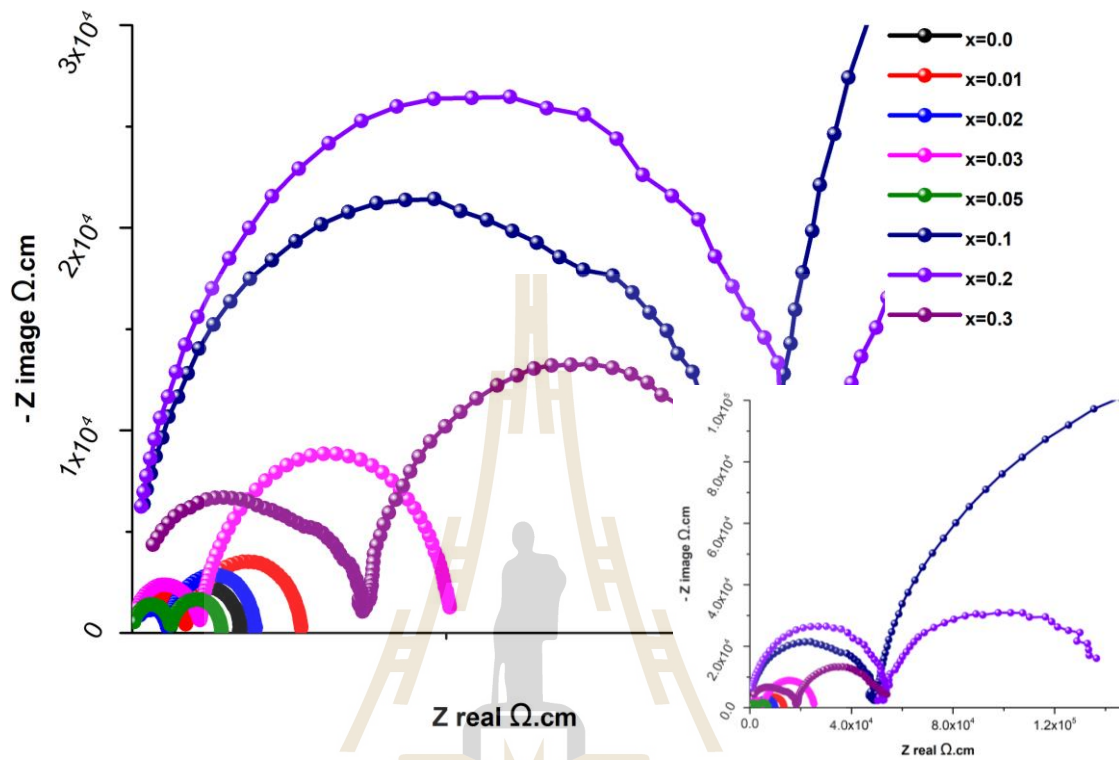


Figure 4.36 Shows original complex impedance spectra of $\text{BiFe}_{1-x}\text{Cu}_x\text{O}_3$ thin films as $x = 0.0, 0.01, 0.02, 0.03, 0.05, 0.1, 0.2$ and 0.3 .

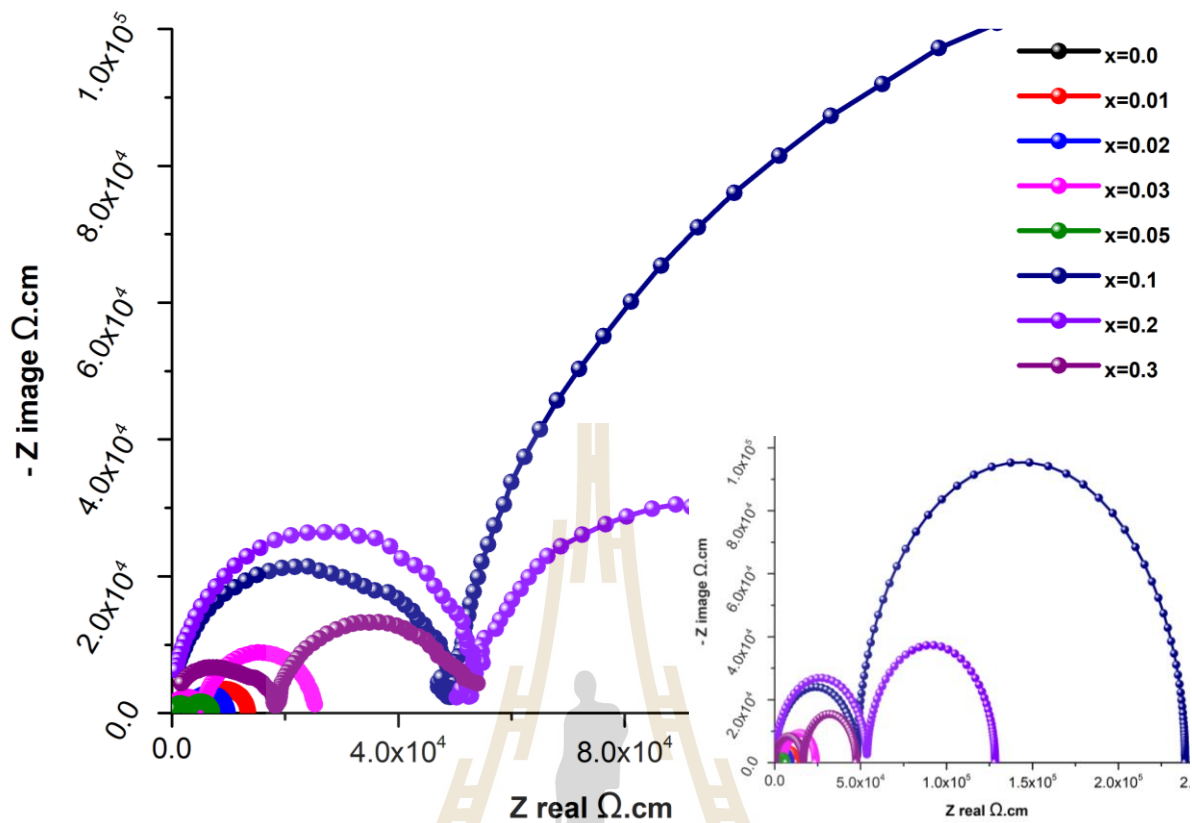


Figure 4.37 Shows fitted complex impedance spectra of $\text{BiFe}_{1-x}\text{Cu}_x\text{O}_3$ thin films as $x = 0.0, 0.01, 0.02, 0.03, 0.05, 0.1, 0.2$ and 0.3 .

From complex impedance spectra of $\text{BiFe}_{1-x}\text{Cu}_x\text{O}_3$ thin films, the grain and grain boundary of resistance increased with increasing Cu doping content for $x = 0.0$ to 0.03 , and $x = 0.05$ to 0.1 . But, the grain and grain boundary of resistance decreased with increasing Cu-doping element for $x = 0.03$ to 0.05 , and $x = 0.1$ to 0.3 . These increment trend of grain and grain boundary resistance also occurred with another metals doped bismuth ferrite (Riaz *et al.*, 2015; Dong *et al.*, 2014). The nonlinear of grain and grain boundary resistance were gave a reasoned explanation by increasing of complex charge mobility and increasing of $\text{Bi}_2\text{Fe}_4\text{O}_9$ phase. The grain and grain boundary conductive were calculated by inverse relation of $\sigma = \frac{1}{R}$, according to Arrheius's law

(Boonlakhorn *et al.*, 2014). The $R_g, R_{gb}, C_g, C_{gb}, \sigma_g$ and σ_{gb} quantities of $\text{BiFe}_{1-x}\text{Cu}_x\text{O}_3$ thin films as $x = 0.0-0.3$ are shown in table 4.5. The fitting software which used in this research are EIS Spectrum Analyser (Ragoisha and Bondarenko, 2005).

Table 4.5 Shows list of grain and grain boundary of resistance, capacitance and conductance of $\text{BiFe}_{1-x}\text{Cu}_x\text{O}_3$ thin films as $x = 0.0-0.3$.

$\text{BiFe}_{1-x}\text{Cu}_x\text{O}_3$ thin films (x)	R_g $10^3 \Omega.cm$	R_{gb} $10^3 \Omega.cm$	C_g $F.cm$	C_{gb} $F.cm$	σ_g $10^{-4} S.cm$	σ_{gb} $10^{-4} S.cm$
0.0	2.9	5.2	9.0×10^{-12}	5.0×10^{-9}	3.4	1.9
0.01	4.3	8.2	1.2×10^{-11}	5.1×10^{-9}	2.3	1.2
0.02	2.6	6.4	1.2×10^{-11}	5.1×10^{-9}	3.8	1.5
0.03	53.7	74.5	2.5×10^{-12}	4.4×10^{-9}	0.18	0.13
0.05	2.9	3.8	2.5×10^{-11}	6.1×10^{-9}	3.4	2.6
0.1	51.0	190.8	2.5×10^{-12}	5.2×10^{-9}	0.19	0.05
0.2	5.3	74.5	2.5×10^{-12}	4.2×10^{-9}	1.8	0.13
0.3	16.6	30.8	3.5×10^{-12}	5.6×10^{-9}	0.6	0.32

CHAPTER V

CONCLUSIONS AND SUGGESTIONS

In this research, the $\text{BiFe}_{1-x}\text{Cu}_x\text{O}_3$ thin films as $x = 0.0, 0.01, 0.02, 0.03, 0.05, 0.1, 0.2$ and 0.3 had been successful fabricated by sol-gel method and spin coating. The crystallite structure and crystallite size were investigated by x-ray diffraction technique. Morphology of films surface and films thickness were observed by scanning electron microscopy. The local oxidation state element of $\text{BiFe}_{1-x}\text{Cu}_x\text{O}_3$ thin films were investigated by x-ray absorption spectroscopy. The electrons valence binding energy and oxidation state of the thin films elements were revealed by x-ray photoelectron spectroscopy. The magnetic properties of the thin films were revealed by vibration sample magnetometer. The electrical properties of the thin films were studied by complex permittivity and complex impedance spectroscopy. The conclusion was divided to four section of structure and characterization, magnetic properties, electrical properties, and suggestions as follows.

5.1 Structure and characterization

The $\text{BiFe}_{1-x}\text{Cu}_x\text{O}_3$ thin films as $x = 0.0, 0.01, 0.02, 0.03, 0.05, 0.1, 0.2$ and 0.3 were fabricated by acetate route and addition of solvents quantity. The phase structure of bismuth ferrite rhombohedral R3C of the thin films were revealed. But, the thin films were consisted of impurity phase $\text{Bi}_2\text{Fe}_4\text{O}_9$ orthorhombic Pbam phase ICSD #20067 (Tutov A. G. *et al.*, 1980). The crystallites size of the thin film increased with increasing

Cu-doped as $x = 0.0$ to 0.03 . But, the crystallites size decreased with increasing Cu-doped as $x = 0.05$ to 0.3 . The peaks shifting of x-rays diffraction peak for 0.01 degree the thin films confirmed substitution of smaller Cu element to Fe element, consequently peak shift forward (Li *et al.*, 2013)

The morphology films surface of the thin films was nonhomogeneous surface because of mountain films occurred on the films surface. The nonhomogeneous of $\text{BiFe}_{1-x}\text{Cu}_x\text{O}_3$ thin films increased with increasing Cu-doped due to incompletely sintered film grain of $\text{BiFe}_{1-x}\text{Cu}_x\text{O}_3$ thin films, and consequently metals oxide particles spilt out from the films surface. So, increasing Cu doping contents effected directly to increasing nonhomogeneous of films surface. The films thickness of $\text{BiFe}_{1-x}\text{Cu}_x\text{O}_3$ thin films are about 200-300 nm.

The elements oxidation state of $\text{BiFe}_{1-x}\text{Cu}_x\text{O}_3$ thin films were indicated to Fe^{3+} , Bi^{3+} and $\text{Cu}^{2+,3+}$ by x-ray absorption spectroscopy. The oxidation state of Bi^{3+} and Fe^{3+} were confirmed again by x-ray photoelectron spectroscopy. The existences of oxygen defect within $\text{BiFe}_{1-x}\text{Cu}_x\text{O}_3$ thin films had been investigated. The x-ray photoelectron spectra valence electrons of Cu elements are too weak, which leded to unidentified valence electrons state of Cu elements.

5.2 Magnetic properties

The $\text{BiFe}_{1-x}\text{Cu}_x\text{O}_3$ thin films had been revealed antiferromagnetism by temperature dependence of susceptibility. The antiferromagnetism of the thin film had occurred because super exchange interaction of Fe_2O_3 and CuO within the $\text{BiFe}_{1-x}\text{Cu}_x\text{O}_3$ thin films (Zeleňáková *et al.*, 2010). The neel temperature and coercive force increased

with increasing Cu doping content as $x = 0.01-0.2$. It clearly, the Cu doping enhanced ferromagnetic behavior within bismuth ferrite thin films. The increasing of ferromagnetic behavior of the thin films are evident of double exchange effect $\text{CuO-Cu}_2\text{O}_3$ which involved with mixture oxidation state of $\text{Cu}^{2+,3+}$ (García *et al.*, 2005). Moreover, increasing ferromagnetism of the thin films are also evident of oxygen defects. Due to the oxygen defect lead to occur free single valence electron of metals oxide materials (Li *et al.*, 2013). The single valence electron of metals oxide materials re easy induced its magnetic moment direction by applying external magnetic field (Li *et al.*, 2013). The coercive force of $\text{BiFe}_{1-x}\text{Cu}_x\text{O}_3$ thin films revealed a little shifting axis of magnetic hysteresis loop. The shifting had occurred due to mixture of antiferromagnetic materials and ferromagnetic materials, which led to shift of magnetic hysteresis loop axis. This phenomenon called exchange anisotropy or exchange bias, which possible applied to spin valve device in hard disk reader probe (Choudhuri *et al.*, 2014). It clearly, ferromagnetic behavior existed within $\text{BiFe}_{1-x}\text{Cu}_x\text{O}_3$ thin films, and Cu doping enhance ferromagnetic behavior to bismuth ferrite thin films.

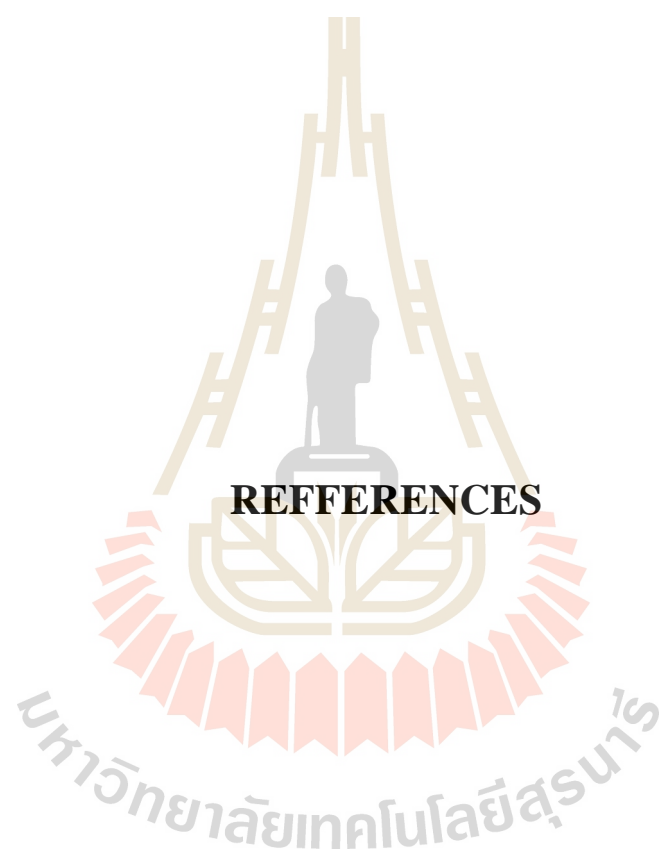
5.3 Electrical properties

The $\text{BiFe}_{1-x}\text{Cu}_x\text{O}_3$ thin films had been investigated by Agilent 4294A Precision impedance analyser. The grain and grain boundary conductance of the thin films decreased with increasing Cu-doping contents for $x = 0.0-0.03$, and $x = 0.05-0.1$. The nonlinear of grain and grain boundary conductance of the thin films were gave a reasoned explanation by increment of complex charge mobility, and occurrence of $\text{Bi}_2\text{Fe}_4\text{O}_9$ phase, respectively. However, the grain and grain boundary conductance

increased with increasing Cu doping content for $x = 0.03-0.05$, and $0.1-0.3$ (Kumar *et al.*, 2009). This increasing of grain and grain boundary conductance were gave a reason by decreasing of complex charge mobility and increasing of $\text{Bi}_2\text{Fe}_4\text{O}_9$ phase, respectively. So, the increasing of $\text{Bi}_2\text{Fe}_4\text{O}_9$ phase structure is a reasonable for explanation increasing of grain and grain boundary conductance of the thin films. According to electrical properties yield, the Cu doping are not optimal element for enhancing electrical properties to bismuth ferrite thin films.

5.4 Suggestion

Due to the magnetic/electrical properties of $\text{BiFe}_{1-x}\text{Cu}_x\text{O}_3$ thin films revealed antiferromagnetism behaviour and poor electrical conductance. The magnetic/electrical properties results show unsuitable for applying magnetic/electronic application, according to inaccurate increasing of the dielectric constant conductance and the loss tangent. However, maybe the antiferromagnetism behaviour of the thin films possible applies to magnetic head reader because of the phenomenon exchange anisotropy. Therefore, advance films preparation method of high radio frequency sputtering is an interesting method for upgrade films morphology quality of $\text{BiFe}_{1-x}\text{Cu}_x\text{O}_3$ thin films. Maybe the high quality morphology films of $\text{BiFe}_{1-x}\text{Cu}_x\text{O}_3$ thin films express excellent magnetic/electrical properties, which are useful for magnetic devices and electronic devices. Furthermore, maybe the energy storage application and electrical generator are studied base on BiFeO_3 films structure because of in the recent day, the BiFeO_3 were reported to high capacitance of superconductor applications.



REFERENCES

REFERENCES

- Arnold, D., S Knight, K., Morrison, F. and Lightfoot, P. (2009). **Ferroelectric-Paraelectric Transition in BiFeO₃ : Crystal Structure of the Orthorhombic β Phase.**
- Boonlakhorn, J., Thongbai, P., Putasaeng, B., Yamwong, T. and Maensiri, S. (2014). Very high-performance dielectric properties of Ca_{1-3x/2}Yb_xCu₃Ti₄O₁₂ ceramics. **Journal of Alloys and Compounds.** 612: 103-109.
- Bredig, G. and Allolio, R. (1927) **Roentgenuntersuchungen an katalytisch wirkenden Metallen.** (Eds, Klein, L., Aparicio, M. and Jitianu, A.) Zeitschrift fuer Physikalische Chemie (Frankfurt Am Main, Cham, pp. 41-71-126.
- Choudhuri, K., Llodrá, J., Roth, E. W., Tsai, J., Gordo, S., Wucherpennig, K. W., Kam, L. C., Stokes, D. L. and Dustin, M. L. (2014). Polarized release of T-cell-receptor-enriched microvesicles at the immunological synapse. **Nature.** 507: 118.
- Dhir, G., Uniyal, P. and Kumar Verma, N. (2017). **Tactics of particle size for enhanced multiferroic properties in nanoscale Ca-doped BiFeO₃.**
- Dong, G., Tan, G., Liu, W., Xia, A. and Ren, H. (2014). Crystal structure and highly enhanced ferroelectric properties of (Tb, Cr) co-doped BiFeO₃ thin films fabricated by a sol-gel method. **Ceramics International.** 40(1): 1919-1925.

- Dong, G., Tan, G., Luo, Y., Liu, W., Xia, A. and Ren, H. (2014). Charge defects and highly enhanced multiferroic properties in Mn and Cu co-doped BiFeO₃ thin films. **Applied Surface Science**. 305: 55-61.
- Fabian, K. and von Dobeneck, T. (1997). Isothermal magnetization of samples with stable Preisach function: A survey of hysteresis, remanence, and rock magnetic parameters. **Journal of Geophysical Research: Solid Earth**. 102(B8): 17659-17677.
- García, M. A., Ruiz-González, M. L., Quesada, A., Costa-Krämer, J. L., Fernández, J. F., Khatib, S. J., Wennberg, A., Caballero, A. C., Martín-González, M. S., Villegas, M., Briones, F., González-Calbet, J. M. and Hernando, A. (2005). Interface Double-Exchange Ferromagnetism in the Mn-Zn-O System: New Class of Biphasic Magnetism. **Physical Review Letters**. 94(21): 217206.
- Haumont, R., Al-Barakaty, A., Dkhil, B., Kiat, J. M. and Bellaiche, L. (2005) **Morphotropic phase boundary of heterovalent perovskite solid solutions: experimental and theoretical investigation of PSN-PT**. In Phys. Rev. B(Eds, Klein, L., Aparicio, M. and Jitianu, A.) Springer International Publishing, Cham, pp. 71-104106.
- Jeong, J.-H., Song, C.-G., Kim, K.-H., Sigmund, W. and Yoon, J.-W. (2018). Effect of Mn doping on particulate size and magnetic properties of LaFeO₃ nanofiber synthesized by electrospinning. **Journal of Alloys and Compounds**. 749: 599-604.
- Jian, S.-R., Chang, H.-W., Tseng, Y.-C., Chen, P.-H. and Juang, J.-Y. (2013). Structural and nanomechanical properties of BiFeO₃ thin films deposited by radio frequency magnetron sputtering. **Nanoscale Research Letters**. 8(1): 297.

- Kadomtseva, A. M., Popov, Y. F., Pyatakov, A. P., Vorob'ev, G. P., Zvezdin, A. K. and Viehland, D. (2006). Phase transitions in multiferroic BiFeO₃ crystals, thin-layers, and ceramics: enduring potential for a single phase, room-temperature magnetoelectric 'holy grail'. **Phase Transitions**. 79(12): 1019-1042.
- Kasper, J. S. and Richards, S. M. (1964). The crystal structures of new forms of silicon and germanium. **Acta Crystallographica**. 17(6): 752-755.
- Khajonrit, J., Phumying, S. and Maensiri, S. (2016). **Structure and magnetic/electrochemical properties of Cu-doped BiFeO₃ nanoparticles prepared by a simple solution method.**
- Khajonrit, J., Prasoetsopha, N., Sinprachim, T., Kidkhunthod, P., Pinitsoontorn, S. and Maensiri, S. (2017). Structure, characterization, and magnetic/electrochemical properties of Ni-doped BiFeO₃ nanoparticles. **Advances in Natural Sciences: Nanoscience and Nanotechnology**. 8(1): 015010.
- Khajonrit, J., Wongprat, U., Kidkhunthod, P., Pinitsoontorn, S. and Maensiri, S. (2018). Effects of Co doping on magnetic and electrochemical properties of BiFeO₃ nanoparticles. **Journal of Magnetism and Magnetic Materials**. 449: 423-434.
- Krishnaswamy, S., Ayyappan, J. and Venkateswaran, C. (2015). **Structural, magnetic and electrical properties of BiFeO₃ co-substituted with Pr–Mn.**
- Kumar, A., Singh, D. and Kaur, D. (2009). Grain size effect on structural, electrical and mechanical properties of NiTi thin films deposited by magnetron co-sputtering. **Surface and Coatings Technology**. 203(12): 1596-1603.

- Kumar, J. and Saxena, R. (1989). Formation of NaCl- and Cu₂O-type oxides of platinum and palladium on carbon and alumina support films. **Journal of the Less Common Metals.** 147(1): 59-71.
- Kumar, N., Kaushal, A., Bhardwaj, C. and Kaur, D. (2010). **Effect of La doping on structural, optical and magnetic properties of BiFeO₃ thin films deposited by pulsed laser deposition technique.**
- Lee, C.-C. and Wu, J.-M. (2007). Effect of film thickness on interface and electric properties of BiFeO₃ thin films. **Applied Surface Science.** 253(17): 7069-7073.
- Li, W., Zhao, R., Wang, L., Tang, R., Zhu, Y., Lee, J. H., Cao, H., Cai, T., Guo, H. and Wang, C. (2013). Oxygen-vacancy-induced antiferromagnetism to ferromagnetism transformation in Eu_{0.5}Ba_{0.5}TiO_{3-δ} multiferroic thin films. **Scientific Reports.** 3: 2618.
- Li, Y., Fan, Y., Zhang, H.-g., Teng, X., Dong, X., Liu, H., Ge, X., Li, Q., Chen, W., Li, X. a. and Ge, Z. (2013). **Structural, Thermal, and Magnetic Properties of Cu-doped BiFeO₃.**
- Li, Y., Fan, Y., Zhang, H., Teng, X., Dong, X., Liu, H., Ge, X., Li, Q., Chen, W., Li, X. a. and Ge, Z. (2014). Structural, Thermal, and Magnetic Properties of Cu-doped BiFeO₃. **Journal of Superconductivity and Novel Magnetism.** 27(5): 1239-1243.
- Lin, J., Tong, P., Cui, D., Yang, C., Yang, J., Lin, S., Wang, B., Tong, W., Zhang, L., Zou, Y. and Sun, Y. (2015). Unusual ferromagnetic critical behavior owing to short-range antiferromagnetic correlations in antiperovskite Cu_{1-x}NMn_{3+x} (0.1 ≤ x ≤ 0.4). **Scientific Reports.** 5: 7933.

- Lopez Maldonado, K. L., de la Presa, P., de la Rubia, M. A., Crespo, P., de Frutos, J., Hernando, A., Matutes Aquino, J. A. and Elizalde Galindo, J. T. (2014). Effects of grain boundary width and crystallite size on conductivity and magnetic properties of magnetite nanoparticles. **Journal of Nanoparticle Research**. 16(7): 2482.
- Mishra, D., Mandal, B., Mukherjee, R., Naik, R., Lawes, G. and Nadgorny, B. (2012). **Oxygen vacancy enhanced room temperature magnetism in Al-doped MgO nanoparticles.**
- Moreau, J. M., Michel, C., Gerson, R. and James, W. J. (1971). Ferroelectric BiFeO₃ X-ray and neutron diffraction study. **Journal of Physics and Chemistry of Solids**. 32(6): 1315-1320.
- Muller, O. and Roy, R. (1968). Formation and stability of the platinum and rhodium oxides at high oxygen pressures and the structures of Pt₃O₄, β-PtO₂ and RhO₂. **Journal of the Less Common Metals**. 16(2): 129-146.
- Patterson, A. L. (1939). The Scherrer Formula for X-Ray Particle Size Determination. **Physical Review**. 56(10): 978-982.
- Priya, A. S., Banu, I. S. and Anwar, S. (2016). Influence of Dy and Cu doping on the room temperature multiferroic properties of BiFeO₃. **Journal of Magnetism and Magnetic Materials**. 401: 333-338.
- Qi, X., Roberts, P., Mathur, N., Lee, J., Foltyn, S., Jia, Q. and MacManus-Driscoll, J. (2006). Multi-Ferroic BiFeO₃ Films Prepared by Liquid Phase Epitaxy and Solgel Methods. **Advanced Dielectric, Piezoelectric and Ferroelectric Thin Films**. 162: 69-73.

- Qian, G., Zhu, C., Wang, L., Tian, Z., Yin, C., Li, C. and Yuan, S. (2017). Enhanced ferromagnetic, ferroelectric, and dielectric properties in BiFeO₃-SrTiO₃-Bi_{0.5}Na_{0.5}TiO₃ ceramics. **Journal of Electronic Materials**. 46(11): 6717-6726.
- Ragoisha, G. A. and Bondarenko, A. S. (2005). Potentiodynamic electrochemical impedance spectroscopy. **Electrochimica Acta**. 50(7): 1553-1563.
- RANGAVITTAL, N., ROW, T. N. G. and RAO, C. N. R. **A study of cubic bismuth oxides**. In Advances in Chemistry, pp. 95-108.
- Ravel, B. and Newville, M. (2006). **Ravel, B. & Newville, M. ATHENA and ARTEMIS: Interactive graphical data analysis using IFEFFIT**. **Phys. Scr.** **115**, 1007-1010.
- Ren, Y., Zhu, X., Zhu, J., Zhu, J. and Xiao, D. (2015). **Comparative study of Mn³⁺ and Mn²⁺ doping effects on structure and electrical properties of BiFeO₃ thin films**.
- Rhidwan, I., Triyono, D. and Laysandra, H. (2017). Crystallite size dependence on electrical properties of LaFeO₃.0.1Fe₃O₄ nanocomposite material. **IOP Conference Series: Materials Science and Engineering**. 188: 012058.
- Riaz, S., Shah, S., Akbar, A., Atiq, S. and Naseem, S. (2015). Effect of Mn doping on structural, dielectric and magnetic properties of BiFeO₃ thin films. **Journal of Sol-Gel Science and Technology**. 74(2): 329-339.
- Schumacher, D., Steffen, A., Voigt, J., Schubert, J., Brückel, T., Ambaye, H. and Lauter, V. (2013). Inducing exchange bias in La_{0.67}Sr_{0.33}MnO₃-SrTiO₃ thin films by strain and oxygen deficiency. **Physical Review B**. 88(14): 144427.
- Shah, S. M. H., Riaz, S., Hussain, S. S., Atiq, S. and Naseem, S. (2015). Structural, Magnetic and Dielectric Properties of Ba Doped BiFeO₃ Thin Films.

Materials Today: Proceedings. 2(10, Part B): 5654-5659.

Sharif, S., Murtaza, G., Meydan, T., Williams, P. I., Cuenca, J., Hashimdeen, S. H., Shaheen, F. and Ahmad, R. (2018). Structural, surface morphology, dielectric and magnetic properties of holmium doped BiFeO₃ thin films prepared by pulsed laser deposition. **Thin Solid Films.** 662: 83-89.

Shirsath, S. E., Jadhav, S. S., Mane, M. L. and Li, S. (2017) **Ferrites Obtained by Sol-Gel Method.** In Handbook of Sol-Gel Science and Technology(Eds, Klein, L., Aparicio, M. and Jitianu, A.) Springer International Publishing, Cham, pp. 1-41.

Siemons, W., Biegalski, M. D., Nam, J. H. and Christen, H. M. (2011). Temperature-Driven Structural Phase Transition in Tetragonal-Like BiFeO₃. **Applied Physics Express.** 4(9): 095801.

Singh, M. K., Jang, H. M., Ryu, S. and Jo, M.-H. (2006). Polarized Raman scattering of multiferroic BiFeO₃ epitaxial films with rhombohedral R3c symmetry. **Applied Physics Letters.** 88(4): 042907.

Tang, X., Hu, L., Yang, J., Chen, L., Dai, J., Song, W., Yang, Z., Zhu, X. and Sun, Y. (2014). BiFeO₃ thin films prepared on metallic Ni tapes by chemical solution deposition: effects of annealing temperature and a La_{0.5}Sr_{0.5}TiO₃ buffer layer on the dielectric, ferroelectric and leakage properties. **RSC Advances.** 4(62): 32738-32743.

Tutov, A. G. and Markin, V. N. (1970) **The X-ray structural analysis of the antiferromagnetic Bi₂Fe₄O₉ and the isotypical combinations Bi₂Ga₄O₉ and Bi₂Al₄O₉.** (Eds, Klein, L., Aparicio, M. and Jitianu, A.) Zeitschrift fuer Physikalische Chemie (Frankfurt Am Main, Cham, pp. 2014-2017-2016.

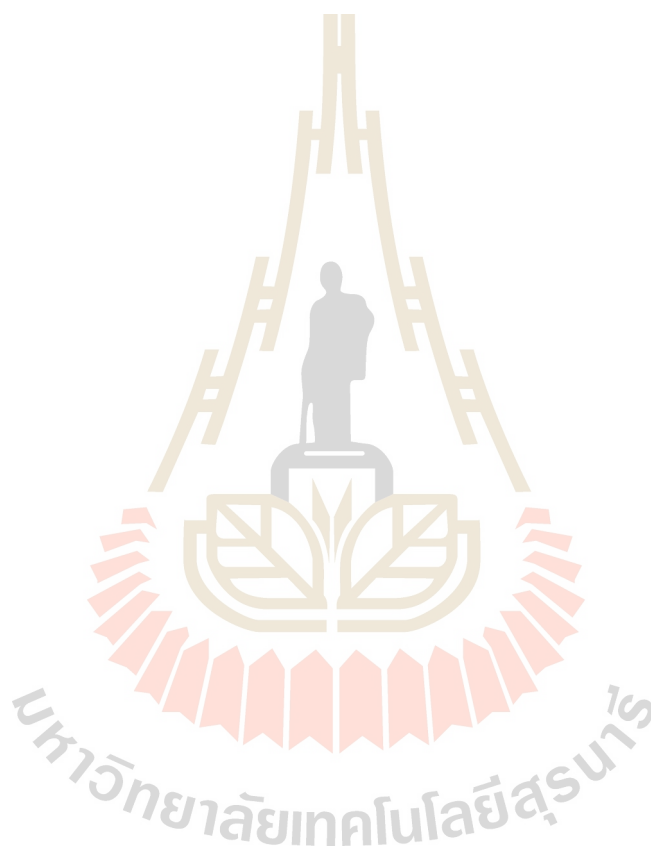
- Wang, J. (2003). J. Wang, JB Neaton, H. Zheng, V. Nagarajan, SB Ogale, B. Liu, D. Viehland, V. Vaithyanathan, DG Schlom, UV Waghmare, NA Spaldin, KM Rabe, M. Wuttig, and R. Ramesh, Science 299, 1719 (2003). **Science**. 299: 1719.
- Wang, X., Yan, B., Dai, Z., Liu, M. and Liu, H. (2010). Enhanced Ferroelectric Properties of Gd- Substitution BiFeO₃ Thin Films Prepared by Sol-Gel Process. **Ferroelectrics**. 410(1): 96-101.
- Wu, X., Tian, M., Guo, Y., Zheng, Q., Luo, L. and Lin, D. (2015). Phase transition, dielectric, ferroelectric and ferromagnetic properties of La-doped BiFeO₃-BaTiO₃ multiferroic ceramics. **Journal of Materials Science: Materials in Electronics**. 26(2): 978-984.
- Xue, J. M., Sim, M. H., Ezhilvalavan, S., Zhou, Z. H., Wang, J., Zhu, H. and Miao, J. M. (2004). Ferroelectric and dielectric properties of 0.6SrBi₂Nb₂O₉-0.4BiFeO₃ thin films. **Thin Solid Films**. 460(1): 1-6.
- Yotburut, B., Thongbai, P., Yamwong, T. and Maensiri, S. (2017). Electrical and nonlinear current-voltage characteristics of La-doped BiFeO₃ ceramics. **Ceramics International**. 43(7): 5616-5627.
- Yotburut, B., Thongbai, P., Yamwong, T. and Maensiri, S. (2017). Synthesis and characterization of multiferroic Sm-doped BiFeO₃ nanopowders and their bulk dielectric properties. **Journal of Magnetism and Magnetic Materials**. 437: 51-61.
- Zeľeňáková, A., Kovac, J. and Zelenak, V. (2010). **Magnetic properties of Fe₂O₃ nanoparticles embedded in hollows of periodic nanoporous silica.**

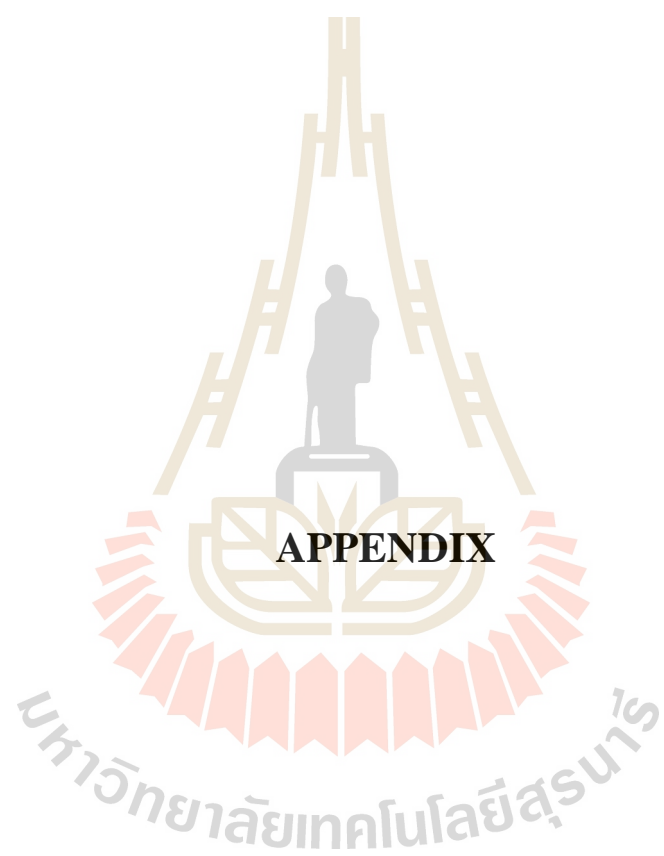
Zhai, X. Z., Deng, H. M., Zhou, W. L., Yang, P. X., Chu, J. H. and Zheng, Z. (2015).

Structural, optical and magnetic tunability in KBiFe_2O_5 multiferroics. **RSC Advances**. 5(100): 82351-82356.

Zhou, J.-P., Yang, R.-L., Xiao, R.-J., Chen, X.-M. and Deng, C.-Y. (2012). Structure

and phase transition of BiFeO_3 cubic micro-particles prepared by hydrothermal method. **Materials Research Bulletin**. 47(11): 3630-3636.





APPENDIX

PUBLICATION AND PRESENTATION

1 List of publication

Jampreecha, T., Khajonrit, J., Kidkhunthod, P., Meevasana, W. and Maensiri, S. (2018). Studies on structural characterization and electrical properties of Cu-doped BiFeO₃ thin films. **Journal of Physics: Conference Series**. 012155

2 List of oral presentation

Jampreecha, T., Khajonrit, J., Kidkhunthod, P., Meevasana, W. and Maensiri, S. (2018). Studies on structural characterization and electrical properties of Cu-doped BiFeO₃ thin films. **In Siam Physics Congress 2018 (SPC2018)**, Pitsanulok, Thailand.

Jampreecha, T., Ouksaphea, P., Khajonrit, J., Meevasana, W. and Maensiri, S. (2018). Fabrication, Structural and Dielectric Properties of Cu-Doped BiFeO₃ Thin Films. **2018 ISAF-FMA-AMEC-PFM (IFAAP) Joint Conference**. Hiroshima, Japan.

3 List of poster presentation

Jampreecha, T., Meevasana, W. and Maensiri, S. (2017). Fabrication, Structural and Magnetic Properties of Cu-Doped BiFeO₃ Thin Films. **The 5th Southeast Asia Conference on Thermoelectrics (SACT2018)**. Siem Reap, Cambodia.

CURRICULUM VITAE

Name Mr. Tachgiss Jampreecha

Date of Birth July 27, 1992

Place of Birth Alunaumarin road, Siri Rat, Bangkok Noi, Bangkok, 10700,
Thailand

Education

2011-2014 Khon Kaen University, Khon Kaen, Thailand. B. S. in Physics

